Effect of Hail Impact on Leading Edge Polyurethane Coated Composites

MSc Thesis

Reshab Savana

Delft University of Technology

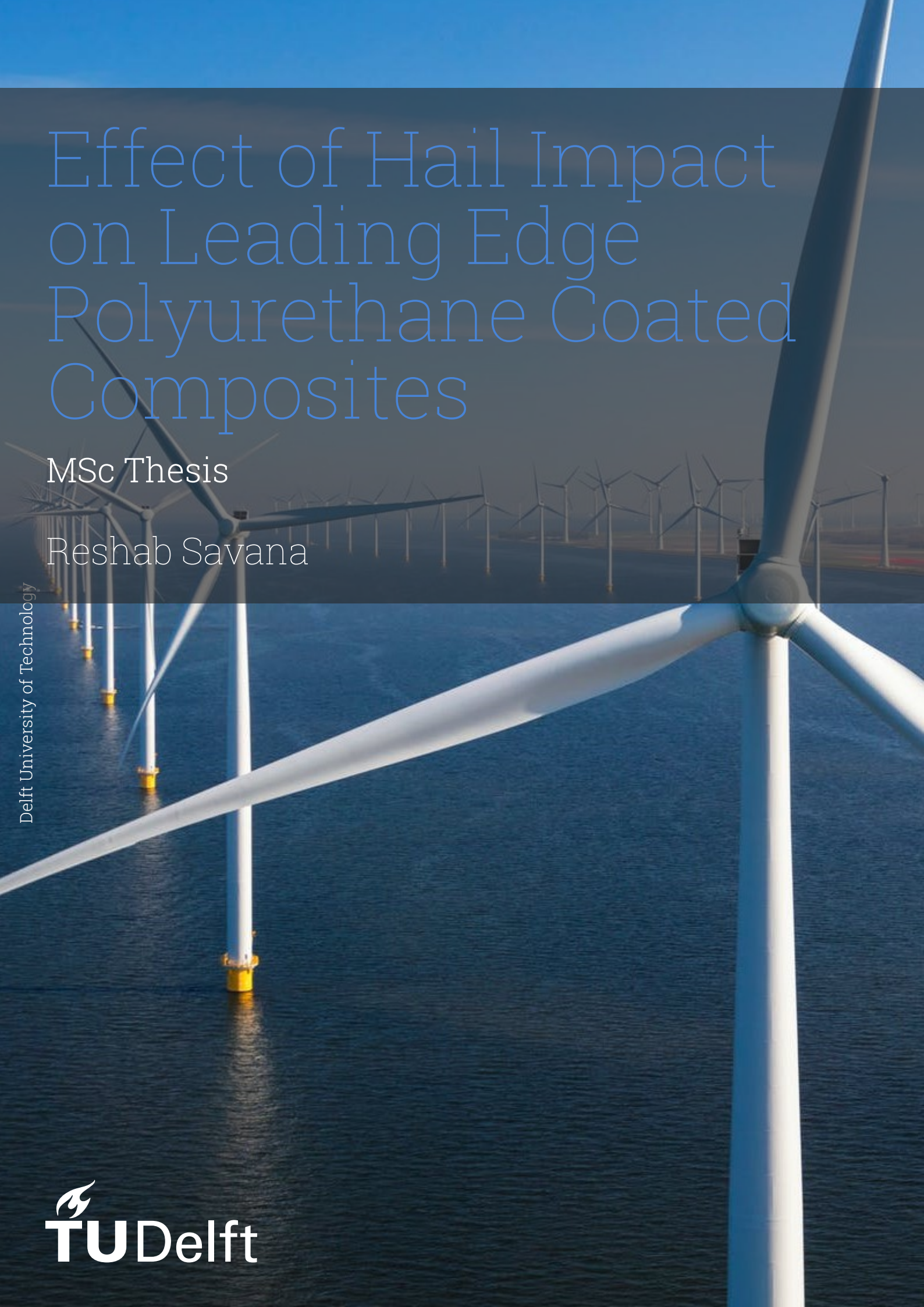

TU Delft

Effect of Hail Impact on Leading Edge Polyurethane Coated Composites

MSc Thesis

by

Reshab Savana

to obtain the degree of Master of Science
at the Delft University of Technology,
to be defended publicly on Friday September 30, 2022 at 09:00 AM.

Student number:	5236673	
Project duration:	November 1, 2021 – September 30, 2022	
Thesis committee:	Prof. dr. ir. Calvin Rans,	TU Delft, Chair
	Dr. Ir. Julie Teuwen,	TU Delft, Supervisor
	Dr. B. Giovanardi,	TU Delft, Examiner

Cover Image: Aerial View of Wind Turbines, Netherlands by Peter Adams, Shutterstock

An electronic version of this thesis is available at http://repository.tudelft.nl/.

TU Delft

Preface

This thesis project presents the result of the research undertaken at the Faculty of Aerospace Engineering at TU Delft. With this, my life as a masters student at TU Delft has also come to an end. These two years have been quite challenging, particularly the last year devoted to the thesis. In the strange times that we live in, the thesis provided me a unique opportunity to experience working at the laboratory. It has allowed me to meet lots of people and exchange different ideas. What seemed like an uphill struggle at the beginning was made easier with the help of the people around me.

Firstly, I would like to thank my supervisors, Dr. Calvin Rans and Dr. Julie Teuwen for their continuous support and guidance throughout the duration of the thesis project. I am grateful for their advice, even at odd hours. I always looked forward to our meetings and the feedback I received in them. Secondly, I am thankful to the staff at DASML and DEMO- Victor, Alexander, Dave, Johan, Durga, Ed and Rob for their constant support and enthusiasm.

Further, I am grateful to Huseyin Eryörük for his help and advice throughout the thesis. I would like to thank, Saran John Vaseekaran for being a great company throughout the thesis and helping me brainstorm over various ideas, Camill de Vos for his help and support and all my friends in Delft, with whom I made great memories.

Finally, I would like to express my gratitude to my parents and my brother, for encouraging and believing in me. I also owe a special thanks to Soumya Prusty for her constant support and motivation, whenever I was feeling low.

Reshab Savana
Delft, September 2022

Abstract

The growing demand for renewable energy has led to significant developments in wind turbine technology. The ever increasing size of turbine blades and their exposure to a variety of environmental factors can affect their annual energy production and service life. Erosion caused by rainfall and hailstones is identified as two of the most detrimental types of environmental factors to the life of a turbine blade. Hailstone impact in particular is expected to affect the aerodynamic profile of the leading edge as well as cause significant damage to the composite substrate.

The aim of this research study is to investigate the effect of varying hailstone sizes on the damage mode in leading edge polyurethane coated composites subjected to hail impact. The coated glass fibre composite samples were experimentally tested using an impact gas cannon. The impact parameters were determined based on real-life scenarios of blade tip speeds and hailstone sizes. Simulated hail ice (SHI) were manufactured using de-ionized water to form monolithic ice spheres. SHI of 15 mm and 20 mm diameter were used in the research for conducting the hail impact experiments. The coated composite samples were evaluated using non-contact profilometry (optical microscopy) and non-destructive testing (ultrasonic c-scan). Observations revealed that the polyurethane coatings remain largely intact throughout the hail impacts and no visible sign of damage or delamination between the coating and substrate was noticed during damage analysis. The damage mode of matrix cracks in the substrate for the impact parameters used, remained the same for both hailstone sizes. Further, it was seen over the experiments that there exists a failure threshold energy (FTE) for each hailstone size and sample thickness, below which no surface/sub-surface damage is visible. It is hypothesized based on observations in literature that a smaller hailstone will have a lower FTE compared to a larger hailstone and will be more lethal, owing to the concentrated area of contact. Future research to develop further awareness of damage evolution in the coated composites is recommended and discussed.

Contents

Preface i

Abstract iii

List of Figures vii

List of Tables xiii

Abbreviations xiv

1 Introduction 1

2 Literature Review 4
2.1 Blade Materials . . . 4
2.1.1 Blade Coating Application . . . 5
2.1.2 Typical Industrial Coatings . . . 7
2.2 Background on Hail . . . 8
2.2.1 Hailstone size distribution . . . 8
2.2.2 Material behaviour of ice . . . 9
2.2.3 Impact velocity of hailstones . . . 11
2.3 Hail Impact Research . . . 13
2.3.1 Hail impact contact force . . . 13
2.3.2 Hail Impact on Composites . . . 15
2.4 Research Definition . . . 21

3 Methodology 22
3.1 Research Strategy . . . 22
3.2 Experimental Setup . . . 24
3.2.1 Test Samples . . . 24
3.2.2 Experimental Apparatus . . . 26
3.3 Manufacturing Hailstones . . . 29
3.4 Challenges with gas cannon & modifications to setup . . . 30
3.5 Measurement Techniques . . . 31
3.5.1 Mass measurement . . . 31
3.5.2 Velocity Measurement . . . 31
3.5.3 Optical microscope and Laser confocal microscope . . . 33
3.5.4 Ultrasonic C-scan . . . 34
3.5.5 Sample Preparation & Cross-Sectional Microscopy . . . 34

4 Results 37
4.1 Optical Microscopy . . . 37
4.2 Ultrasonic C-scan . . . 41
4.3 Damage Analysis of Sample Cross-Sections . . . 42
4.4 Projectile Kinetic Energy and Peak Contact Force . . . 45

5 Discussions 48
5.1 Optical Microscopy . . . 48

5.2 Ultrasonic C-Scans 49
5.3 Cross-Sectional Microscopy 49
5.4 Kinetic Energy and Peak Contact Force 50

6 Conclusion **52**

7 Recommendations **55**

A Design Chart for Peak Force Estimation **63**

B Pressure-velocity calibration **65**

C Hailstone Mass Measurement **67**

D Optical Microscopy **69**

E Ultrasonic C-scans **93**

F Cross-Sectional Microscopy **97**

G Test Summary **101**

List of Figures

1.1 Distribution of wind power installations by country in 2020 [6] 1
1.2 Evolution of Wind Turbines, in terms of turbine capacity, hub height and rotor diameter [8] 2
1.3 Example of (a) Erosion of turbine blade [11] and (b) Leading Edge Erosion of turbine blade [12] 2
1.4 Challenges of on-site maintenance of wind turbines [13] 3

2.1 Manufacturing of turbine blades by vacuum infusion [17] 5
2.2 Material application through in-mould coating approach [21] 5
2.3 Post-mould coating application through (a) spray, (b) roller and (c) trowel [21] . 6
2.4 Schematic depicting (a)Cross-section of a blade, (b)Gelcoat based in-mould coating and (c)Elastomeric post-mould coating, applied with primer and putty layers [22] 6
2.5 Cross section of a hailstone, depicting onion-like layered structure [42] 8
2.6 Distribution of hail incidents recorded at UK MIDAS stations from 1949-2013 [43] 9
2.7 Size distribution of hail reports across Europe as of October 2021 [44] 9
2.8 Illustration of the ductile to brittle transition of ice [45] 10
2.9 Illustration of ice break-up on impact [47] 11
2.10 Terminal velocity of hailstones (upto SHI diameter of 20 mm) 12
2.11 Comparison between impact velocities at different blade positions for a 15 mm and 30 mm hailstone and a rain droplet with terminal velocity of 8 m/s [41] . . . 12
2.12 Damage of aerospace composite structures by hail impact [53] 13
2.13 Gas gun setup used to propel hailstones[49] 13
2.14 Images from high-speed footage depicting hail impact, cracking and fragmentation of ice [49] 14
2.15 Force history recorded by experiments for a 61 mm SHI at 61.8 m/s [49] 14
2.16 Contact force measurement apparatus [54] 15
2.17 Equilibrium of forces acting on target [54] 15
2.18 Depiction of inertial and reaction forces for a 50 mm hailstone[54] 15
2.19 Illustration of 2 DOF spring-damper system used in analytical model [54] 15
2.20 Oblique marks observed for 50 impacts of 15mm hailstone at a mean velocity of 85.6 m/s [50] 16
2.21 Plot of peak force vs kinetic energy for normal impacts [59] 17
2.22 Damage mode progression observed by Kim et al.[59] for high velocity SHI impacts 18
2.23 Plot of failure threshold energy vs panel thickness for different SHI sizes [59] . 18
2.24 Backside fibre failure observed for cotton-filled 25.4 mm SHI at 71.6 m/s [53] . 19
2.25 State of cotton-filled ice after impact, showing the deformation and that it is intact [53] 19
2.26 Plot of normalized failure threshold energy vs ratio of panel thickness and SHI diameter [53] 20

3.1 Maximum blade tip speed vs rotor diameter for different wind turbine operators [41] . . . 23
3.2 Polyurethane coated GFRP specimen (8.8 cm x 8.5 cm in size). The front side has the white PU coating on it. . . . 25
3.3 Cross section of a test sample. Left - Cross section showing thickness of substrate (2664.82 μm) and Right - Cross-section showing thickness of coating (302.75 μm) . . . 25
3.4 Impact gas cannon at DASML . . . 27
3.5 Mounting of target sample inside impact chamber . . . 28
3.6 High speed camera setup to observe hail impact . . . 28
3.7 Manufacturing of hailstones . . . 29
3.8 Acrylic tube for 20mm hailstone . . . 30
3.9 3D printed casing around acrylic tube for 15mm hailstone . . . 30
3.10 Aluminium plate assembly . . . 30
3.11 Positioning of scale near sample . . . 30
3.12 20 mm SHI in frame no.46109, coinciding with 272.6 cm on scale . . . 32
3.13 20 mm SHI in frame no.46104, coinciding with 274.8 cm on scale . . . 32
3.14 Pressure vs velocity calibration of 15 mm and 20 mm SHI with gas cannon . . . 33
3.15 Microscopes used for damage analysis . . . 33
3.16 Ultrasonic C-scan . . . 34
3.17 Secotom-10 cutting machine . . . 35
3.18 Tegramin-20 grinding and polishing machine . . . 35
3.19 Creating cross-section of samples around damage zone . . . 35
3.20 Cut samples embedded in resin . . . 36

4.1 (a-f)High-speed images of simulated hail ice impact, depicting impact and deformation of hailstone. Here, the hailstone diameter is 20 mm and the impact velocity is 88 m/s . . . 37
4.2 Optical microscopy pictures of Sample D3 before impact . . . 38
4.3 Optical microscopy picture of rear of Sample D3 before impact . . . 38
4.4 Optical microscopy pictures of Sample D3 after 10 impacts of 15 mm SHI . . . 39
4.5 Optical microscopy picture of rear of Sample D3 after 10 impacts of 15 mm SHI, showing matrix cracks in -45° direction . . . 39
4.6 Optical microscopy pictures of Sample B5 before impact . . . 40
4.7 Optical microscopy pictures of Sample B5 after 10 impacts of 20 mm SHI . . . 40
4.8 Optical microscopy picture of rear of Sample B5 after 10 impacts of 20 mm SHI, showing matrix cracks in -45° direction. A closeup of the matrix crack shows whitening of the matrix around the crack . . . 41
4.9 C-scan of sample D3 after 10 impacts of 15 mm SHI . . . 41
4.10 C-scan of sample B5 after 10 impacts of 20 mm SHI . . . 41
4.11 Optical microscopy picture of the cross-section of Sample D3 after 10 impacts of 15 mm SHI . . . 42
4.12 Optical microscopy picture of the cross-section of Sample C5 after 15 impacts of 15 mm SHI . . . 43
4.13 Optical microscopy picture of the cross-section of Sample B5 after 10 impacts of 20 mm SHI . . . 43
4.14 Optical microscopy picture of the cross-section of Sample E4 after 5 impacts of 20 mm SHI . . . 44

4.15 Impact velocity vs kinetic energy for 15 mm and 20 mm hailstone. (The blue curly brace on the left indicates the range within which the FTE for a 20 mm SHI lies in. Similarly, the green curly brace on the right indicates the range within which the FTE for a 15 mm SHI lies in. 45
4.16 Peak contact force vs kinetic energy for 15 mm and 20 mm hailstone 46
4.17 Impact velocity vs cumulative force, providing total force imparted on the sample 47
4.18 Impact velocity vs cumulative kinetic energy, providing total energy imparted on the sample 47

A.1 Design chart to estimate peak forces for SHI ranging from 5 mm to 100 mm diameter [54] 64

D.1 Optical microscopy pictures of Sample C2 before impact 69
D.2 Optical microscopy pictures of Sample C2 after 10 impacts of 15 mm SHI . . . 70
D.3 Optical microscopy pictures of Sample C2 after 15 impacts of 15 mm SHI . . . 70
D.4 Optical microscopy pictures of Sample C3 before impact 71
D.5 Optical microscopy pictures of Sample C3 after 10 impacts of 15 mm SHI . . . 71
D.6 Optical microscopy pictures of Sample C3 after 15 impacts of 15 mm SHI . . . 72
D.7 Optical microscopy pictures of Sample C4 before impact 72
D.8 Optical microscopy pictures of Sample C4 after 10 impacts of 15 mm SHI . . . 73
D.9 Optical microscopy pictures of Sample C4 after 15 impacts of 15 mm SHI . . . 73
D.10 Optical microscopy pictures of Sample C5 before impact 74
D.11 Optical microscopy pictures of Sample C5 after 10 impacts of 15 mm SHI . . . 74
D.12 Optical microscopy pictures of Sample C5 after 15 impacts of 15 mm SHI . . . 75
D.13 Optical microscopy pictures of Sample D1 before impact 75
D.14 Optical microscopy pictures of Sample D1 after 10 impacts of 15 mm SHI . . . 76
D.15 Optical microscopy pictures of Sample D2 before impact 76
D.16 Optical microscopy pictures of Sample D2 after 10 impacts of 15 mm SHI . . . 77
D.17 Optical microscopy pictures of Sample B3 before impact 78
D.18 Optical microscopy pictures of Sample B3 after 10 impacts of 20 mm SHI . . . 78
D.19 Optical microscopy pictures of Sample B4 before impact 79
D.20 Optical microscopy pictures of Sample B4 after 10 impacts of 20 mm SHI . . . 79
D.21 Optical microscopy pictures of Sample C1 before impact 80
D.22 Optical microscopy pictures of Sample C1 after 10 impacts of 20 mm SHI . . . 80
D.23 Optical microscopy pictures of Sample E1 before impact 81
D.24 Optical microscopy pictures of Sample E1 after 5 impacts of 20 mm SHI 81
D.25 Optical microscopy pictures of Sample E2 before impact 82
D.26 Optical microscopy pictures of Sample E2 after 5 impacts of 20 mm SHI 82
D.27 Optical microscopy pictures of Sample E3 before impact 83
D.28 Optical microscopy pictures of Sample E3 after 5 impacts of 20 mm SHI 83
D.29 Optical microscopy pictures of Sample E4 before impact 84
D.30 Optical microscopy pictures of Sample E4 after 5 impacts of 20 mm SHI 84
D.31 Optical microscopy pictures of Sample E5 before impact 85
D.32 Optical microscopy pictures of Sample E5 after 5 impacts of 20 mm SHI 85
D.33 Optical microscopy picture of rear of Sample D1 after 1 impact of 15 mm SHI, showing matrix cracks in -45◦ direction 86
D.34 Optical microscopy picture of rear of Sample D1 after 10 impacts of 15 mm SHI, showing matrix cracks in -45◦ direction 86
D.35 Optical microscopy picture of rear of Sample D2 after 1 impact of 15 mm SHI, showing matrix cracks in -45◦ direction 86

D.36 Optical microscopy picture of rear of Sample D2 after 5 impacts of 15 mm SHI, showing matrix cracks in -45◦ direction 86
D.37 Optical microscopy picture of rear of Sample D2 after 7 impacts of 15 mm SHI. The matrix cracks can only be seen with coaxial light. This is possibly due to compaction pressure applied while mounting the sample on clay to observe the coating layer 87
D.38 Optical microscopy picture of rear of Sample D2 after 10 impacts of 15 mm SHI. The matrix cracks can only be seen with coaxial light. This is possibly due to compaction pressure applied while mounting the sample on clay to observe the coating layer 87
D.39 Closeup picture of matrix crack seen in sample D3 (Figure 4.5) 87
D.40 Optical microscopy picture of rear of Sample B3 after 5 impacts of 20 mm SHI, showing matrix cracks in -45◦ direction 88
D.41 Optical microscopy picture of rear of Sample B3 after 10 impacts of 20 mm SHI, showing matrix cracks in -45◦ direction 88
D.42 Optical microscopy picture of rear of Sample B4 after 4 impacts of 20 mm SHI, showing matrix cracks in -45◦ direction 88
D.43 Optical microscopy picture of rear of Sample B4 after 10 impacts of 20 mm SHI, showing matrix cracks in -45◦ direction 88
D.44 Optical microscopy picture of rear of Sample B5 after 4 impacts of 20 mm SHI, showing matrix cracks in -45◦ direction 89
D.45 Optical microscopy picture of rear of Sample B5 after 7 impacts of 20 mm SHI, showing matrix cracks in -45◦ direction 89
D.46 Optical microscopy picture of rear of Sample C1 after 3 impacts of 20 mm SHI. No matrix cracks are visible due to the breaking of the hailstones for the first 3 impacts for this sample 89
D.47 Optical microscopy picture of rear of Sample C1 after 10 impacts of 20 mm SHI, showing matrix cracks in 45◦ direction. This change in orientation is possibly due to a different orientation while clamping of the sample inside the impact chamber 89
D.48 Optical microscopy picture of rear of Sample E1 after 1 impact of 20 mm SHI. No matrix cracks are visible in this sample 90
D.49 Optical microscopy picture of rear of Sample E1 after 5 impacts of 20 mm SHI. No matrix cracks are visible in this sample 90
D.50 Optical microscopy picture of rear of Sample E2 after 1 impact of 20 mm SHI. No matrix cracks are visible in this sample 90
D.51 Optical microscopy picture of rear of Sample E2 after 5 impacts of 20 mm SHI. No matrix cracks are visible in this sample 90
D.52 Optical microscopy picture of rear of Sample E3 after 1 impact of 20 mm SHI. No matrix cracks are visible in this picture. However, cracks were seen when viewed under coaxial light 91
D.53 Optical microscopy picture of rear of Sample E3 after 5 impacts of 20 mm SHI. No matrix cracks are visible in this picture. However, cracks were seen when viewed under coaxial light 91
D.54 Optical microscopy picture of rear of Sample E4 after 1 impact of 20 mm SHI, showing matrix cracks in -45◦ direction 91
D.55 Optical microscopy picture of rear of Sample E4 after 5 impacts of 20 mm SHI, showing matrix cracks in -45◦ direction 91

D.56 Optical microscopy picture of rear of Sample E5 after 1 impact of 20 mm SHI. No matrix cracks are visible in this sample 92
D.57 Optical microscopy picture of rear of Sample E5 after 5 impacts of 20 mm SHI. No matrix cracks are visible in this sample 92

E.1 C-scan of sample C2 after 15 impacts of 15 mm SHI 93
E.2 C-scan of sample C3 after 15 impacts of 20 mm SHI 93
E.3 C-scan of sample C4 after 15 impacts of 15 mm SHI 94
E.4 C-scan of sample C5 after 15 impacts of 20 mm SHI 94
E.5 C-scan of sample D1 after 10 impacts of 15 mm SHI 94
E.6 C-scan of sample D2 after 10 impacts of 20 mm SHI 94
E.7 C-scan of sample B3 after 10 impacts of 20 mm SHI 95
E.8 C-scan of sample B4 after 10 impacts of 20 mm SHI 95
E.9 C-scan of sample C1 after 10 impacts of 20 mm SHI 95
E.10 C-scan of sample E1 after 5 impacts of 20 mm SHI 95
E.11 C-scan of sample E2 after 5 impacts of 20 mm SHI 96
E.12 C-scan of sample E3 after 5 impacts of 20 mm SHI 96
E.13 C-scan of sample E4 after 5 impacts of 20 mm SHI 96
E.14 C-scan of sample E5 after 5 impacts of 20 mm SHI 96

F.1 Optical microscopy picture of the cross-section of Sample C2 after 15 impacts of 15 mm SHI. No matrix cracks were observed in this cross-section 97
F.2 Optical microscopy picture of the cross-section of Sample D1 after 10 impacts of 15 mm SHI. 5 matrix cracks were observed in this cross-section 97
F.3 Optical microscopy picture of the cross-section of Sample B4 after 10 impacts of 20 mm SHI. 9 matrix cracks were observed in this cross-section 98
F.4 Optical microscopy picture of the cross-section of Sample E5 after 5 impacts of 20 mm SHI. No matrix cracks were observed in this cross-section 98
F.5 Closeup of crack 3 in Sample D3, shown in Figure 4.11 98
F.6 Closeup of crack 4 in Sample D3, shown in Figure 4.11 98
F.7 Closeup of crack 3 in Sample B5, shown in Figure 4.13 99
F.8 Closeup of crack 4 in Sample B5, shown in Figure 4.13 99
F.9 Closeup of crack 3 in Sample E4, shown in Figure 4.14 99
F.10 Closeup of crack 4 in Sample E4, shown in Figure 4.14 99
F.11 Closeup of crack 1 in Sample D1, shown in Figure F.2 99
F.12 Closeup of crack 4 in Sample D1, shown in Figure F.2 99
F.13 Closeup of crack 5 in Sample D1, shown in Figure F.2 99
F.14 Closeup of crack 1 in Sample B4, shown in Figure F.3 100
F.15 Closeup of crack 5 and 6 in Sample B4, shown in Figure F.3 100
F.16 Closeup of crack 8 and 9 in Sample B4, shown in Figure F.3 100

List of Tables

3.1 Overview of hail impact experiments conducted 24
3.2 Mechanical properties of polyurethane coating 25

B.1 Pressure-velocity calibration for 15 mm hailstone 66
B.2 Pressure-velocity calibration for 20 mm hailstone 66

C.1 Mass measurement for 15 mm hailstone 67
C.2 Mass measurement for 20 mm hailstone 68

G.1 15 mm Test Overview 105
G.2 20 mm Test Overview 108

Abbreviations

Abbreviation	Definition
AEP	Annual energy production
ASTM	American Society for Testing and Materials
BVID	Barely Visible Impact Damage
DASML	Delft Aerospace Structures and Materials Lab
ESSL	European Severe Storms Laboratory
FTE	Failure Threshold Energy
GFRP	Glass Fibre Reinforced Polymer
KE	Kinetic Energy
LEE	Leading edge erosion
SHI	Simulated Hail Ice
SPG	Smooth particle hydrodynamics

1

Introduction

Climate change has accelerated the focus on renewable sources of energy like wind, solar and hydropower. This is a result of global initiatives like the Paris Agreement [1], seeking to move to a carbon neutral society. According to a report by Wind Europe [2], the installed capacity of wind power in Europe is estimated to reach 277 GW by 2023. China overtook the EU in 2015, in terms of the number of wind turbines installed [3]. Global distribution of wind turbines installed in 2020 is depicted in Figure 1.1, which clearly shows China becoming a world leader in this industry. It is predicted [4] that wind energy costs will reduce 37%-49% by 2050 and fulfill one-third of the global energy needs [5].

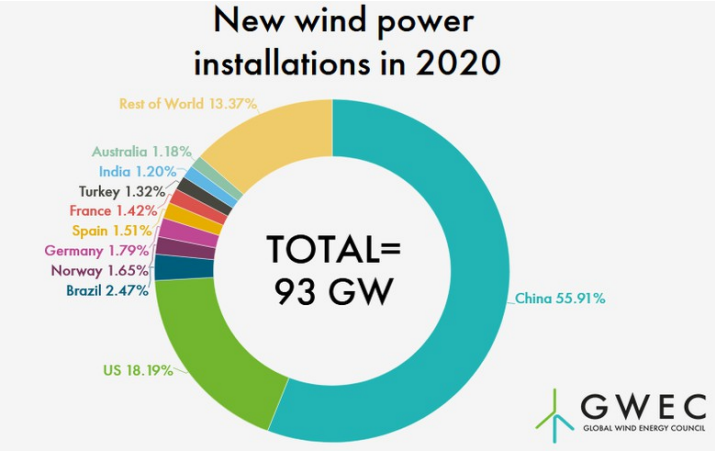

Figure 1.1: Distribution of wind power installations by country in 2020 [6]

This growing demand for wind energy has accelerated tremendous advancements in blade design and its length. The increasing blade length has brought about an increase in the blade tip speeds; wind turbines with tip speeds of more than 80 m/s are now common [7]. This is illustrated in Figure 1.2, which shows the evolution of wind turbines, in terms of energy capacity and size. The speeds depicted are often representative of the maximum attainable speeds for the design of the turbine and these turbines operate at such speeds for a limited amount of time.

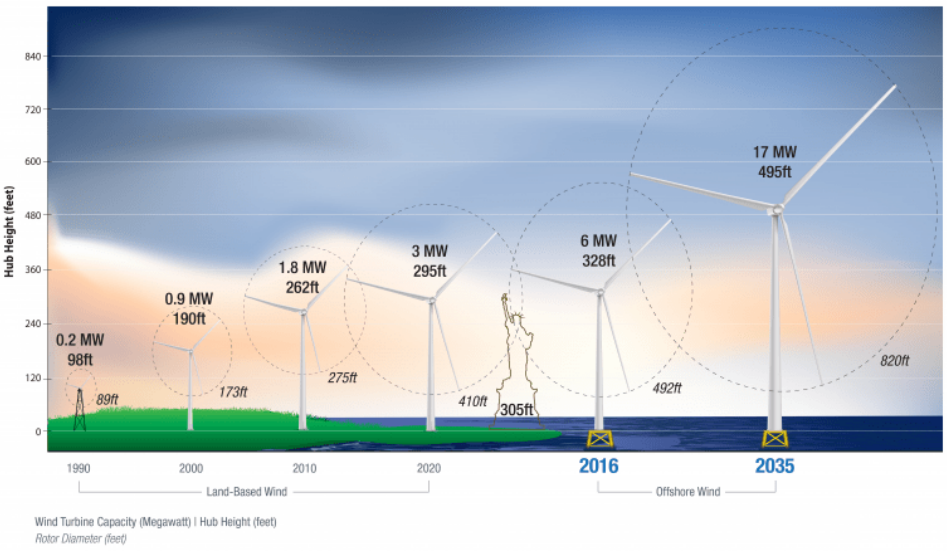

Figure 1.2: Evolution of Wind Turbines, in terms of turbine capacity, hub height and rotor diameter [8]

Wind turbines are typically expected to operate for 25 years over their service life [9]. During this service life, the blades are subjected to a variety of loads and environmental factors, while the frequency of maintenance is intended to be kept to a minimum to reduce financial losses. The high tip speeds of the wind turbine blades make them susceptible to damage and erosion caused by precipitation. Structural damage can degrade the strength and stiffness of the turbine blade. Operational life of the turbine blade can be reduced, if the structural damage crosses a certain threshold. Such a damage can be anything that compromises the structural integrity of the blade. For example, water seeping through the laminate structure can affect the load bearing capacity of the blade and severely affects it's strength and stiffness. A lack of stiffness in the structural members could also affect the airfoil shape of the blade, which in turn affects the aerodynamic efficiency.

The leading edge of the wind turbine blade is the most exposed zone to a form of damage called Leading Edge Erosion (LEE). The phenomenon of LEE of wind turbine blades is caused by repeated liquid impact by rain drops. This is accelerated when combined with hail, moisture, bugs, dust, UV and thermal loading. A real life example of this phenomenon is shown in Figure 1.3. Larger particles like hail cause more damage, when compared with raindrops of the same size, due to the kinetic energy of hail, when impacting the blade [7, 10]. Larger raindrops tend to break up into smaller droplets, while this is usually not the case with hailstones.

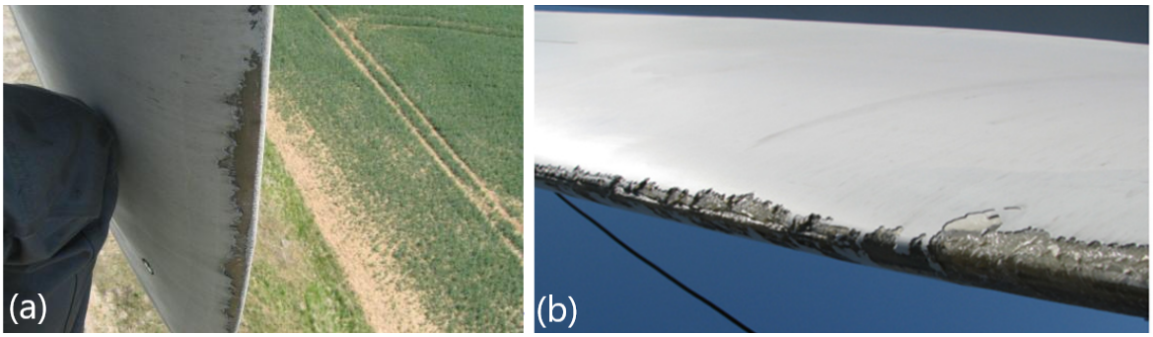

Figure 1.3: Example of (a) Erosion of turbine blade [11] and (b) Leading Edge Erosion of turbine blade [12]

LEE can lead to a loss in aerodynamic performance and negatively affect the annual energy production (AEP) of a wind turbine [13]. This was analyzed by Sagol et al. [14], where it was found that accumulation of dirt, ice and insects on the blades generates roughness, which disturbs the flow field and leads to a reduction in the power produced. Roughening produced by erosion leads to increased drag coefficients and decreased lift coefficients. An approach to mitigate AEP losses was presented by Bech et al. [15], which suggested reduction in the tip speed of the blade, during extreme weather events.

To protect the wind turbine against this form of damage, coatings are applied on the leading edge in the form of gelcoats, elastomeric coatings or paints. Gelcoats are often of the same material as the matrix of the blade composite, whereas elastomeric coatings are generally made of polyurethane, applied on the leading edge. The repair of wind turbines is known to be expensive; a repair which takes one to three days can cost between $800 and $1600, using a crane for repair or replacing a blade can cost up to $350,000 a week. Repairing offshore wind turbines becomes even more expensive due to the difficulties in accessing the wind turbine. The challenges of repairing a wind turbine blade can be visualized in Figure 1.4. Thus, it becomes imperative to minimize the occurrence of such repairs to keep maintenance costs at a minimum.

Figure 1.4: Challenges of on-site maintenance of wind turbines [13]

The current research project focusses on investigating the effect of hail impact on composite wind turbine blade. The report has been divided into separate chapters, with the following structure. chapter 2 presents a detailed literature review conducted on wind turbine blade materials, material behaviour of hailstone and research on hail impact on composites. The chapter ends with describing the research definition. chapter 3 describes the research strategy and methodology followed for conducting the hail impact experiments and the steps taken to measure impact parameters and analyze the damage. In chapter 4, the results of the thesis project are presented;ranging from optical microscopy analysis, C-scans and detailed cross-section observations have been performed. These results are discussed in detail in chapter 5, where possible hypotheses for the observations are presented. chapter 6 provides answers to the research question and all the sub-questions defined earlier. Finally, chapter 7 presents some recommendations for future work in extending this line of research and in investigating hail impacts on composites in a real-life scenario.

2

Literature Review

In order to define the research, thorough background knowledge on commonly used wind turbine materials and coatings needed to be obtained. Hail as a form of precipitation is not common all over the world and thus, research performed on understanding the material behaviour of ice and the effects of hail impacts on composites need to be studied. The experimental setup to be used for conducting such studies needed to be ascertained from literature. The following sections will present a review of the state of the art research conducted on these topics.

2.1. Blade Materials

The evolution and growth of wind turbine blades and the need for lightweight solutions has seen the implementation of composites, which have high specific strength and specific stiffness properties, while also boasting excellent fatigue properties. In the early years of the wind turbine industry, wet hand layup technique was used to manufacture the blades [16]. With the growth of wind turbine blade lengths and manufacturing technologies, most of the current blades are manufactured using resin infusion process. Resin infusion processes are typically divided into two types: Resin Transfer Molding (RTM), which involves injection of resin under high pressure and Vacuum Assisted Resin Transfer Molding (VARTM), where the resin is injected with the aid of vacuum (Figure 2.1). Manufacturing using prepregs has also been adapted in the wind energy industry (for example by the company Vestas to produce their turbine blades [16]). Resin infusion is known to be cheapter than prepreg based methods, although mechanical properties by prepreg based composites are more consistent.

The composites used in a wind turbine blade are typically composed of a thermoset polymer matrix, with carbon fibre or glass fibre reinforcements. E-glass fibres have been typically used as reinforcements in such composites, although stronger fibres like S-glass or R-glass are also occasionally used. Usage of carbon fibres have increased in recent years, due to their high stiffness and low density, permitting the design of stiff, lightweight blades. However, they are more expensive than glass fibres and have low damage tolerance and ultimate strain [16]. Aramid and basalt fibres also present a potential option for use as reinforcement in composite blades. Aramid fibres have high damage tolerance and toughness, though they have poor resistance to UV radiation [18]. Basalt fibres are known to have good mechanical properties, while being cheaper than carbon fibres [16]. They have been used in small wind turbines and show great promise for applications in hybrid composites [19].

Figure 2.1: Manufacturing of turbine blades by vacuum infusion [17]

Polyesters, epoxies and vinyl esters are some of the thermoset polymers commonly used as matrix in these composites. They offer the advantages of curing at low temperatures and low viscosity, which is suitable for resin infusion. Thermoplastics offer benefits with their circularity and higher fracture toughness. However, their applications in blade manufacturing has been limited due to their requirement of higher processing temperatures and higher viscosity.

2.1.1. Blade Coating Application

Composites have a few drawbacks, such as poor resistance to impact, sensitivity to moisture, heat and UV radiation [7]. To overcome these issues, protective coating systems are used to protect the composite against the impact and environmental factors. There are two approaches used to apply a surface coating:

1. **In-mould application:** In this approach, a coating layer is applied on the surface during the moulding process (illustrated in Figure 2.2). Typical coatings added through this method have a similar material as that of the matrix of the substrate (typically epoxy or polyester). They also allow enable manufacturers to integrate coatings with the blade, thus resulting in a smoother outer surface and improving the aerodynamic efficiency of the blade [20]. The typical terminology for such coatings is called a gelcoat.

Figure 2.2: Material application through in-mould coating approach [21]

2. **Post-mould application:** In this approach, coatings are applied after the moulding process, in the form of sprays or paints (Figure 2.3). There is more flexibility in material choice when applying coatings through this approach. Flexible, elastomeric coatings, generally made of polyurethane are applied on the leading edge, after the manufacturing of the blades. These coatings are applied in combination with a primer and putty layer, which aid the adhesion of the coating with the substrate (Figure 2.4).

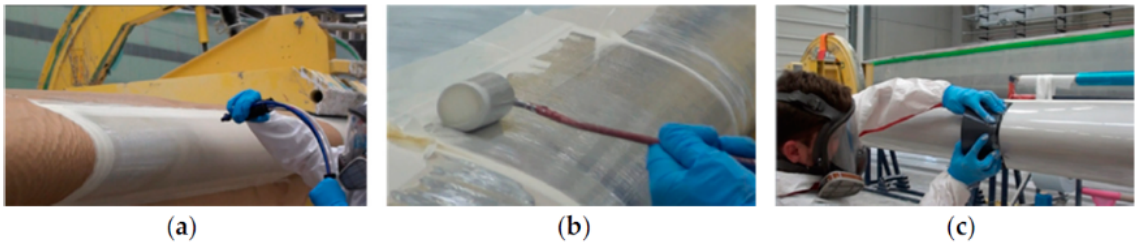

Figure 2.3: Post-mould coating application through (a) spray, (b) roller and (c) trowel [21]

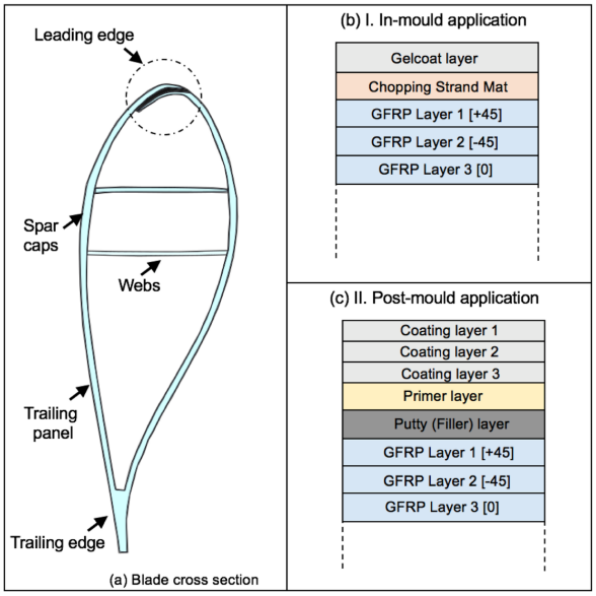

Figure 2.4: Schematic depicting (a)Cross-section of a blade, (b)Gelcoat based in-mould coating and (c)Elastomeric post-mould coating, applied with primer and putty layers [22]

Thermoplastics being more damage tolerant than thermosets, are preferred for usage in leading edge protection systems. The application of a thermoplastic on a thermoset matrix of a wind turbine blade can be complicated due to the differences in their physical, chemical and mechanical properties. Defects and bonding issues in the interface of the two materials could reduce the structural integrity of the leading edge protection system and accelerate the erosion. Cortes et al.[23] observed that incomplete or semi-cured coatings applied by in-mould techniques displayed better performance against erosion. This was due to chemical enhancement at the interface, which led to a longer incubation period and decreased erosion rate, when compared to fully cured coatings.

Zanjani et al.[24] investigated the application of an ABS thermoplastic protection system on an unsaturated polyester thermoset resin through co-bonding. The influence of the processing temperature on the cure kinetics and interphase thickness of the resin was studied. It

was observed through microhardness tests that the hardness of the interface was lower than ABS and the polyester resin. Increasing the processing temperature led to an increase in this hardness. Fractography analysis revealed that the specimens failed by interface failure and cohesive failure, with the fracture toughness of the specimens related to the amount of cohesive failure.

2.1.2. Typical Industrial Coatings

Polyurethane coatings are one of the most widely used protection systems against leading edge erosion. Leading Edge Protection systems are generally elastomeric coatings made of Polyurethane (PU), such as the 3M Wind Blade Protection Coating W4600 [25] and ProBlade by LM Wind Power [26]. Yilgör et al. [27] demonstrated the case of segmented polyurethanes having hard and soft segments, where stiffness and strength were provided by the hard segments, while the softer segments determined the damping properties [28]. Mishnaevsky and Sütterlin [29] developed an analytical model, aiming to study the effect of the structure, morphology and properties of segregated polyurethane on the erosion behaviour of the coating. The model is based on the equivalent box model (EBM) approach developed by Kolarik [30] and adaption of EBM by Govaert et al. [31], to determine the viscoelastic properties of a segmented two-phase polyurethane, as a function of its structure (volume content of the hard and soft phases). The model demonstrated that a higher difference between the damping properties of the polyurethane segments led to higher damping in the overall material and higher damping properties.

Some of the available solutions against leading edge erosion include KYNAR PVDF-acrylic hybrid emulsion coatings by Arkema, W4600 polyurethane coating by 3M [25], ProBlade by LM Wind Powder [26], Blade protective sheet by IER Fujikura and Belzona 1331 and Belzona 1381 [32, 33]. 3M [25, 34] has implemented a leading edge tape which is made of polyurethane to absorb the impact energy of rain droplets and other particulate matter. It was seen by Weigel [35] that elastomeric materials like polyurethanes have better solid-particle erosion resistance than metals, though being outperformed for the case of rain erosion due to poor performance at direct impact angles. Most of these coatings have a lifetime of about 6 to 8 years [9], with the 3M tape W8750 (one of the latest coatings in the market) having a predicted lifetime of about 16-20 years. This is still short of the expected design lifetime of 25 years.

LM Wind Power [26, 36, 37] had created a coating technology named ProBlade, which comprised of a “Highly flexible 2-component solvent free UV-resistant polyurethane based paint”. As investigated by Haag [36], exposure to UV radiation affects the erosion resistance of a coating. This applies also for the properties of the substrate, where the polyester resin showed a decrease of 15% in the average failure strain, decrease of 30 % in ultimate strength and a decrease of 18% in tensile modulus under UV exposure [38]. Water ingress into the substrate can also affect the performance of the blade. According to a report by manufacturer Gurit [39], a polyester laminate will possibly retain only 65 % of its interlaminar shear strength, when immersed in water for one year, whereas an epoxy laminate retains about 90 % of its interlaminar shear strength.

2.2. Background on Hail

Typically, a hailstone is an amalgamation of ice/water/air, with particle diameters of more than 5 mm [40]. Their shape depends on their diameter with hailstones between 5-10 mm diameter having spherical or conical shapes, while larger hailstones between 10-50 mm appear ellipsoidal. Hailstones are generally opaque in appearance and have a layered structure. Particles which are smaller than 5mm are referred to as graupel or ice pellets [41]. Hailstones are formed in thunder clouds with strong updrafts. The droplets rise up through the clouds and freeze. The ice particles descend when it has a certain mass. Some of the ice particles get caught in the updraft again and this results in the formation of an additional layer of ice. This process gets repeated and in each cycle, the ice particle acquires an additional layer of ice [41]. This results in an onion-like layered formation of ice, shown in Figure 2.5. The final size and form of the hailstone depends on the amount of time it spends in the cloud before descent to the ground. It was also seen by Field et al. [40] that hailstones smaller than 20 mm had a wide range of densities (from 50 to 890 kg/m^3). Larger hailstones were found to be more dense, with densities ranging between 810 to 915 kg/m^3.

Figure 2.5: Cross section of a hailstone, depicting onion-like layered structure [42]

2.2.1. Hailstone size distribution

The amount of hailstorms in an area varies from year to year and depends on a number of climatic factors. Hailstones are formed when the temperature in the upper atmosphere is conducive to develop ice formation while the surface temperature is warm. This causes thunderstorms. Data collected by the UK Met Office Integrated Data Archive System (MIDAS) stations found that when considering ice formations, ice pellets have the highest frequency of occurrence, while large hailstones(>10 mm) have a comparatively lower frequency [43] (Figure 2.6).

The European Severe Storm Laboratory (ESSL) collected reports of severe hailstorms across Europe (Figure 2.7). This classification takes into account hail events of more than 20 mm. The data for 2021 (upto October) showed that the number of hail reports were almost double the previous most active year (2019). This indicates the drastically changing weather patterns. It is important to note from these observations that the data collected for hailstorm reports accounts for reports onshore. Collection of offshore hail events has thus far proven to be difficult.

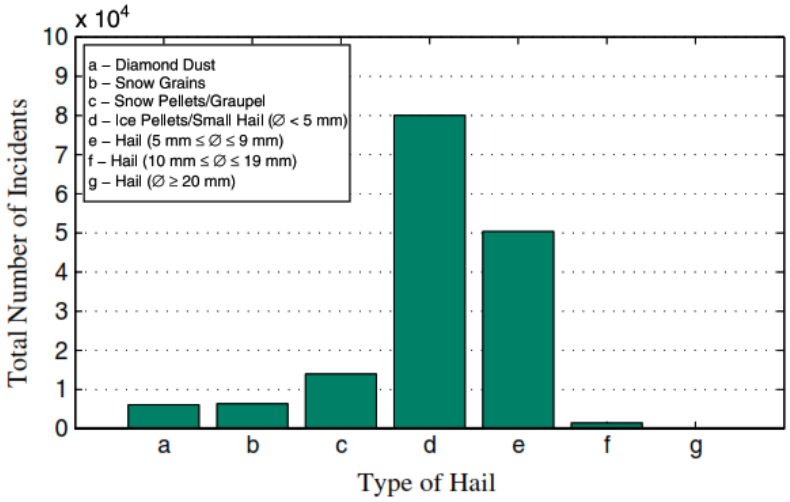

Figure 2.6: Distribution of hail incidents recorded at UK MIDAS stations from 1949-2013 [43]

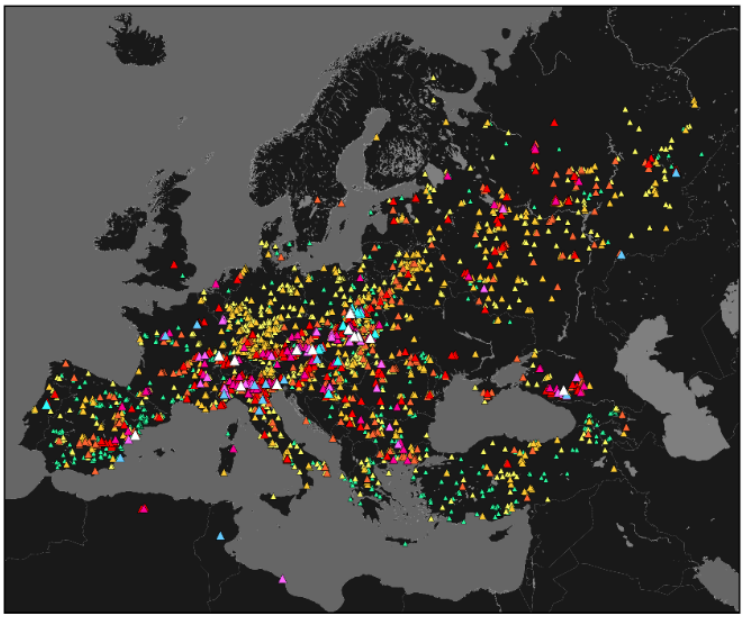

Figure 2.7: Size distribution of hail reports across Europe as of October 2021 [44]

2.2.2. Material behaviour of ice

Ice is considered to be a very complex material with 13 different crystal structures and two amorphous states [41]. The mechanical properties of ice are influenced by various other factors. Schulson [45] noted that ice behaves in two different ways in compression. It is ductile at low strain rates i.e. when the ice is compressed slowly. Increasing the strain rate leads to a change in behaviour, resulting in a brittle state of ice. This change from a ductile to brittle nature occurs at strain rates in the order of 10^{-3} s^{-1}. This can be seen by the change in slope of the curve in Figure 2.8. Increasing strain rate is also seen to result in a linear

stress-strain curve of the ice material and the compressive strength is also found to increase with a decrease of temperature. Carney et al.[46] developed a model for ice and compared it to experimental results. They found that compressive failure is a function of strain rate and the model works for multiple material conditions such as polycrystalline and single crystal ice, which exhibit strain sensitivity from 10^{-8}s^{-1} to 10^{-2}s^{-1}. However, strain sensitivity between 10^{0}s^{-1} to 10^{3}s^{-1} was also noted for single crystal ice. Dealing with these complexities and variability of the material properties of ice is one of the major challenges in predicting the impact forces and contact stresses of an ice impact, especially in the case of a hailstone strike on a composite blade.

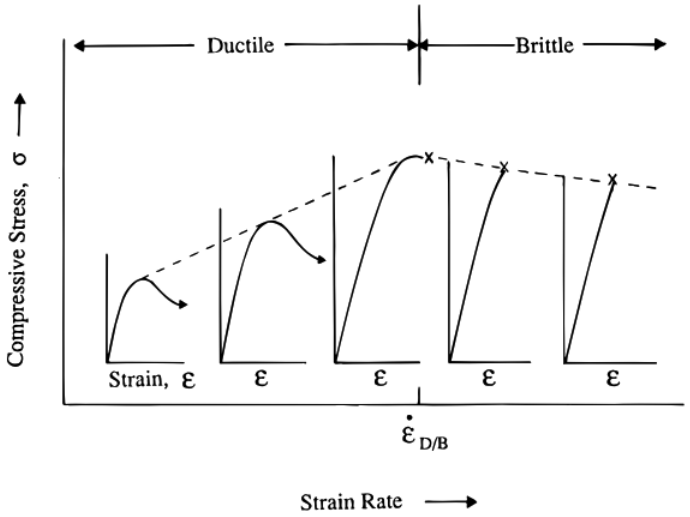

Figure 2.8: Illustration of the ductile to brittle transition of ice [45]

Roisman and Tropea [47] developed a quasi-one-dimensional model to study the impact of ice on a rigid-solid wall. The model was able to predict the force generated on impact of ice with the wall, the duration of the impact and the residual height of the ice particle. Ice impact on a target can be characterized by three different stages:

a) Initial stage of particle collision: In this stage, a shock wave develops in the ice particle and the target. This forms a small part of the duration of impact and the shock wave is expressed by the Rankine-Hugoniot jump conditions.
b) Elastic deformation of ice particle and target: This is described by the Hertzian theory [48]. This stage is seen only in case of low impact velocities.
c) Plastic deformation of ice: At this stage, the contact stresses on impact with the target reaches the yield pressure of ice. As discussed before, ice shows both ductile and brittle behaviour and at this stage, behaves like a semi-brittle material. The ice particle contains a crushed zone near the target and a cracked zone, where comparatively large sized fragments are created.

As discussed earlier in this section, the yield stress of ice depends on the strain rate. At low strain rates, this is taken as Y_{stat}=5.2MPa [49]. A characteristic velocity, $U_c = \sqrt{(Y_{stat}/\rho)} = 75.2$ m/s is defined. The density of ice is taken to be $\rho = 920$ kgm^{-3}. The average peak force for the impact of ice on the target is given by Equation 2.1, where R_0 is the radius of the impacting ice sphere and U_0 is the impact velocity. It is important to note here that the peak forces obtained from Equation 2.1 gives higher forces than what actually are expected on composites. This is because this equation takes into account impacts on solid, rigid surfaces [50].

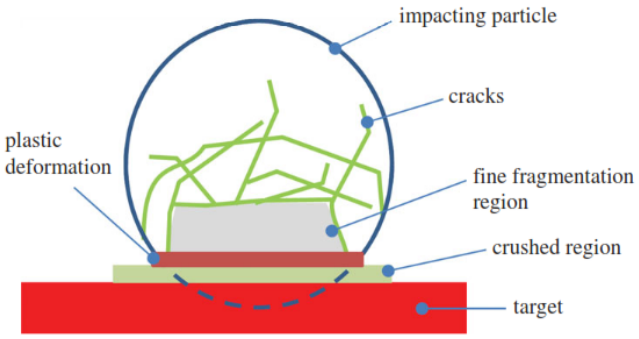

Figure 2.9: Illustration of ice break-up on impact [47]

$$F \approx \frac{4\pi}{3} R_0^2 U_0 \rho^{1/2} Y^{1/2} \tag{2.1}$$

By fitting the data from [49], the compressive yield stress of the hailstone is determined to be,

$$Y = Y_{\text{stat}} \exp\left(\frac{0.9U_0}{U_c}\right) \tag{2.2}$$

2.2.3. Impact velocity of hailstones

The impact velocity plays a crucial role in understanding the dynamics of a hailstone impact. When considering hail impacts, increase in diameter leads to an increase in hailstone mass and subsequently, the kinetic energy imparted on impact (Kinetic energy being given by $KE = \frac{1}{2}mv^2$. Furthermore, increase in diameter also leads to an increase in terminal velocity of the hailstone. The terminal velocity is the maximum velocity obtainable by a free falling hailstone. This can be seen in Equation 2.3 , derived from force balance between the gravitational force and the aerodynamic drag [41]. Here, m_h is the mass of the hailstone, g is the acceleration due to gravity, C_d is the drag coefficient, ρ_{air} is the density of air (taken as 1.29 kg/m^3) and A_h is the cross-sectional area of the hailstone.

$$V_t = \sqrt{\frac{2m_h g}{C_d \rho_{air} A_h}} \tag{2.3}$$

Assuming a spherical hailstone shape, the expression can be re-written as

$$V_t = \sqrt{\frac{4g\rho_h D}{3\rho_{air} C_d}} \tag{2.4}$$

Here, D is the diameter of the hailstone and ρ_h the density of the hailstone. For spherical hailstones, the drag coefficient is seen to vary between 0.4 and 0.8, though 0.6 is found to be a good fit over different sizes of hailstones [51]. However, as discussed earlier, the shape of a hailstone changes with size. Heymsfield et al. [52] developed size-dependent relationships for terminal velocities and kinetic energy. They are shown in Equation 2.5 and Equation 2.6. Here, D_{max} is the maximum diameter of the hailstone and Equation 2.5 is valid for hailstones upto 2.05 cm in size. This is because the shape of a hailstone changes around this size. The terminal velocity calculated by Equation 2.4 and Equation 2.5 for hailstone diameters upto 20 mm can be seen in Figure 2.10.

$$v_t = 12.65{D_{max}}^{0.65} \text{ for } D_{max} < 2.05cm \tag{2.5}$$

$$v_t = 15.69D_{max}^{0.35} \text{ for } D_{max} > 2.05cm \tag{2.6}$$

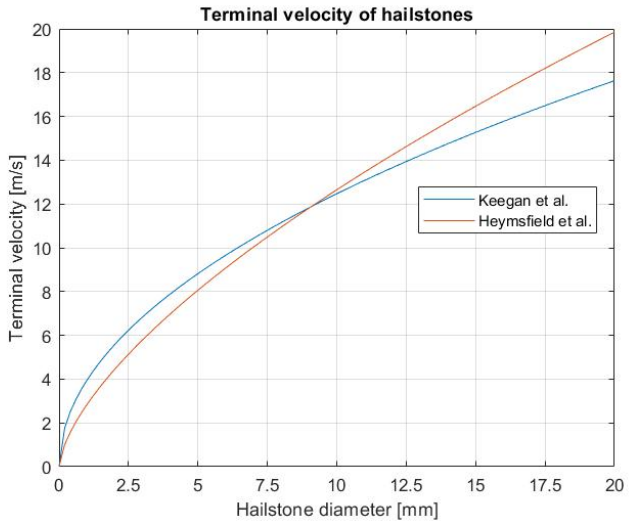

Figure 2.10: Terminal velocity of hailstones (upto SHI diameter of 20 mm)

Keegan et al. [41] used Equation 2.4 to calculate the terminal velocity of a 15 mm and a 30 mm hailstone and took the case of these hailstones impacting a wind turbine blade. The tip speed of this blade is taken to be 90 m/s with a horizontal wind velocity of 20 m/s. This was compared to the impact velocity of a rain droplet with a terminal velocity of 8 m/s. The difference in impact velocities between these distinct cases at different blade positions can clearly be seen in Figure 2.11. Taken into account the higher mass of hailstones, similar differences in the impact energy imparted during impact can be quantified. For all the cases, the maximum impact velocity can be seen when the blade sweeps upwards and is in a horizontal position (270°).

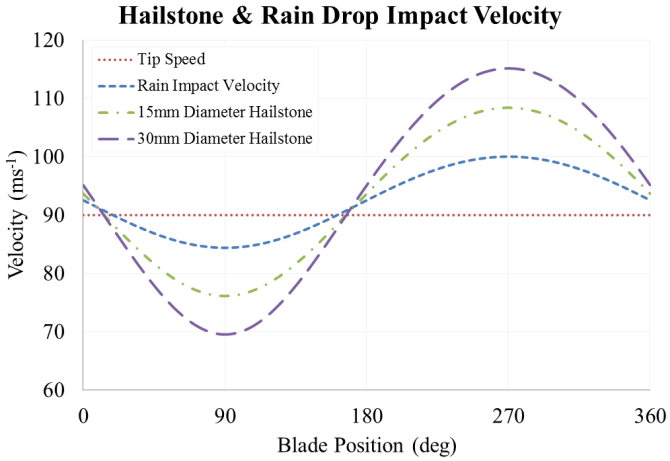

Figure 2.11: Comparison between impact velocities at different blade positions for a 15 mm and 30 mm hailstone and a rain droplet with terminal velocity of 8 m/s [41]

2.3. Hail Impact Research

Based on the impact energies observed for hail impact and the usage of composites in aerospace applications and wind turbine blades seen in the previous sections, it becomes important to understand the interaction between a hailstone and a target on impact. The impact energy and contact force generated on hail impact play an important role in this dynamics. Particular examples of damage caused to aerospace composite structures are shown in Figure 2.12a (when the aircraft is on the ground, impact velocities of around 30 m/s) and Figure 2.12b (when the aircraft is in flight, impact velocities of around 230 m/s). Numerical modelling and simulated hail impact (SHI) experiments have been conducted to get a fundamental understanding of ice impact dynamics.

(a) Fan cowl door damaged by hail impact - on-ground impact

(b) In-flight hail damage

Figure 2.12: Damage of aerospace composite structures by hail impact [53]

2.3.1. Hail impact contact force

Tippmann et al.[49] developed a strain rate dependent ice material model using strain rate dependent compression data obtained from experiments. The hail impact experiments were conducted with a gas gun setup, where the forces were measured with a force measurement bar apparatus. The gas gun utilizes compressed nitrogen gas, which is released to launch the projectile onto the target. The projectiles are propelled using a foam sabot.

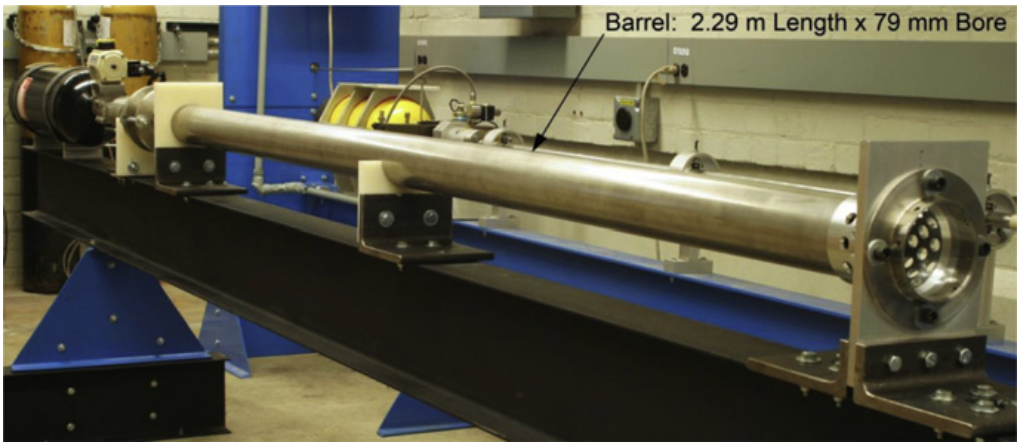

Figure 2.13: Gas gun setup used to propel hailstones[49]

The impact forces obtained from this model by Tippmann et al.[49] are in close agreement with experimental results. It was seen from high-speed footage (Figure 2.14) that crack propagation during experiments and the crack propagation obtained from the model were similar and thus,

validated the results from the model. From both the methods, it was observed that the impact force increases till the peak value and this corresponds with cracks reaching the back end of ice sphere. After this, the forces decrease as energy gets dissipated in the form of heating of the ice sphere and breakdown into smaller fragments (Figure 2.15).

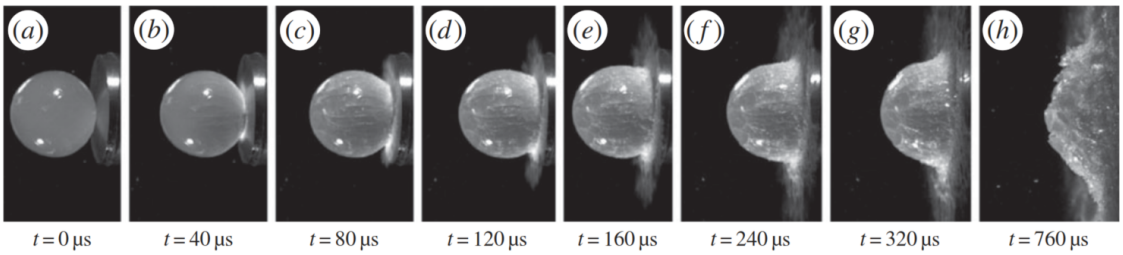

Figure 2.14: Images from high-speed footage depicting hail impact, cracking and fragmentation of ice [49]

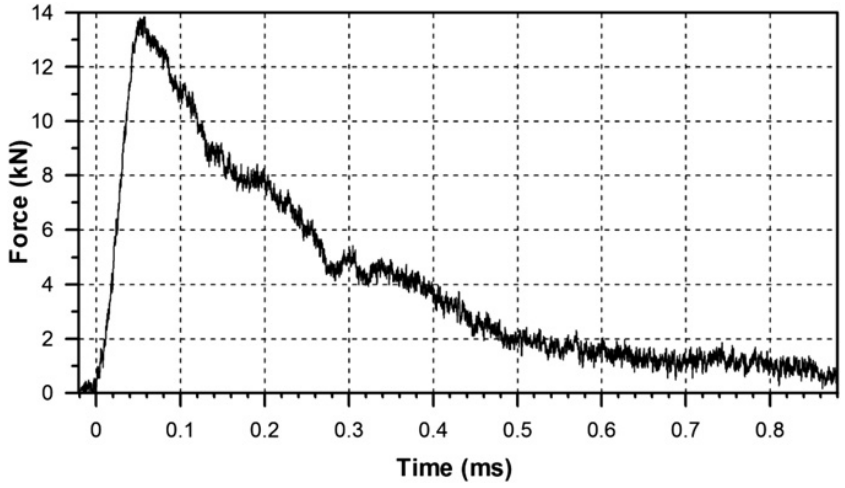

Figure 2.15: Force history recorded by experiments for a 61 mm SHI at 61.8 m/s [49]

Sun et al.[54] developed a model to predict the value of the peak force on impact of a hailstone with a target. First, they designed an apparatus for measuring the impact force of an ice projectile (Figure 2.16). This apparatus contained a spring connected lumped mass which has an accelerometer. The ice spheres were made to impact the lumped mass with a gas gun, which accelerated the projectiles. The impact force caused movement of the lumped mass, resulting in shortening of the spring. The impact forces on contact were a sum of the inertial force of the lumped mass and the reaction force caused by the shortening of the spring (Figure 2.17). The inertial force is determined from the accelerometer while the high speed camera provides information about the shortening of the spring. It is observed that a major part of the contact force is dominated by the inertial force and the reaction force formed only 10% of the contact force. However, the reaction forces were seen to last longer compared to the inertial forces. This can be seen clearly in Figure 2.18.

Following this, an analytical model was developed based on a 2-DOF spring connected lumped mass. This is illustrated in Figure 2.19.The spring connecting the impactor to the target displays visco-elastic behaviour and the parameters associated with it (k_n, p and D_n) were determined with a two-step calibration approach. From this, an algebraic expression for calculating

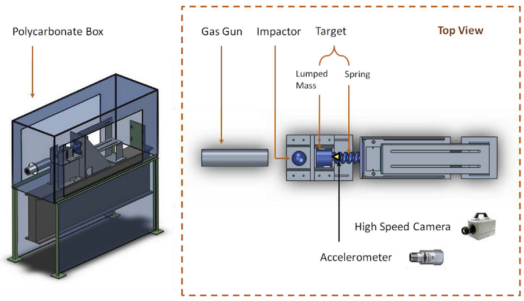

Figure 2.16: Contact force measurement apparatus [54]

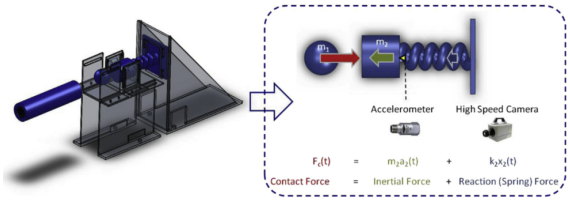

Figure 2.17: Equilibrium of forces acting on target [54]

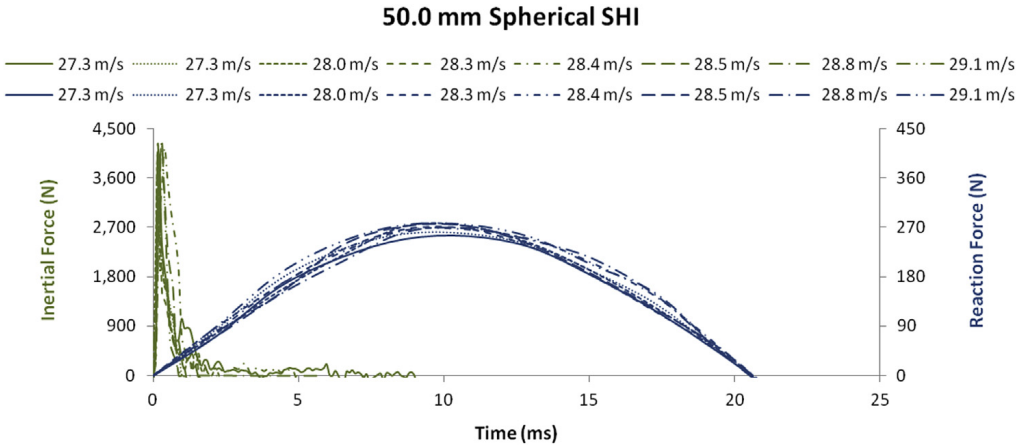

Figure 2.18: Depiction of inertial and reaction forces for a 50 mm hailstone[54]

peak force and a design chart to estimate peak forces for SHI ranging from 5 to 100 mm in diameter was presented (Appendix A).

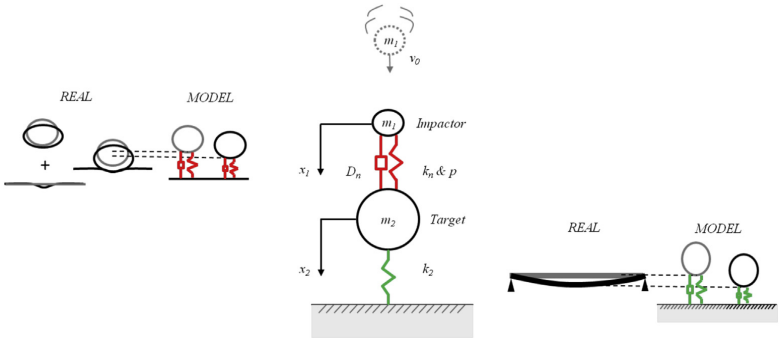

Figure 2.19: Illustration of 2 DOF spring-damper system used in analytical model [54]

2.3.2. Hail Impact on Composites

Composites have found widespread usage in the aerospace and wind energy industry. Though composites provide excellent in-plane mechanical properties, they are vulnerable to damage from out-of-plane loadings. This is seen in the form of barely visible impact damage (BVID) as matrix cracks, fibre failure and delaminations [55]. An extensive review of impact experiments on composites by Davies and Olsson [56] found that for the same impact energy, the response of a composite is different for a impactors with small mass and

moderate velocity and impactors with large mass and low velocity. This is explained by the shorter impact times of lower mass projectiles, resulting in a wave controlled response of the laminate and thus, a higher peak load. The damage caused by such impacts are seen in the form of matrix cracks and ply separation due to delaminations. Fibre cracking is seen at more intense testing parameters, which can result in a reduction of strength of 1/3rd in the composite [57]. Jackson and Poe [58] found that for large-mass impacts at low velocities on composite panels, increasing the impact force increases the extent of delamination seen. This delamination decreases with increasing plate size.

Macdonald et al.[50] investigated the effect of repeated impact of SHI on tri-axial glass-fibre composites. Hailstones of four different sizes (5, 10, 15 and 20 mm diameter) were fired at velocities calculated with respect to their terminal velocities and typical wind turbine tip speeds. The hailstones were fired using a vertically oriented experimental setup. A force transducer was used to measure the impact force. It was observed that the difference in range of peak force was quite noticeable for each hailstone size. Mass loss measurements did not reveal any signs of material loss.

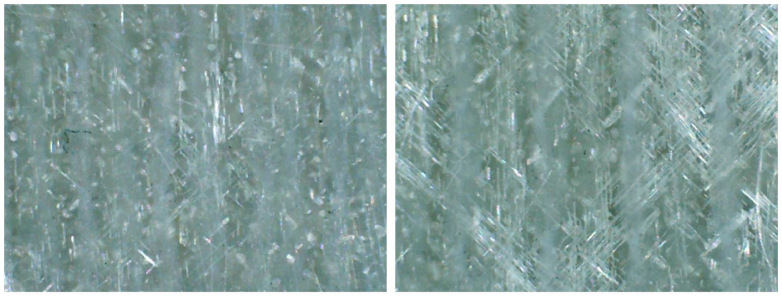

(a) Before (b) After

Figure 2.20: Oblique marks observed for 50 impacts of 15mm hailstone at a mean velocity of 85.6 m/s [50]

Optical microscopy revealed oblique marks in the 45° and -45° directions for 50 impacts of a 15 mm hailstone at a mean velocity of 85.6 m/s (Figure 2.20). Observing the samples using scanning electron microscopy revealed signs of fibre breakage at high mean velocity impacts of 15 mm and 20 mm SHI (at around 98 m/s and 87 m/s respectively). Pronounced matrix removal was seen for the case of 20 mm SHI at the largest number of impacts possible at low impact velocities (49.4 m/s). No clear surface damage was seen for the cases of 5 mm and 10 mm SHI, even though these are more commonly seen in meteorological studies. It is inferred from these observations that there exists a threshold velocity for each hailstone diameter and sample thickness, below which surface damage is negligible.

Kim et al. [59] conducted high velocity impacts of SHI on woven carbon fibre/epoxy panels. The different carbon-epoxy panels were manufactured to be as close to a quasi-isotropic layup. They noted that research focussing on metal projectile impact is vastly different to ice impact, owing to the disintegrating nature of ice and its material behaviour. To investigate the difference in impact force caused by this behaviour, force measurements on a dynamic force measurement transducer were carried out. Monolithic and flat-wise layered hailstones were manufactured for these tests.

For the force history recorded by the force measurement transducer for a 42.7 mm diameter layered SHI impacting at 73.5 m/s, it was seen that a peak impact force of 15.9 kN was recorded at 97 μs . Correlating this with the high speed footage of the impact between 91 μs

and 182 μs , it was seen that only a small portion of the front of ice sphere had impacted and fractured between these two time frames. The sphere was originally dyed blue (to aid velocity measurement) but whitens during the impact event. This is seen as a sign of micro-cracking in the sphere [60]. In further studies by Kim et al. [59], the time to reach peak force is seen to decrease with increasing impact velocities. Plotting the peak force for normal impacts against kinetic energy of impact results in a linear trend between the two (Figure 2.21). It is hypothesized that this linear relationship is valid for a range of high velocity SHI impacts on a particular composite panel.

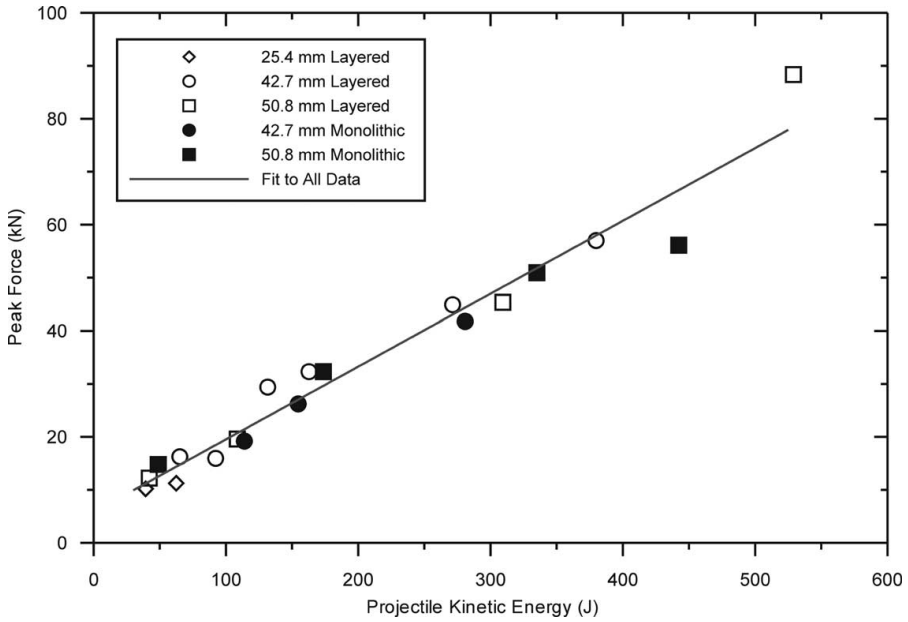

Figure 2.21: Plot of peak force vs kinetic energy for normal impacts [59]

The failure threshold energy (FTE) is determined for each distinct composite panel by impacting it at a velocity lower than the expected velocity at which delamination occurs. If no delamination is seen, the composite panel is subjected to a higher impact velocity and the procedure is repeated until damage is seen. For impact velocities below the FTE, no observable damage was seen. However, exceeding the FTE resulted in different types of damage modes (Figure 2.22). An almost linear trend is noted when plotting the FTE against the different panel thicknesses tested for each hailstone size. This can be seen in Figure 2.23.A steep slope in this trend is seen for SHI with smaller diameter. It is inferred that a SHI of smaller diameter is more lethal in initiating damage compared to a SHI of larger diameter, due to a lower FTE for a specified panel thickness. This is explained by the fact that the impact force is localized to a smaller area than a larger SHI. It is also observed during the experiments that the FTE for a specified panel thickness increases with an increase in SHI diameter.

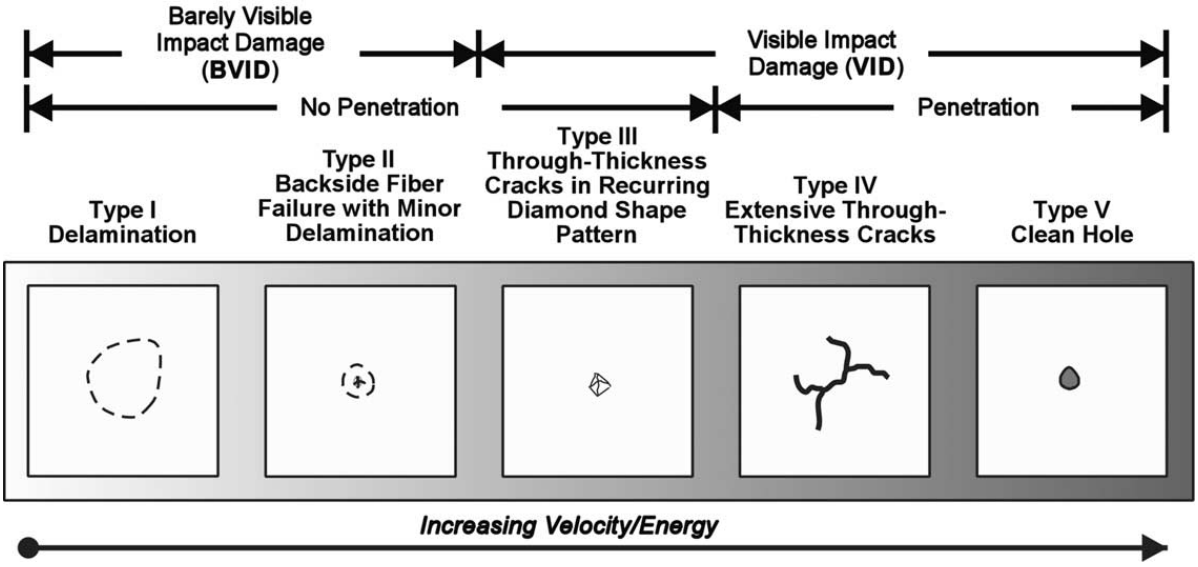

Figure 2.22: Damage mode progression observed by Kim et al.[59] for high velocity SHI impacts

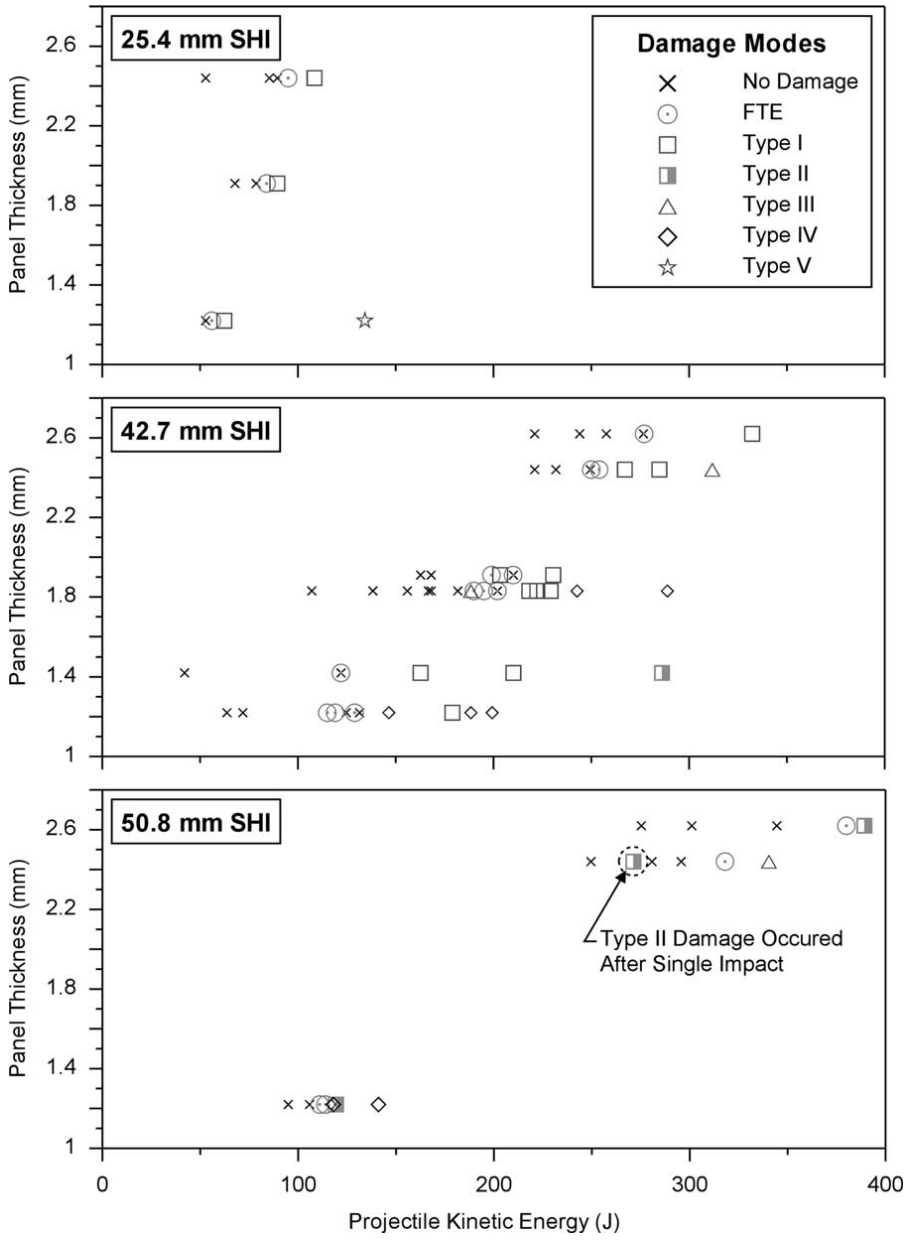

Figure 2.23: Plot of failure threshold energy vs panel thickness for different SHI sizes [59]

Kim et al.[53] also examined the difference in damage initiation from the impact of cotton-filled SHI and unfilled SHI. This difference in damage initiation was noted with respect to the failure threshold energy (FTE) and the corresponding damage mode. Impact experiments were conducted on woven carbon-fibre/epoxy panels. The cotton-filled SHI are made as per ASTM F320 [61] and dyed blue to aid velocity measurement. It was seen that the initial damage mode above FTE depended on the type of SHI used for impacts. Delaminations were observed as the initial damage mode for panels impacted by unfilled ice. Increasing the velocity led to a damage progression as seen in Figure 2.22. For a cotton-filled SHI, the initial damage mode was observed to be backside fibre failure (Figure 2.25). This difference in damage mode is attributed to the contact area over which the cotton-filled SHI impacts the composite panel, leading to larger localized deformations in the panel. This concentrated contact area is caused by the SHI being more intact after coming in contact with the target panel due to cotton acting as a reinforcement. This can be clearly seen in Figure 2.24. On the other hand, due to the large scale breakup of the unfilled SHI, the contact forces are spread over a wider area.

Figure 2.24: Backside fibre failure observed for cotton-filled 25.4 mm SHI at 71.6 m/s [53]

Figure 2.25: State of cotton-filled ice after impact, showing the deformation and that it is intact [53]

Numerical analysis by Kim et al.[10] found that the Failure Threshold Energy (FTE) and the interlaminar shear strain energy at the contact region of the panel are related to each other. Delamination occurs in the panel when the interlaminar shear strain energy exceeds a certain limit and the failure threshold is reached. The FTE recorded by Kim et al.[53] was normalized by the SHI diameter, density of ice and the interlaminar shear strength (τ_{ILS}) and shear modulus (G_{ILS}) of the composite panel. This normalized FTE, represented by α is written as Equation 2.7.

$$\alpha = \frac{\rho_{ice} V_{FTE}^2}{(\tau_{ILS}^2 / G_{ILS})} \tag{2.7}$$

This is plotted against the ratio of panel thickness H and SHI diameter D (Figure 2.26). It is observed from the plots that the unfilled SHI shows a linear trend between normalized FTE and H/D, whereas the cotton-filled SHI shows a non-linear trend and lower FTE values. Based on these observations, it is inferred than a cotton-filled SHI is more aggressive in initiating damage, especially in cases of small H/D values i.e. thin panels with large SHI diameter.

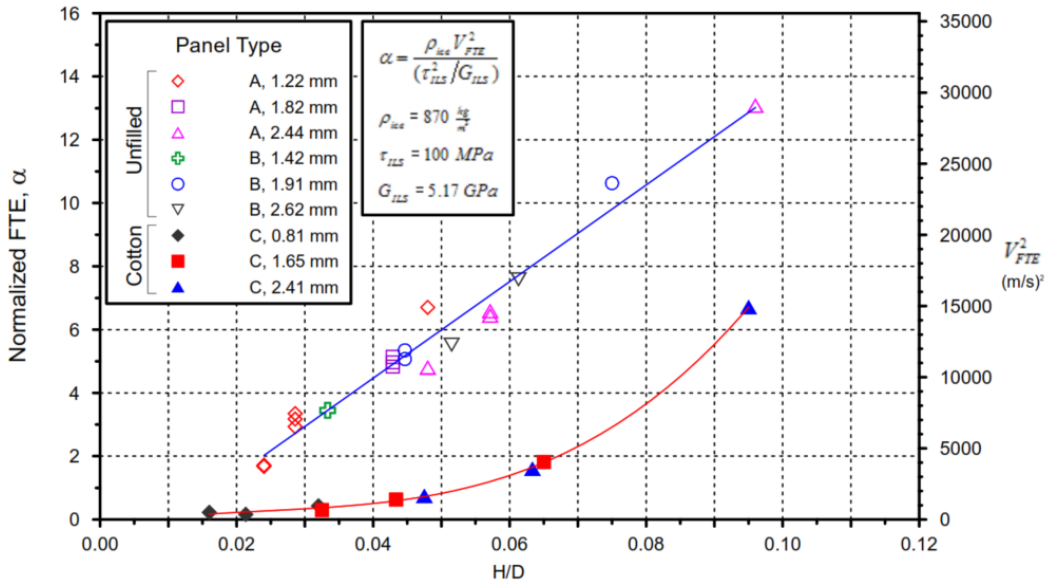

Figure 2.26: Plot of normalized failure threshold energy vs ratio of panel thickness and SHI diameter [53]

Kim and Kedward [55] studied the elastic response of composite panels subjected to hail impact by conducting numerical analysis and used it to formulate an analytical prediction of the failure threshold energy. This was predicted using the principle of conservation of energy. For the numerical analysis, an ice material model was created using DYNA3D. This was applied to predict the dynamic response of composite panels, subjected to SHI impact. The studies found interlaminar shear stress (ILS) in the composite to be a major cause for the formation of impact induced delaminations and occurs before bending induced surface strain. This correlated with experimental observations that delaminations are seen as the initial damage mode. Based on the analytical predictions, an expression was derived (shown in Equation 2.8). This shows a linear trend between the failure threshold energy and D^2H, with two empirically determined constants, α and β. α is the factor of velocity reduction on impact and β is a measure of the sphere deformation i.e. βD is the diameter of the ice sphere over which the average shear stress acts. D^2H is a combination of the geometric parameters (D is the sphere diameter and H is the panel thickness).

$$\text{FTE} = \frac{1}{1-\alpha^2}\left[\frac{\left(\tau_{\text{av}}^{\text{crit}}\right)^2}{8G_{xy}}\pi\beta^2 D^2 H + V_{\text{other}} - W_{\text{nc}}\right] = C_1 + C_2 D^2 H \tag{2.8}$$

2.4. Research Definition

The literature study signifies the importance for investigations into understanding the effect of hail impact on wind turbine blades and developing a knowledge base on coating resistance to hail impacts. With growing demand for wind energy and ever increasing wind turbine blade lengths, the risks to erosion and damage of wind turbine blades at remote locations is increasing. And with that, is the increase in costs for maintenance of the blades. Hailstone impact can severely affect the annual energy production of the wind turbine and thus, it is imperative to develop ways to protect the turbine blade against this form of damage. With climate change, hailstorms have become unpredictable and in extreme cases, large hailstones can occur which have the potential to cause heavy damage. Based on this, the following sections will elaborate on the research question, research objectives and the hypotheses involved in performing the planned thesis project.

The research question formulated based on the literature study on hail impacts on composites is as follows:

> *"What is the effect of varying hailstone sizes on the damage mode in leading edge polyurethane coatings subjected to hail impact?"*

In order to answer the main research question, a set of sub-questions are elaborated below.

1. Which parameters play a key role in understanding the dynamics of hailstone impact?
2. What role does kinetic energy play in damage initiation and progression?
3. What is the principal damage mode in the coating and the composite?
4. What is the damage evolution in the coated samples over the course of multiple hailstone impacts?

Based on the literature collected on the effect of hailstone size on damage initiation in composites, it is hypothesised that:

1. A larger hailstone is expected to cause more damage in the composite (in the form of delaminations, matrix cracking, matrix removal, scarring, fibre breakage) than a hailstone of a smaller size, when considering a fixed number of impacts and a specified impact velocity. This is due to the larger kinetic energy imparted by a larger hailstone.
2. The failure threshold energy for smaller hailstones is expected to be lower than the failure threshold energy for larger hailstones.

3

Methodology

Based on the literature review conducted, a research strategy was drawn up. The research strategy was based on commonly used experimental techniques to conduct hail impact studies and the availability of resources at the Delft Aerospace Structures and Materials Laboratory (DASML). The literature review showed that an impact gas cannon is commonly used to propel hailstones onto target composite panels. The following sections in this chapter go into the details on the experimental setup, method of manufacturing hailstones and the measurement techniques to quantify the impact parameters and damage, if any.

3.1. Research Strategy

An important decision that needed to be made in this study was the range of hailstone sizes and impact velocities to be used to achieve the research aims and answer the research question. From subsection 2.2.1, it was seen that hailstones with the size ranging from 5 mm to 9 mm have the highest frequency (when considering hailstones and not ice pellets). But, hailstones of these sizes are not known to cause any visible damage to typical glass fibre composites [50]. Considering the design limitations of the impact gas cannon, hailstones of 10 mm, 15 mm and 20 mm diameters were manufactured. During concept testing, it was seen that 10 mm hailstones are difficult to handle due to their small size and the shape and size of 10 mm hailstones are inconsistent. Most of it melts by the time the hailstone is fired. Therefore, after initial testing, the use of 10 mm SHI was discarded and only 15 mm and 20 mm SHI were used during the thesis project.

From Figure 3.1, we can see that the maximum blade tip speed for most of the commercially used wind turbines is between 85-95 m/s. The terminal velocity of hailstones of different sizes can be obtained from Equation 2.4, Equation 2.5 and Equation 2.6. Keegan et al.[41] noted that the maximum impact velocity for the hailstones occur when the blade is in a horizontal position at an angle of 270°. This example by Keegan et al.[41] was shown in subsection 2.2.3. For the sake of simplicity and the observation that the impact velocity didn't change by much, our calculations will involve no wind component of velocity. Using the equations described before and a blade tip speed of 85-95 m/s, it is seen that a 15 mm hailstone will have impact velocities between 101-111 m/s, whereas a 20 mm hailstone will have impact velocities between 113.5-123.5 m/s. Based on these calculations, 110 m/s was chosen as the impact velocity that will be tested initially.

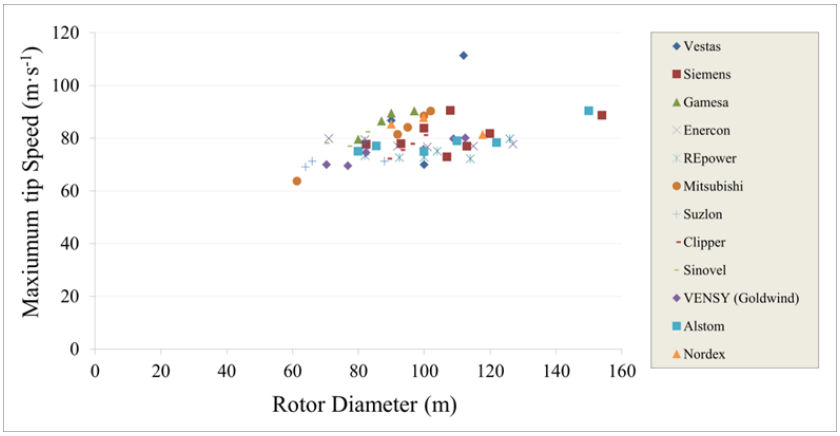

Figure 3.1: Maximum blade tip speed vs rotor diameter for different wind turbine operators [41]

In order to achieve the intended impact velocity, calibrations were performed with the has cannon to correlate the pressure values with the impact velocity. The hail impacts were recorded using a high-speed camera setup, which allowed observation of the impact event and calculate the impact velocity. The projectile kinetic energy was calculated from this impact velocity and the mass of the hailstone which was also noted. Research by Macdonald et al.[50] found that the mass change in the GFRP composite, caused by hail impact is negligible and in some cases, there was a mass increase of upto 0.02%. Therefore, non-contact profilometry was used to analyze the front and rear surface of the sample. The samples were analyzed and checked for damage after a set number of hail impacts. An overview of the hail impact experiments conducted and the analysis methods followed is presented in Table 3.1. The cross-sections of the samples were later analyzed to get an in-depth idea about the damage type and location of damage.

Sample name	Hailstone diameter	Number of impacts	Intended Impact Velocity	Optical microscopy after n impacts	C-scan after n impacts
B3	20mm	10	110 m/s	0,1,2,3,4,5,6,7,8,9,10	0,1,3,5,7,10
B4	20mm	10	110 m/s	0,1,2,3,4,5,6,7,8,9,10	0,1,3,5,7,10
B5	20mm	10	110 m/s	0,1,2,3,4,5,6,7,8,9,10	0,1,3,5,7,10
C1	20mm	10	110 m/s	0,1,2,3,4,5,6,7,8,9,10	0,1,3,5,7,10
C2	15mm	15	110 m/s (10 impacts) followed by 120 m/s (5 impacts)	0,1,2,3,4,5,6,7,8,9,10,15	0,1,3,5,7,10,15
C3	15mm	15	110 m/s (10 impacts) followed by 130 m/s (5 impacts)	0,1,2,3,4,5,6,7,8,9,10,15	0,1,3,5,7,10,15
C4	15mm	15	110 m/s (10 impacts) followed by 140 m/s (5 impacts)	0,1,2,3,4,5,6,7,8,9,10,15	0,1,3,5,7,10,15
C5	15mm	15	110 m/s (10 impacts) followed by 150 m/s (5 impacts)	0,1,2,3,4,5,6,7,8,9,10,15	0,1,3,5,7,10,15
D1	15mm	10	160 m/s	0,1,3,5,7,10	0,1,3,5,7,10
D2	15mm	10	160 m/s	0,1,3,5,7,10	0,1,3,5,7,10
D3	15mm	10	160 m/s	0,1,3,5,7,10	0,1,3,5,7,10
E1	20mm	5	90 m/s	0,1,3,5	0,5
E2	20mm	5	90 m/s	0,1,3,5	0,5
E5	20mm	5	90 m/s	0,1,3,5	0,5
E3	20mm	5	100 m/s	0,1,3,5	0,5
E4	20mm	5	100 m/s	0,1,3,5	0,5

Table 3.1: Overview of hail impact experiments conducted

3.2. Experimental Setup

This section describes the target material and provides some context behind the application of the coating. Then, subsection 3.2.2 describes the configuration of the impact gas cannon, the impact chamber and the high-speed camera setup.

3.2.1. Test Samples

The samples being tested in this project are glass fibre reinforced plastic (GFRP) composites, coated with polyurethane. The samples used in the research project are 8.9$\pm$0.6 cm x 8.4$\pm$ 0.4 cm in size [62]. An example of such a sample can be seen in Figure 3.2. The sample shown is 8.8 cm x 8.5 cm in size. The biaxial GFRP composites were manufactured by Suzlon and have a layup sequence of [-45/+45]$_4$. This is a layup that is typically found in the leading edge of a wind turbine blade. These samples were subsequently coated with an industrial polyurethane coating by 3M. The PU coating (W4600 WBPC) is a two-component polyurethane coating that is applied post-mould. From the datasheet [25], it is noted that the glass transition temperature (T_g) is $-5°C$. The datasheet also details the recommends the applied coating thickness to be between 250 to 350 μm [25]. This is found to correspond to the thickness of the coating in the tested samples (310 $\pm$ 40 μm). The GFRP substrate is about 2.5 mm thick (2.53 $\pm$ 0.03 mm). This is shown in Figure 3.3. A woven fabric layer with fibre bundle diameter larger than the diameter of the fibres seen in the layers above is the last layer at the back of the sample and doesn't have a uniform thickness throughout. Table 3.2 details some of the mechanical properties of the polyurethane coating.

Mechanical Property	Value
Density,ρ_c	1100 kg/m^3 [41]
Young's modulus, E	32 MPa [41]
Poisson's ratio, ν	0.3 [41]
Failure strain, ε_f	700% [41]
Tensile Strength, σ_U	37 MPa [25]

Table 3.2: Mechanical properties of polyurethane coating

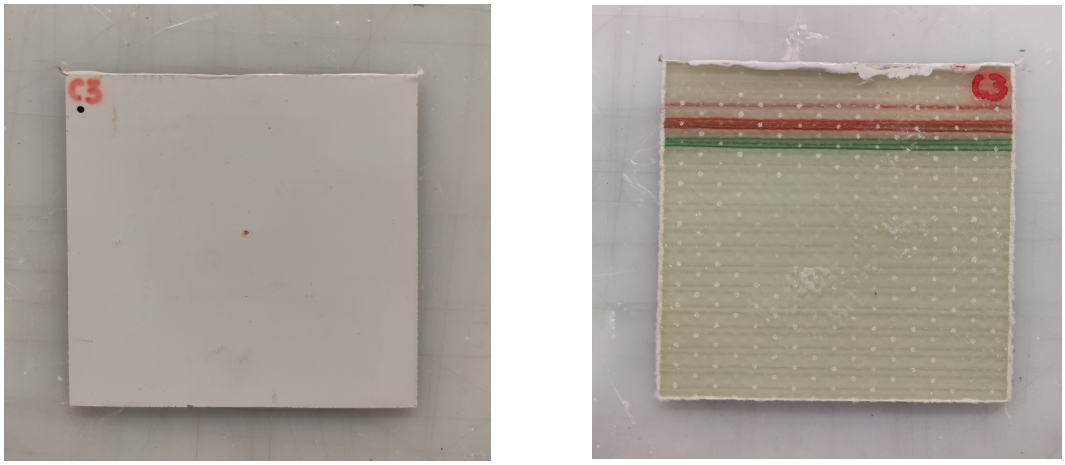

(a) Front Side of Sample

(b) Back side of Sample

Figure 3.2: Polyurethane coated GFRP specimen (8.8 cm x 8.5 cm in size). The front side has the white PU coating on it.

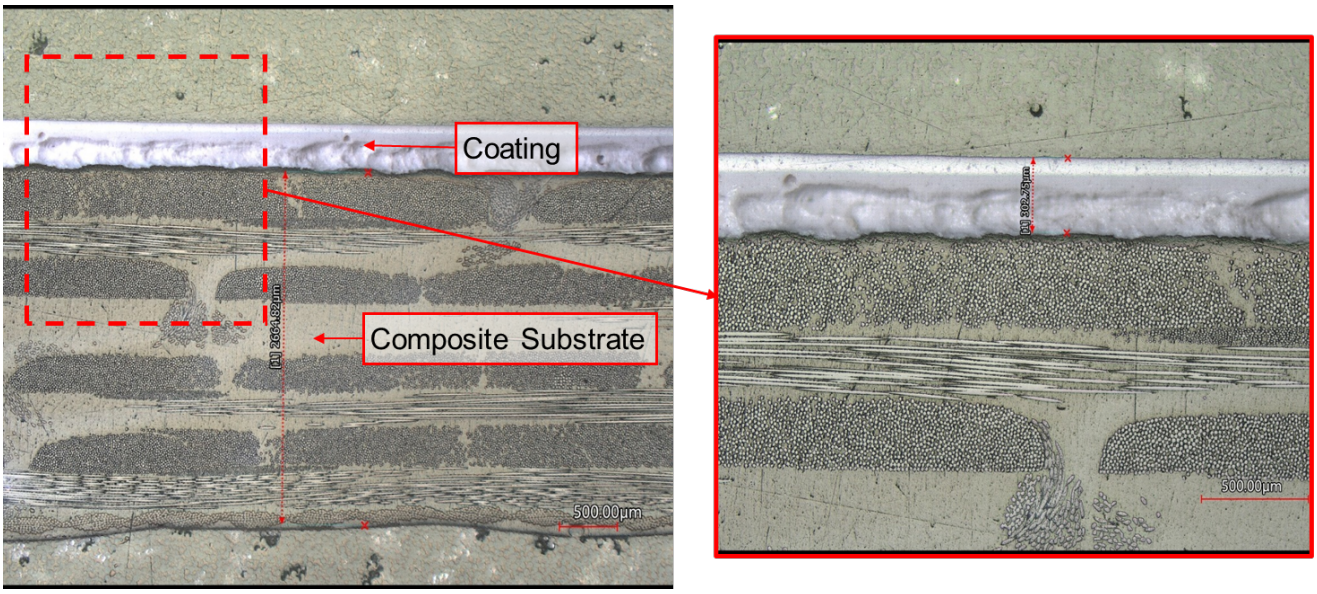

Figure 3.3: Cross section of a test sample. Left - Cross section showing thickness of substrate (2664.82 μm) and Right - Cross-section showing thickness of coating (302.75 μm)
(Scale bar depicting 500 μm)

3.2.2. Experimental Apparatus

This section provides background on the experimental apparatus used during the thesis project: the impact gas cannon and the high speed camera.

Impact Gas Cannon

The impact gas cannon at the Delft Aerospace Structures and Materials Laboratory (DASML) was used to conduct hail impact experiments on the PU coated GFRP samples. As discussed in chapter 2, the gas cannon approach was typically used to conduct such experiments. The gas cannon is mounted on a movable frame and is mainly composed of the following components (Figure 3.4):

- Barrel: The barrel is made of stainless steel and is about $\approx$750 mm in length and has a inner diameter of 25.4 mm.
- Pressure chamber: The pressure chamber is used to store compressed air and can be pressurised upto 30 bar.
- Pressure regulating system: The pressure regulating system allows us to monitor the pressure inside the pressure chamber and gives control over the pressure at which the projectile is shot at.
- Firing valve: The firing valve separates the pressure chamber from the barrel and acts like a switch until the firing trigger is turned.
- Fill valve: The fill valve is used to fill the pressure chamber with compressed air. This can be from the central system (maximum pressure of about 9 bar) or from a tank of compressed air (maximum pressure of 30 bar).
- Empty valve: The empty valve is used to reduce the pressure inside the pressure chamber without firing the gas cannon. This can be used to reduce the pressure in case of overfill.
- Trigger: Turning the trigger allows the projectile inside the barrel to be fired, by the compressed air present inside the pressure chamber.

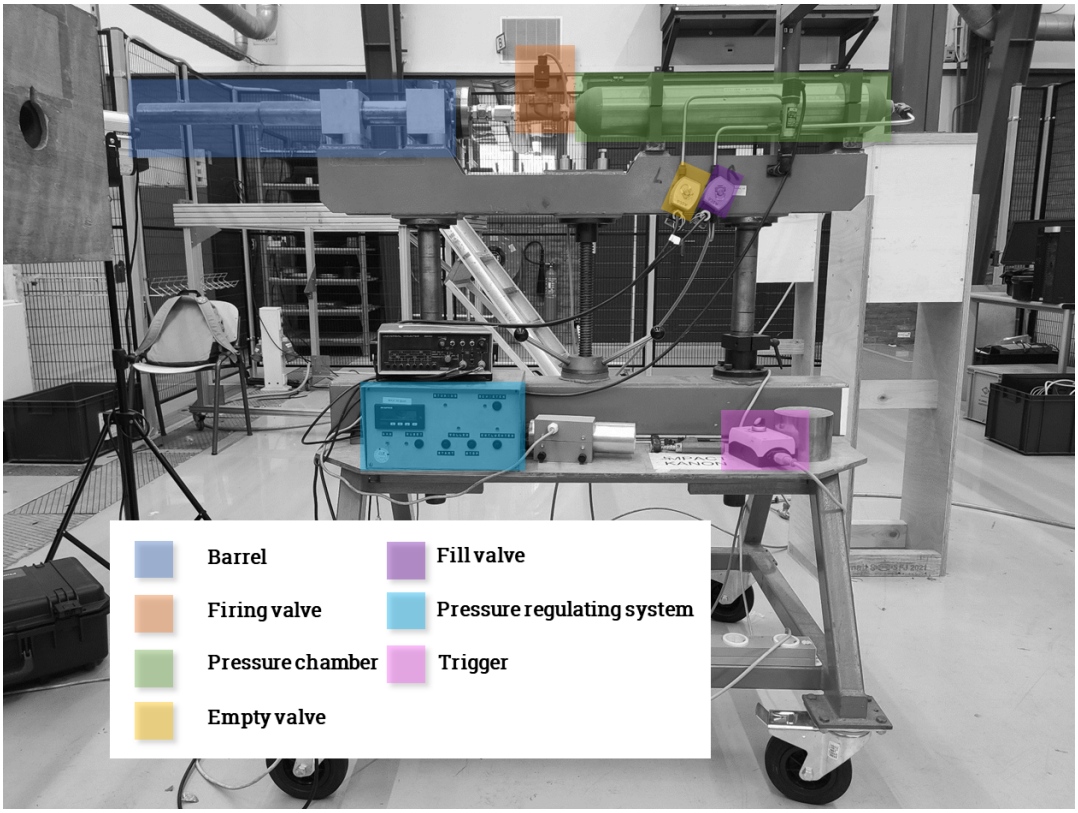

Figure 3.4: Impact gas cannon at DASML

The projectile was fired inside the impact chamber, which is mounted on a rigid frame and is cushioned inside with foam. The barrel was placed inside the gas cannon through a hole and is oriented towards the target by moving the gas cannon. The gas cannon was moved such that the tip of the barrel is placed at a distance of 420 mm from the sample. This is the least distance that is possible for the given setup. The sample was mounted inside the impact chamber using the bracket and wooden support. The test sample is clamped between two such substructures and is fixed in position against the aluminium backing structure using T-bolts. This is shown in Figure 3.5. It was seen by Kim et al.[10] that the panel boundary conditions do not influence the failure mode or threshold energy. This is due to the localized deformation around the region of impact. Thus, the samples are held in such a way that the left and right sample edges are constrained to resist bending, yet in-plane freedom is permitted. The position of the substructure corresponding to a hail impact at the centre of the specimen is marked. This central point is determined with the help of a laser pointer. A scale is attached to an aluminium substructure to monitor the position of the impacting hailstone, when the impact event is recorded by the high speed camera.

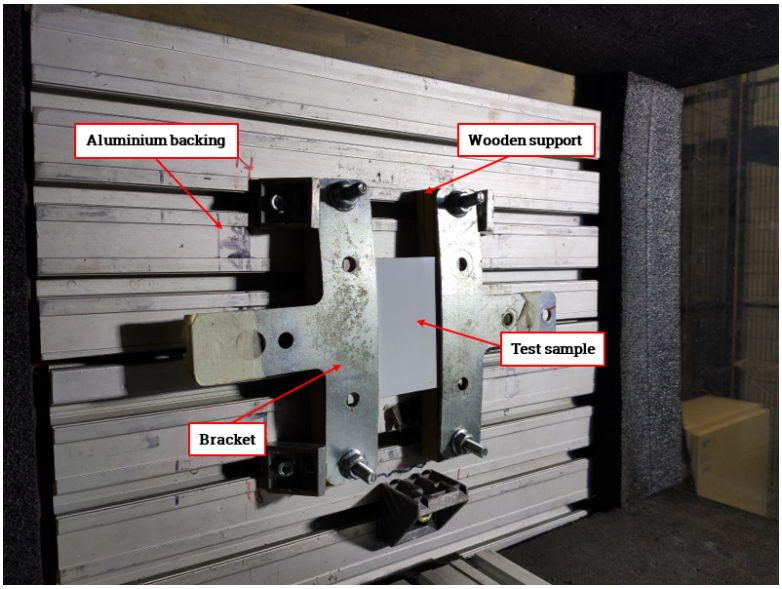

Figure 3.5: Mounting of target sample inside impact chamber

High Speed Camera

A high speed camera (Photron FASTCAM Nova S6) was used to record the hail impact event and measure the impact velocity of the hailstone (Figure 3.6). This could record upto 3 seconds of the impact event. Therefore, the turning of the trigger and the start of the recording needs to be timed properly to get the required high-speed footage. The high-speed camera is placed at a 90° angle to the impact chamber and it's height is adjusted to capture the moving hailstone throughout it's impact length. The footage obtained from the high speed camera was also used to evaluate the shape of the hailstone before impact. Recording this at 20000 fps (Resolution of 640x480) was seen to be sufficient to clearly observe the moving hailstone and calculate the velocity. However, some impact velocities (e.g 160 m/s) were recorded at 24000 fps (Resolution of 512x480).

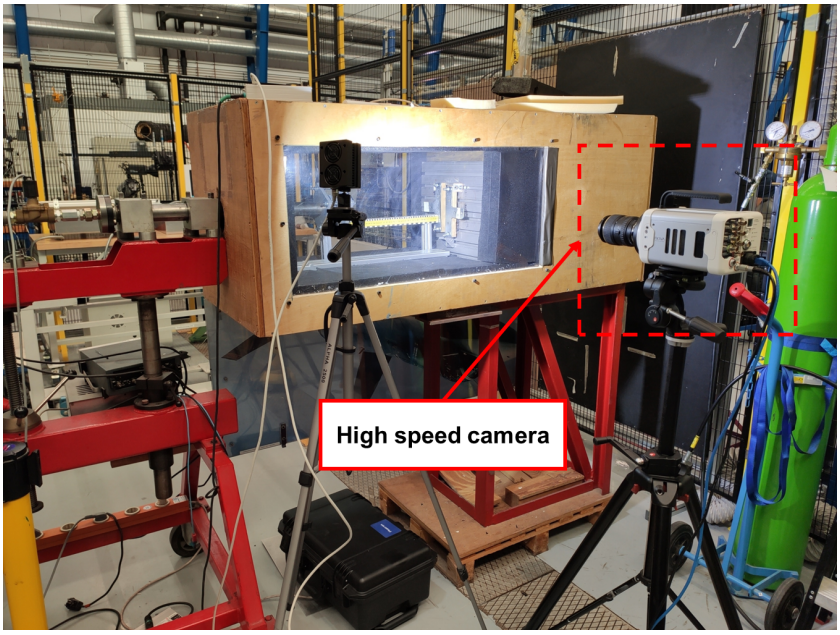

Figure 3.6: High speed camera setup to observe hail impact

3.3. Manufacturing Hailstones

Hailstone occurring naturally have an onion-like layered microstructure, which lends to its toughness. This has been found to be difficult to replicate in lab condition. Lab-made ice, also called Simulated Hail Ice (SHI), is manufactured using two 3D printed moulds made of PLA. The mould designs are obtained from the work of Eryörük [63]. The ice spheres are made in a single filling session with de-ionized water, leading to the formation of monolithic ice. De-ionized water is used instead of tap water as the minerals present in tap water can potentially weaken the hailstones and reduce its compressive strength. The ASTM standard F320-21 [61] describes the test method to be followed to determine the impact resistance of aerospace transparent enclosures (windshields, windows, etc.). The use of cotton fillers to reinforce the SHI is also suggested. However, research by Kim et al. [53] found that impact of cotton-reinforced hailstones on Carbon Fibre Reinforced Plastic (CFRP) composites are significantly more lethal than unfilled ice and are not the most suitable representation of naturally occurring hailstones. Usage of ceramic or metal beads are found to be unsuitable as the material behaviour is vastly different from that of ice, even if considering same diameters and kinetic energy [41]. Thus, de-ionized water is chosen for filling the hailstone moulds.

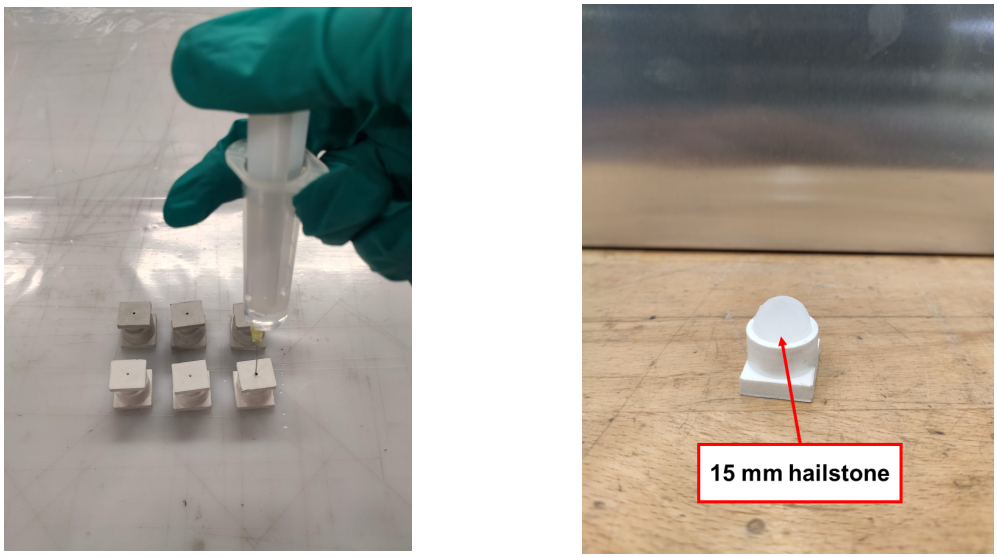

(a) Filling hailstone mould through a syringe

(b) 15 mm SHI before demoulding

Figure 3.7: Manufacturing of hailstones

De-ionized water was filled into the mould through a small opening with the help of a syringe. This is illustrated in Figure 3.7a. The mould was slightly under-filled to account for the volumetric expansion of water during phase change. This was then placed in a freezer at $-22°$C for at least 5 hours. After removal from the freezer, the moulds were weighed with the hailstone inside and then weighed again. This is because transferring the hailstone to a ziplock bag led to slight flattening of the hailstone on the side it was resting at, when placed inside the freezer. The hailstone moulds were kept in the freezer for another hour before being removed for usage in the test. The mould was kept in room temperature for a few minutes before the two halves could be separated. It was quickly inspected for cracks and voids before being pushed inside the barrel with a PVC cable.

3.4. Challenges with gas cannon & modifications to setup

As described in subsection 3.2.2, the barrel of the gas cannon is made of stainless steel. This poses a challenge as the SHI starts melting on coming in contact with the barrel directly. This was due to the conductivity of the barrel. Thus, a different method to place the hailstone inside was needed to be thought of. ASTM F320-21 [61] describes the usage of a sabot as a carrying case for the SHI. This approach was found by Eryörük [63] to be unsuitable for hail impact in the given impact chamber due to the amount of debris flying inside. Finally, an acrylic tube with an outer diameter of 24.6 mm was used. This acrylic tube was used to insert a 20 mm hailstone inside the barrel. For a 15 mm hailstone, a thinner tube (outer diameter of about 20 mm) with a 3D printed casing was used to keep the tube at the centre. This was because the acrylic tube used for a 15 mm hailstone is smaller than the diameter of the barrel and thus, needs a casing to match the inner diameter of the barrel. These adaptions to the setup are shown in Figure 3.8 and Figure 3.9.

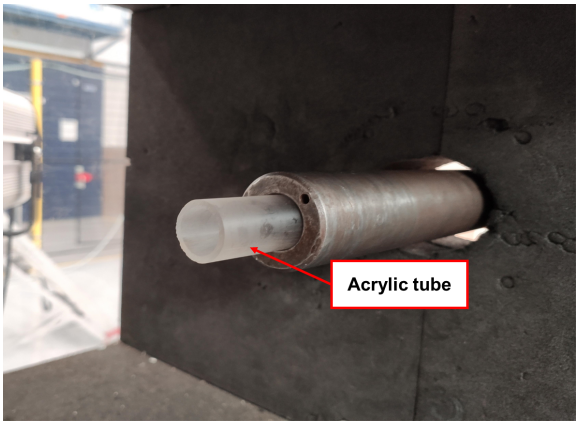

Figure 3.8: Acrylic tube for 20mm hailstone

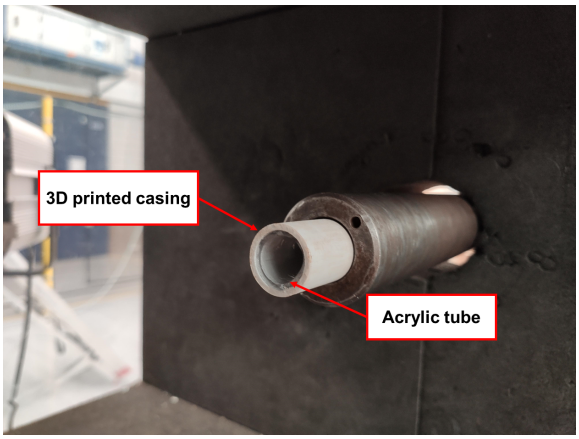

Figure 3.9: 3D printed casing around acrylic tube for 15mm hailstone

An aluminium plate assembly was designed with a hole to prevent the acrylic tube from shooting out, along with the hailstone (Figure 3.10). This assembly is mounted on the barrel. To note the position of the hailstone, an aluminium substructure with a scale is placed close to the sample. This is illustrated in Figure 3.11.

Figure 3.10: Aluminium plate assembly

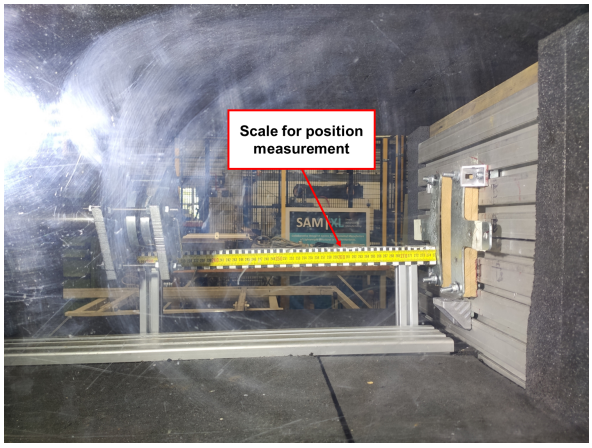

Figure 3.11: Positioning of scale near sample

3.5. Measurement Techniques

3.5.1. Mass measurement

Mass measurement of the hailstone samples allows us to calculate the projectile kinetic energy, which is an important quantity for characterizing impact events. As discussed in section 3.3, flattening of hailstones was observed when they were transferred to a ziplock bag and placed inside the freezer. Therefore, the mass of the hailstones had to be measured indirectly. The hailstone moulds are weighed at the start of the test day. This is performed by measuring the mass of the hailstone with the mould, when it has been frozen inside the freezer for at least 5 hours. This has to be performed quickly to prevent the hailstone from melting. When the hailstone is demoulded and used for the impact event, the moulds are weighed again to get a measure of the empty mass of the mould. Subtracting this from the previously measured mass gives us the mass of the hailstone. This can be understood from Equation 3.1, where m_h is the mass of the hailstone, m_hm is the mass of the hailstone with the mould and m_m is the mass of the empty mould. A small sample size of the mass measurements carried out can seen in Appendix C.

$$m_h = m_{hm} - m_m \tag{3.1}$$

3.5.2. Velocity Measurement

The high speed camera setup described in Figure 3.2.2 is used to record the impact event. The aluminium substructure with the scale allows noting the position of the hailstone with respect to the sample and calculate the distance moved by the hailstone in each frame. The velocity of the hailstone is calculated from the difference in position of the moving hailstone divided by the time taken for this change in position. This is given by,

$$v = \frac{dx}{dt} \tag{3.2}$$

To explain this, an example measurement from the research is considered. This is shown in Figure 3.12 and Figure 3.13, where a 20 mm SHI is impacting the sample. The frame rate of measurement here is 20000 fps i.e. one second of recording constitutes 20000 frames. An inverse of the frame rate means that there is 0.00005 seconds or 0.05 msec between each frame. The impact velocity is calculated based on the distance covered in the last 0.25 msec (or the last five frames) before impact with the sample. This is because of the reduction in velocity due to the air present inside the chamber. The actual impact velocity is lower than the velocity at which the hailstone leaves the barrel. Looking at Figure 3.12, we see that in frame no. -46109, the end of the hailstone is at a position coinciding with 272.6 cm on the scale. In Figure 3.13, the hailstone in frame no. -46104 is at 274.8 cm on the scale. This means that the hailstone has travelled 2.2 cm in 0.25 msec (5 frames between the two frames shown). Using Equation 3.2, the impact velocity is determined to be 88 m/s. The impact velocity for all impact events is calculated in a similar manner from the high-speed footage. The error in velocity measurement is noted to be $\pm$2 m/s.

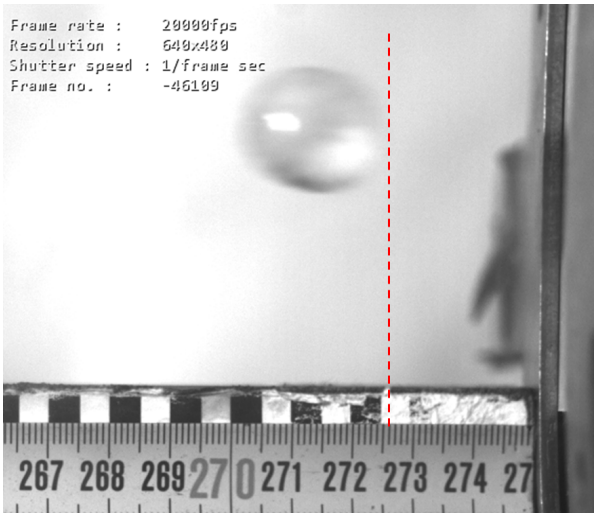

Figure 3.12: 20 mm SHI in frame no.46109, coinciding with 272.6 cm on scale

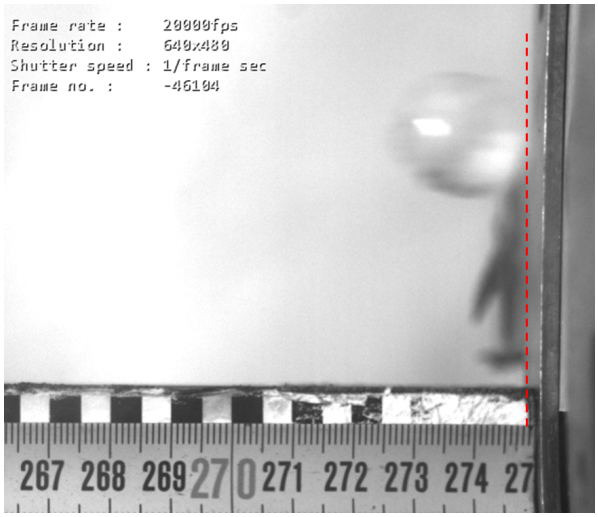

Figure 3.13: 20 mm SHI in frame no.46104, coinciding with 274.8 cm on scale

The gas cannon has metal projectiles for which calibration data were already available. However for hailstones, calibrations have to be performed to determine the pressure corresponding to the impact velocity of the hailstone. The velocity of each hailstone was measured by collecting high speed footage of the impact experiments. The pressure values at these velocities were noted to comprehend the required pressure threshold in the gas cannon. This is plotted and shown in Figure 3.14. The raw data for the calibration can be seen in Appendix B.

From the graphs, we can see that to obtain an impact velocity of 110 m/s, a pressure of 4,63-4.87 bar and 7.1-7.2 bar is required for a 15 mm and 20 mm SHI, respectively. These pressure values were obtained by setting the pressure regulating system to the required pressure and turning the trigger when this pressure was reached. Over the duration of the thesis, it was noticed that due to rising temperatures in the summer, this pressure led to a slightly higher impact velocity caused by the melting and thus, reduction in size of the hailstones. This was corrected by re-calibrating around the required velocity values and thus, reducing the pressure to compensate for the quicker melting of the hailstones. An effort was made to ensure the achieved impact velocity is as close as possible to the intended impact velocity.

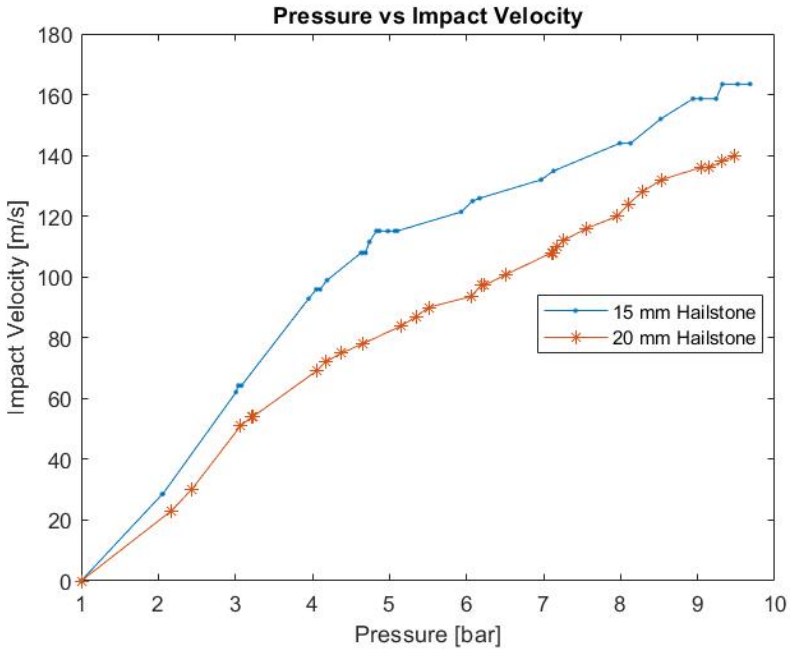

Figure 3.14: Pressure vs velocity calibration of 15 mm and 20 mm SHI with gas cannon

3.5.3. Optical microscope and Laser confocal microscope

The coating side of the sample is analysed using the wide-area optical microscope (Keyence VR-5000) (Figure 3.15a). This microscope allows high-resolution wide-area measurement and allows the entire surface of the sample to be scanned. The 3D measurement system also investigates the height profile of the inspection area. In the case of coating damage, the damage area and volume of material removal can be measured and a contour map of this area can be generated.

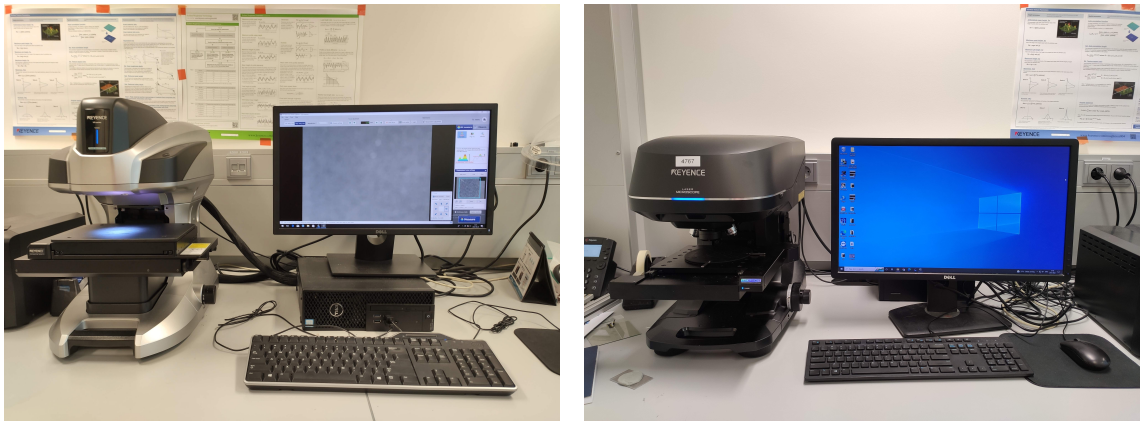

(a) Keyence wide-area microscope **(b)** Keyence laser confocal microscope

Figure 3.15: Microscopes used for damage analysis

A laser confocal microscope, Keyence VK-X1000 (Figure 3.15b) is used to analyze the rear surface and cross-section of the samples. The rear surface was found to be difficult to analyze with the wide-area microscope due to the brightness and scatter of light from the microscope. The laser confocal microscope provides detailed images through confocal scanning (also called focus variation). This gives high-resolution images with height variation, even at

high magnification. The drawback of this microscope is that it doesn't have a wide area of measurement compared to the Keyence VK-5000 and is also comparatively slower. Thus, only the central region near the zone of impact is scanned using this microscope.

3.5.4. Ultrasonic C-scan

Ultrasonic C-scan (Olympus Epoch 650) is used to check for delaminations and porosity in the test samples (Figure 3.16). A 10 MHz probe is used in a pulse-echo transducer. Considering the speed of sound in water to be 1480 m/s, the wavelength of the ultrasonic beam is calculated to be 148 μm. The samples are clamped to an iron bar (which is fixed to an aluminium frame) and submerged in water. This is because water acts a good coupling medium for the ultrasonic waves to travel through. The output of the c-scan is obtained in terms of signal strength values (dB), as the ultrasonic signal travels through the composite.

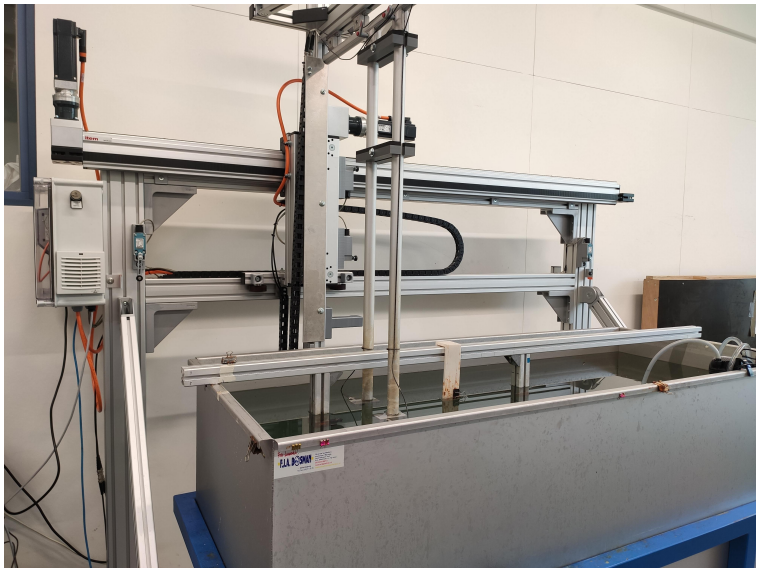

Figure 3.16: Ultrasonic C-scan

3.5.5. Sample Preparation & Cross-Sectional Microscopy

In order to get an in-depth idea about the type of damage and damage location, resin mounts of the sample are created. For this, the sample needs to be prepared. Sample preparation consists of sectioning and mounting. The sample is first cut with a cutting machine. This is performed using the Secotom-10 cutting machine (Figure 3.17). During sectioning, it is important to ensure that the damage features are not affected. A lubricant or coolant is used for cooling the samples. The samples are cut according to the schematic shown in Figure 3.19. The green lines indicate the oblique lines that are seen while scanning the backside, while the red dashed lines are the cutting lines. The arrows indicate the side which will be inspected under the microscope. The yellow circle at the centre indicates the central point of impact of the sample. The numbers inside highlight the section number.

Figure 3.17: Secotom-10 cutting machine

Figure 3.18: Tegramin-20 grinding and polishing machine

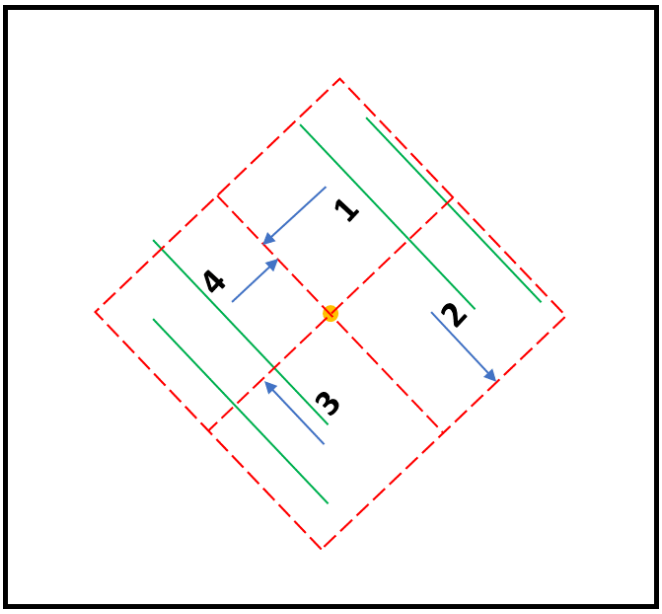

Figure 3.19: Creating cross-section of samples around damage zone

The cut samples are cleaned in an ultrasonic bath and then placed in a mould. The mould is filled with the resin and allowed to cure. After about 30 minutes, the mount samples are removed from the moulds. Mounting of the sample allows easy handling of the cut parts before the grinding and polishing step. Grinding and polishing is performed using the Tegramin-20 grinding and polishing machine (Figure 3.18. Grinding is done using various grades of grinding paper. Water is used as a coolant during the grinding process. Polishing of the mounts is performed using the same machine using polishing cloth. Here, different grades of diamond paste are used. This paste consists of fine particles which aid in the polishing process. Once the sample has been polished sufficiently, it is cleaned with ethanol to remove any contaminations. An example of a final mount sample is shown in Figure 3.20.

The mount samples are observed using the laser confocal microscope described in subsection 3.5.3. High-resolution images of the cross-sections were analyzed to evaluate possible damage modes and location of damage in the samples. The cross-sectional observations

Figure 3.20: Cut samples embedded in resin

were made using coaxial light as this provides detailed pictures without reflection from the polished surface of the cross-sections.

4

Results

The research strategy and methodology described in the previous chapter are followed to conduct hail impact experiments and analyze the coated composite samples. This chapter presents the observations from the experiments and the subsequent measurement techniques. An overview of the test results can be seen in Table G.1(for 15 mm SHI impact results) and Table G.2(for 20 mm SHI impact results). An illustration of a typical high-speed impact experiment is provided in Figure 4.1.

Figure 4.1: (a-f)High-speed images of simulated hail ice impact, depicting impact and deformation of hailstone. Here, the hailstone diameter is 20 mm and the impact velocity is 88 m/s

4.1. Optical Microscopy

The coatings side of the samples were scanned and inspected by optical microscopy before the first hail impact. This was done to generate a height map of the samples and compare differences in topography, if any caused by repeated impacts. An example of this is shown in Figure 4.2 for sample D3. As can be seen, the sample height is uniform, while no observable deformity can be seen in the coating. The scan of the central zone of the rear of the sample shows no visible damage (Figure 4.3). Only dry spots can be seen on this side.

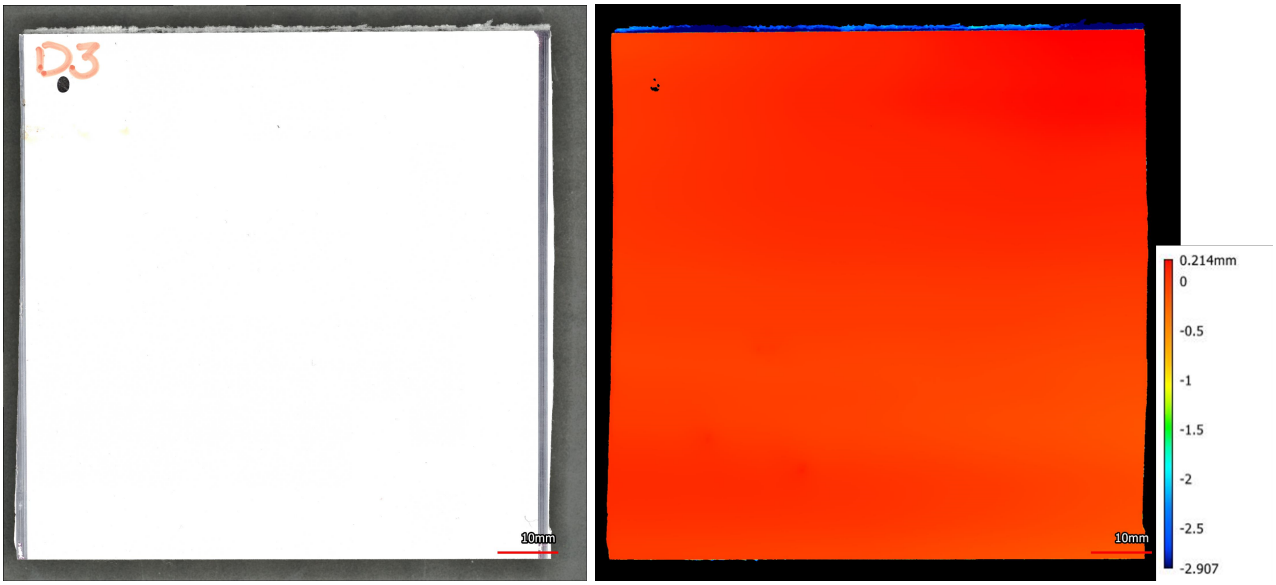

(a) Optical microscope scan of sample **(b)** Height map of sample

Figure 4.2: Optical microscopy pictures of Sample D3 before impact

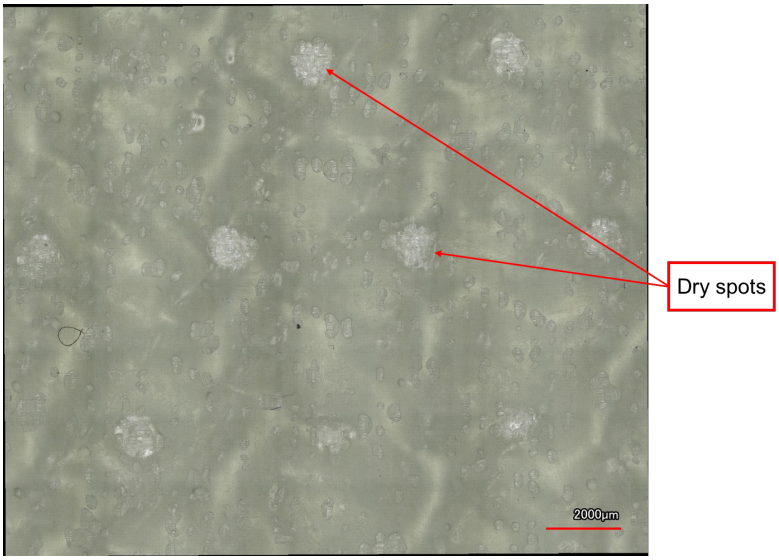

Figure 4.3: Optical microscopy picture of rear of Sample D3 before impact

After 10 impacts of 15 mm SHI at a mean impact velocity of 162 m/s (with the highest impact velocity being 163 m/s), no difference in the coating layer is observed (Figure 4.4a). The height map virtually remains the same (Figure 4.4b). However, the optical microscopy image of the rear (Figure 4.5) had some interesting observations. Faint lines at oblique angles (-45°) are seen in the rear of the sample. A closeup image of this is shown in Figure D.39. This is similar to what was observed by Macdonald et al.[50] and shown in Figure 2.20. These lines could be located by using a pointed, focussed light (like the coaxial light from a laser confocal microscope). These lines are identified as signs of matrix cracking and are investigated further by observing cross-sections of the samples(discussed in section 4.3). Another interesting observation is that these lines appear slightly away from the impact zone. Such lines were not observed by optical microscopy in samples impacted by 15 mm SHI at velocities lower than 160 m/s.

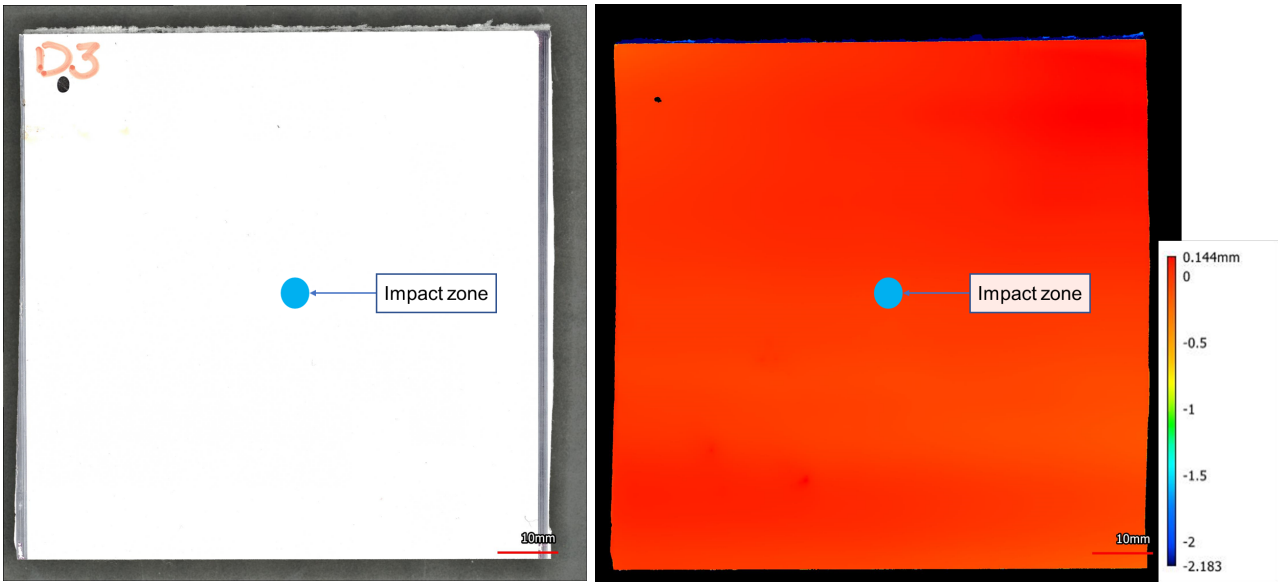

(a) Optical microscope scan of sample **(b)** Height map of sample

Figure 4.4: Optical microscopy pictures of Sample D3 after 10 impacts of 15 mm SHI

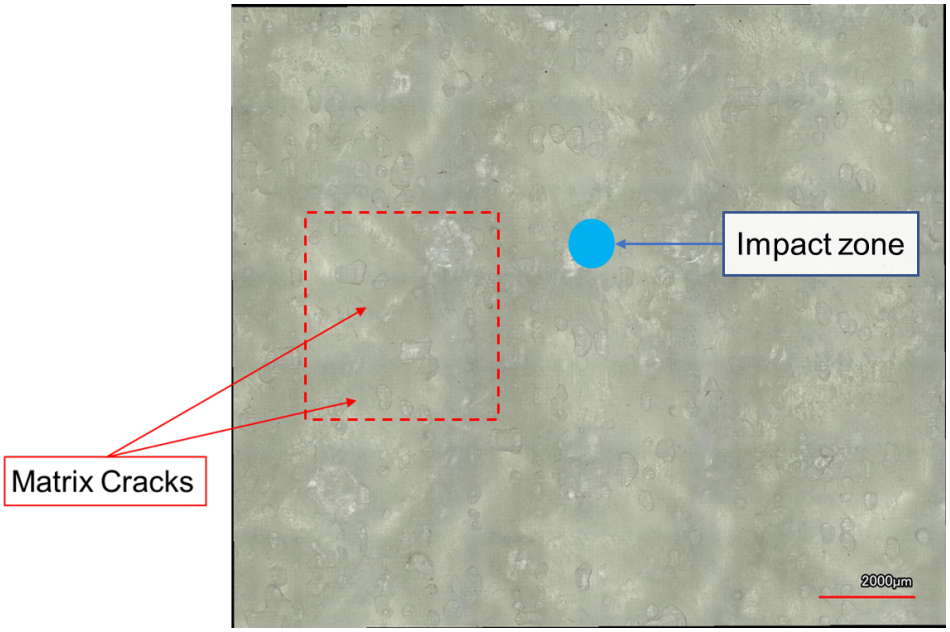

Figure 4.5: Optical microscopy picture of rear of Sample D3 after 10 impacts of 15 mm SHI, showing matrix cracks in -45° direction

Considering the cases which are to be impacted by 20 mm SHI, the same procedure was repeated. The sample shown has been impacted 10 times with 20 mm SHI at a mean impact velocity of 112 m/s (highest impact velocity of 120 m/s). Comparing Figure 4.6 and Figure 4.7, a difference is observed compared to the previous case of a 15 mm SHI impact. The height map shows a change in the topography of the coating (noticeable by the change in height colour) after the hailstone impacts. No visible coating damage is observed.

The optical microscopy image of the rear of the sample (Figure 4.8) shows more distinct marks of matrix cracks, compared to the previous case. These lines at oblique angles are more

frequent and scattered around the central point of impact (similar to the previously shown example). A closeup image of the matrix crack reveals whitening of the matrix surrounding the crack. To know the minimum velocity for this size of hailstone below which such cracks are not seen, multiple tests were conducted at velocities lower than 110 m/s. It was observed that for 20 mm SHI impacts at an average impact velocity of 90 m/s, such cracks were not visible by optical microscopy.

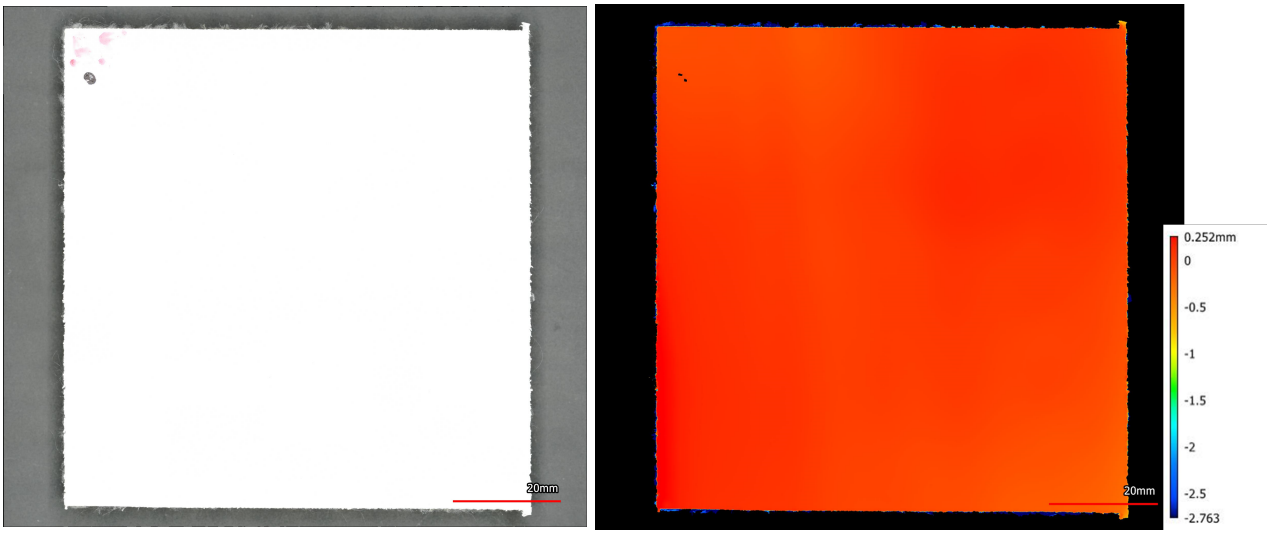

(a) Optical microscope scan of sample **(b)** Height map of sample

Figure 4.6: Optical microscopy pictures of Sample B5 before impact

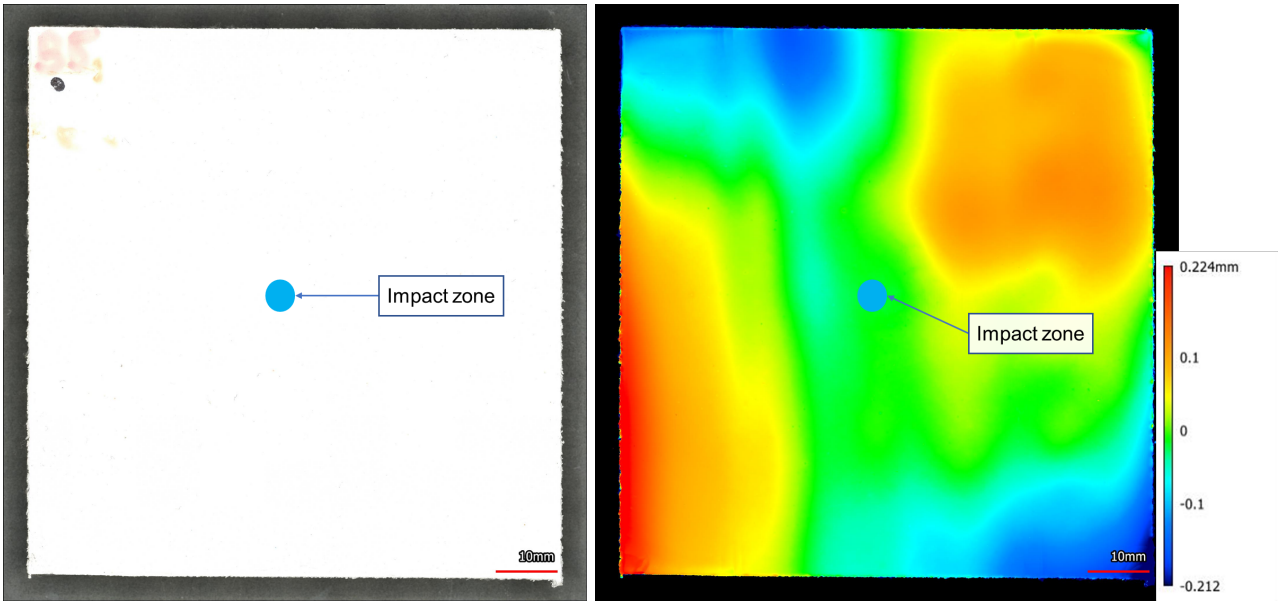

(a) Optical microscope scan of sample **(b)** Height map of sample

Figure 4.7: Optical microscopy pictures of Sample B5 after 10 impacts of 20 mm SHI

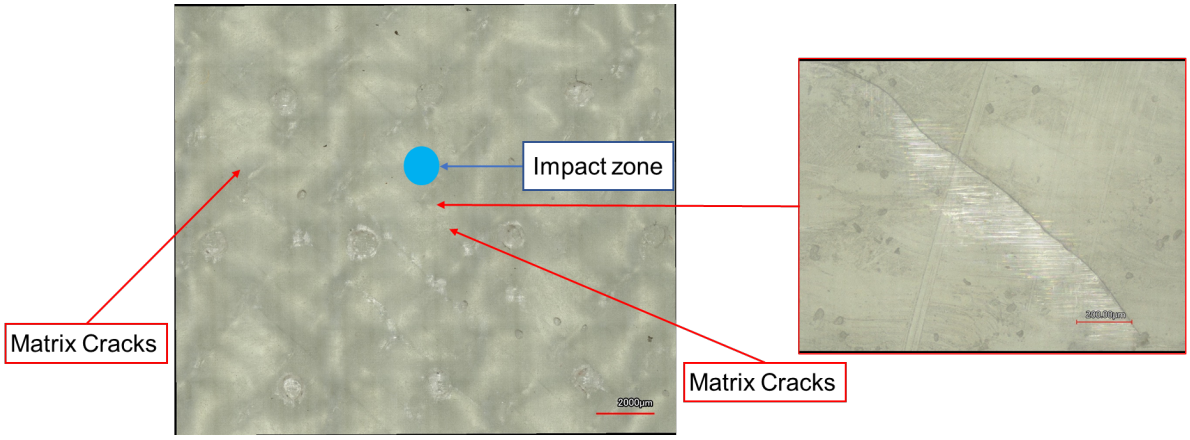

Figure 4.8: Optical microscopy picture of rear of Sample B5 after 10 impacts of 20 mm SHI, showing matrix cracks in -45° direction. A closeup of the matrix crack shows whitening of the matrix around the crack

4.2. Ultrasonic C-scan

Ultrasonic C-scans of the samples were generated to check for delaminations and porosity. Scanning of the samples prior to any impact revealed no signs of voids, impurities or existing defects in the samples. After conducting repeated hail impacts, C-scans were performed again to examine the samples and note any form of delaminations caused by the impacts. The C-scan of the sample D3 (Figure 4.9) impacted 10 times with 15 mm SHI at the highest mean velocity (160 m/s) showed no signs of delaminations or impact damage. Similar observations were noted for sample B5 (Figure 4.10) which was impacted 10 times with a 20 mm SHI at around 112 m/s. C-scans performed for the remaining samples are shown in Appendix E.

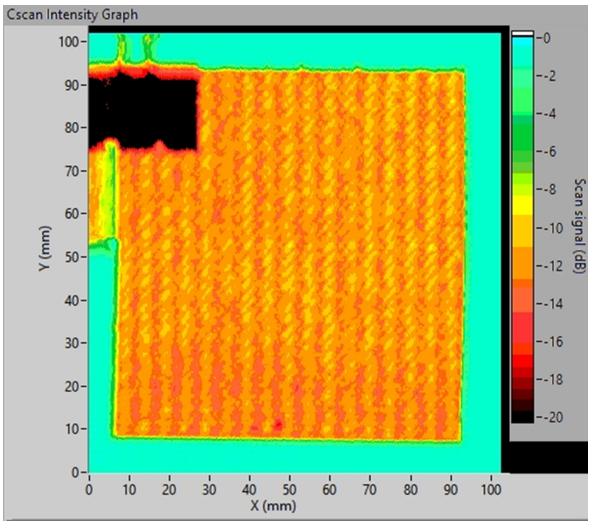

Figure 4.9: C-scan of sample D3 after 10 impacts of 15 mm SHI

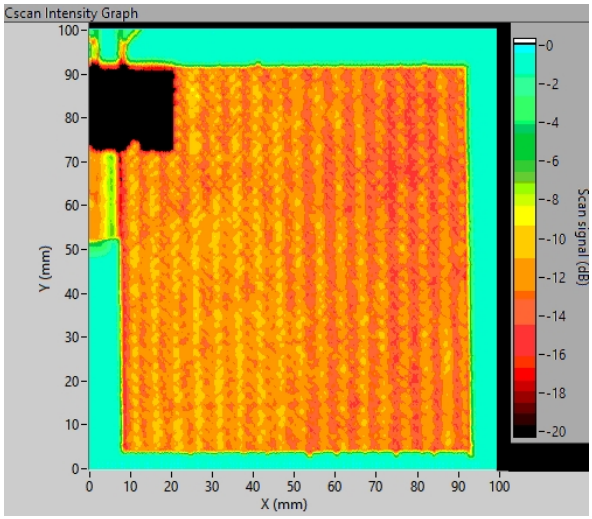

Figure 4.10: C-scan of sample B5 after 10 impacts of 20 mm SHI

4.3. Damage Analysis of Sample Cross-Sections

After conducting the hail impact experiments, the cross-sections of the samples were analyzed with a laser confocal microscope by creating mounts of the sample to get a deeper understanding of the failure mode and to identify the location of failure. Observing the mounts under a coaxial light, transverse matrix cracks were found to be in the lowermost -45° layer. Figure 4.11 shows the cross-section of sample D3, which has been impacted 10 times with a 15 mm SHI (maximum impact velocity of 163 m/s).

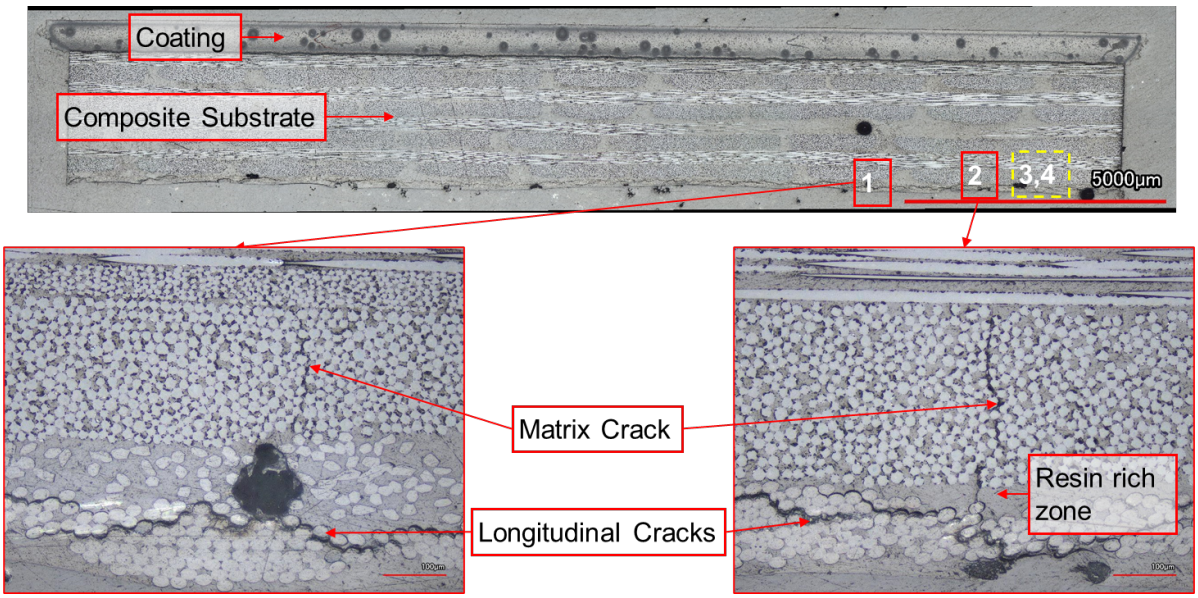

Figure 4.11: Optical microscopy picture of the cross-section of Sample D3 after 10 impacts of 15 mm SHI

Four matrix cracks can be seen in the lowermost -45° layer. The other two cracks are shown in Figure F.5 and Figure F.6. The location of this cross-section is section 3 shown in Figure 3.19. One interesting thing to note here is that the position of these cracks are away from the central point of impact. Similar observations were noted for matrix cracks and delaminations by Eryörük [63]. Looking at a closeup of one of the cracks (left side), we notice the matrix crack appearing in the -45° layer and the resin rich regions. The picture on the right side shows similar matrix cracks in the fibre bundle and the resin rich zone. Longitudinal cracks were seen in both the cases and are detected in the woven fabric layer. This is a feature which has been seen in a lot of samples.

Going back to the observations in section 4.1 about no noticeable damage in the samples impacted at less than 160 m/s, the cross-section of sample C5 showed a singular matrix crack (Figure 4.12). This was something that was not seen earlier while scanning the back of the sample using a laser confocal microscope. This sample was impacted 10 times at an average velocity of 110 m/s followed by 5 impacts at 150 m/s (with the highest impact velocity being 151 m/s). All of these impacts were with 15 mm hailstones. The matrix crack seen in (Figure 4.12) is again in the same location i.e. away from the central point of impact in section 3 of the sample. The singular matrix crack occurs in the resin rich zone between the fibres in the lowermost (-45°) layer and the woven fabric layer. No longitudinal cracks accompanying the matrix crack seen in the previous case is observed here. The picture on the left shows longitudinal cracks in the woven fabric layer but there are no matrix cracks associated with it. To verify if the samples impacted at lower velocities (i.e. 140 m/s and lower) with 15 mm SHI had similar cracks, the rear of the samples were examined using a pinhole light or the coaxial

light of the microscope. No such cracks were seen in the remaining samples. This technique of using a pinhole light/coaxial light was seen to produce something like a highlight or shadow of matrix cracks, if present. This however couldn't be seen on the screen of the microscope system and could be seen only on close scrutinization with the naked eye .

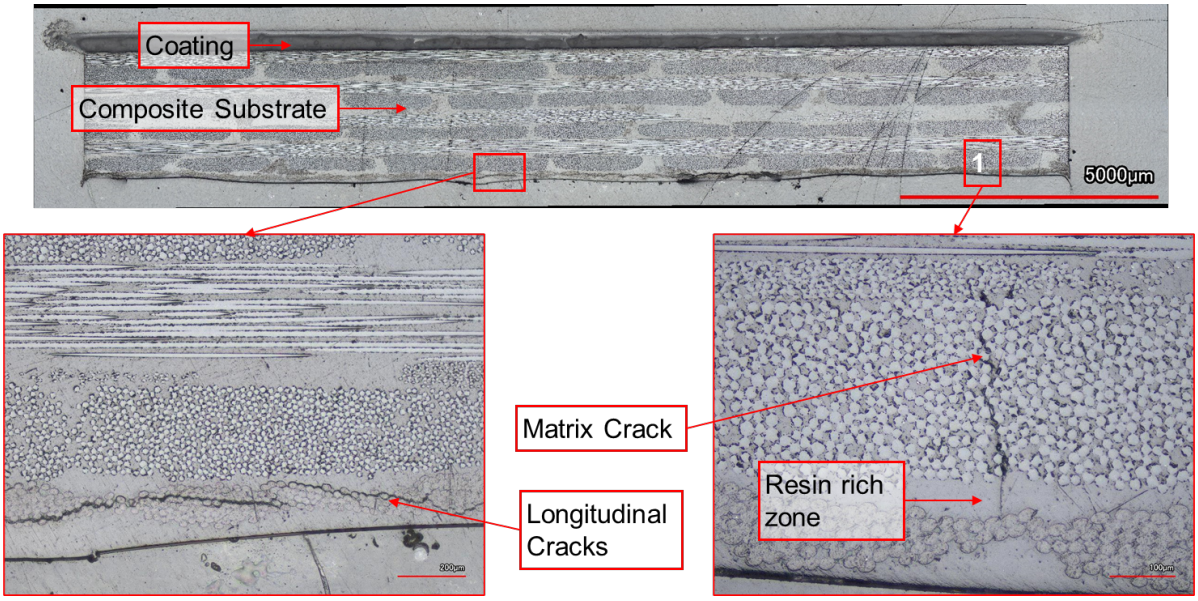

Figure 4.12: Optical microscopy picture of the cross-section of Sample C5 after 15 impacts of 15 mm SHI

Figure 4.13 shows the cross-section of sample B5. This sample was impacted 10 times with a 20 mm SHI with an average impact velocity of 112 m/s (the highest impact velocity being 120 m/s). Six matrix cracks could be seen in the lowermost -45° layer of the cross-section (Remaining cracks shown in Appendix F). Comparing this cross-section with Figure 4.11, we can see that the cracks are higher in number in sample B5. The matrix cracks follow the same pattern, in terms of location.

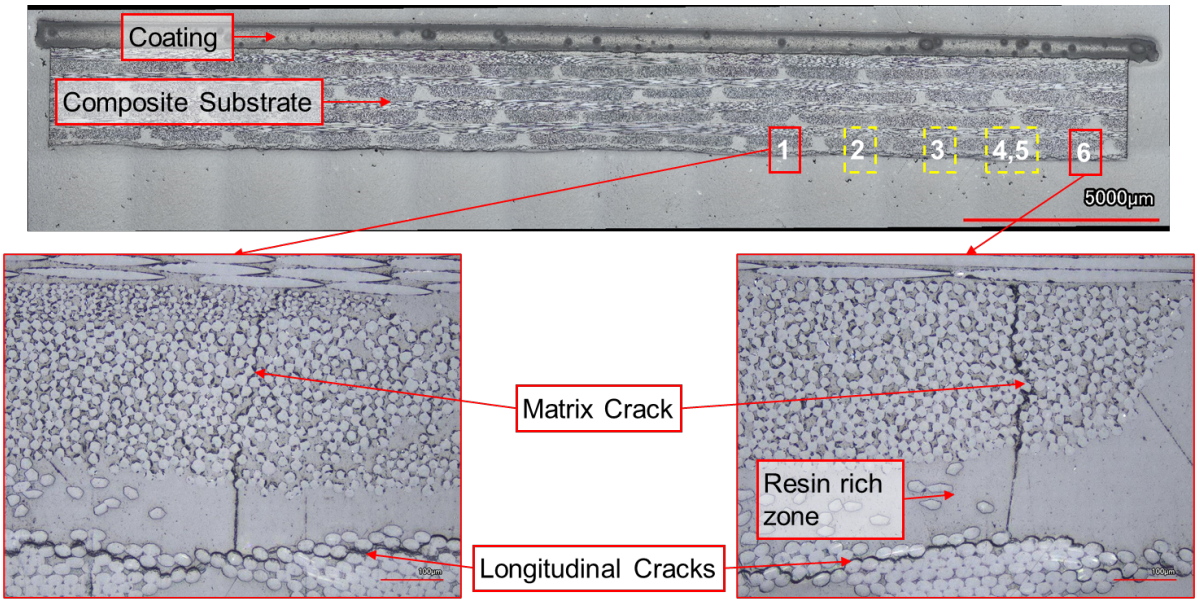

Figure 4.13: Optical microscopy picture of the cross-section of Sample B5 after 10 impacts of 20 mm SHI

Finally, taking the case of sample E4 (impacted 5 times with 20 mm SHI at mean velocities of 100 m/s, with a maximum impact velocity of 104 m/s), four matrix cracks were seen in the lowermost layer. Crack 3 and 4 can be seen in Figure F.9 and Figure F.10. The cracks follow a similar path noted in previous cases, occurring in the resin rich region and the lowermost -45° oriented fibres. The longitudinal cracks seen before were also noticed in this case.

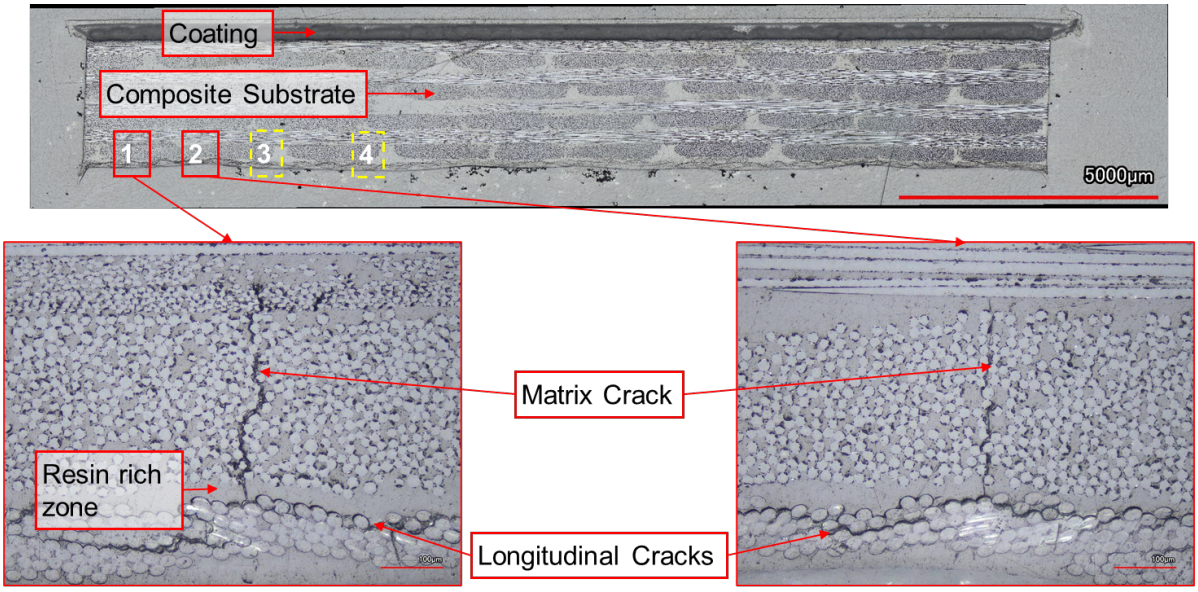

Figure 4.14: Optical microscopy picture of the cross-section of Sample E4 after 5 impacts of 20 mm SHI

Cross-sections of sample C2(15 impacts of 15 mm SHI at highest impact velocity of 124 m/s) and E5 (5 impacts of 20 mm SHI at highest impact velocity of 88 m/s) can be seen in Figure F.1 and Figure F.4, respectively. Other examples are also available in Appendix F.

4.4. Projectile Kinetic Energy and Peak Contact Force

During the experiments, only the hailstone diameter and the impact velocities were varied. The mass measurement of the hailstones and impact velocity measurements were detailed in subsection 3.5.1 and subsection 3.5.2 respectively. These two parameters can be combined together and quantified in the form of kinetic energy, which is given by,

$$KE = \frac{1}{2}mv^2 \tag{4.1}$$

Considering the theoretical density of ice to be 0.92 g/cm^3, the mass of a 15 mm SHI and 20 mm SHI should be 1.63 g and 3.85 g, respectively. However, since the moulds were made oversized (to account for volumetric expansion of water during freezing), the actual mean mass of the hailstones that was recorded is an 1.66 g and 4.53 g for a 15 mm and 20 mm SHI, respectively. By using this mass, the actual diameter of the hailstones are calculated to be 15.28 mm and 21.12 mm.

The average kinetic energy of the 150 m/s impacts of a 15 mm SHI was 18.7 J and the average kinetic energy of the 140 m/s impacts was 15.7 J. As noted by Kim et al.[59] and Macdonald et al.[50], damage occurs on exceeding the failure threshold energy. It is expected that the failure threshold energy (FTE) for a 15 mm SHI for the given sample lies between 15.7 J and 18.7 J and that the threshold velocity lies between 140 m/s and 150 m/s. Similarly, for a 20 mm SHI, the average kinetic energy of impacts at 110 m/s was 27.8 J. The average kinetic energy of 100 m/s impacts was 22.9 J, while the 90 m/s impacts had an average kinetic energy of 18 J. Drawing a similar analogy like before, we can establish that the FTE for a 20 mm SHI lies between 18 J and 22.9 J. Likewise, the threshold velocity for a 20 mm SHI lies between 90 m/s and 100 m/s. From these results, we can clearly see a difference in the threshold velocity for a 15 mm SHI and a 20 mm SHI.

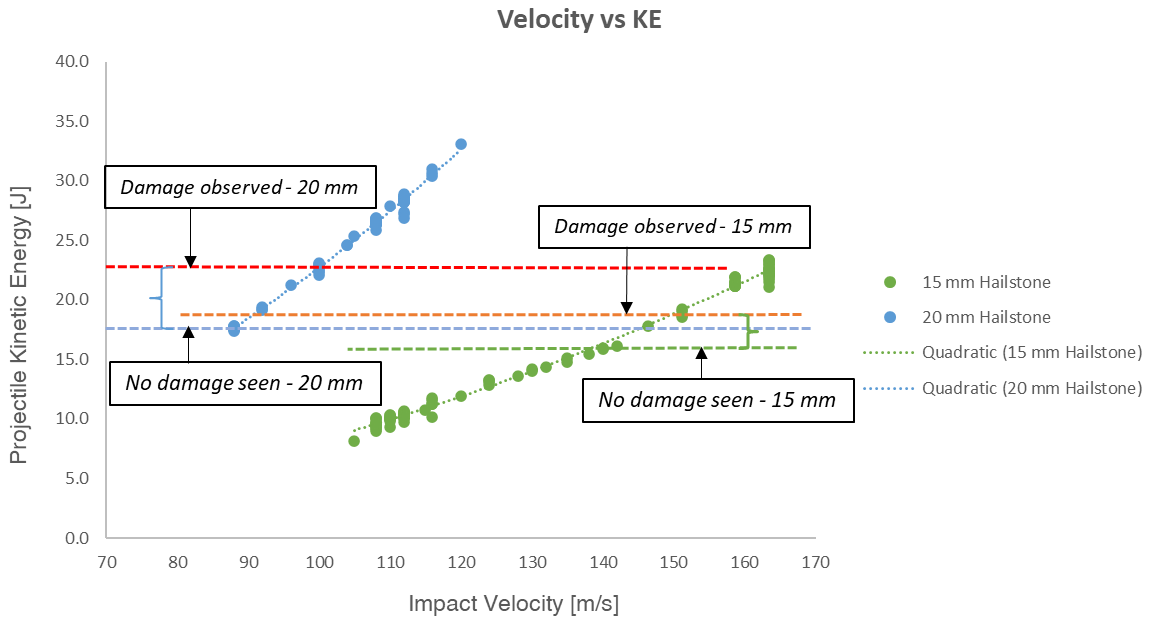

Figure 4.15: Impact velocity vs kinetic energy for 15 mm and 20 mm hailstone. (The blue curly brace on the left indicates the range within which the FTE for a 20 mm SHI lies in. Similarly, the green curly brace on the right indicates the range within which the FTE for a 15 mm SHI lies in.

Plotting the impact velocity of the different hailstones and the kinetic energy calculated

from the mass and velocity, we obtain Figure 4.15. From the expression for kinetic energy (Equation 4.1), we can deduce that the relationship between velocity and kinetic energy will be quadratic, which is also seen in the plot. Looking closely at the plot, we see a small range of kinetic energy between 18 J and 18.7 J, where both the FTE can lie in.

Due to the constraints with the gas cannon and impact chamber setup, the forces couldn't be measured experimentally. However, we can use a theoretical formula and input our experimental variables to get an approximate idea of the forces. In subsection 2.3.1, we had seen Equation 2.1 which provides a theoretical formula to calculate the peak contact forces. The peak forces are calculated from the equation and then plotted against the kinetic energy of the hailstone impacting at the same impact velocities (Figure 4.16). From the plot, a linear trend between peak force and kinetic energy for both the 15 mm hailstone and the 20 mm hailstone is observed. These observations are similar to the observations of Kim et al.[59], where they noted a similar linear relationship.

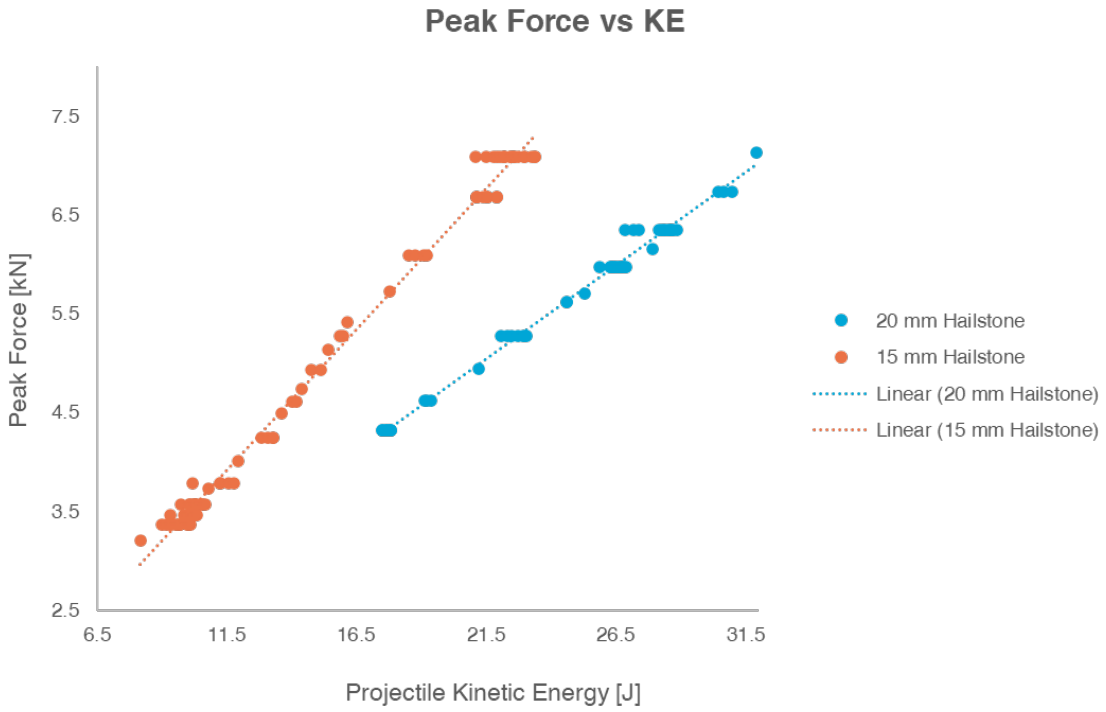

Figure 4.16: Peak contact force vs kinetic energy for 15 mm and 20 mm hailstone

Plotting the impact velocity against the cumulative sum of the contact forces imparted on the sample by the hailstones provides some interesting comparisons (Figure 4.17). It can be seen that cumulative force for five 20 mm hailstone impacts at 110 m/s is almost the same as the cumulative force for ten 15 mm hailstone impacts at the same velocity. This highlights the effect of the radius of the ice sphere on the theoretical contact forces accumulated at similar velocities. However, due to a larger mass of the 20 mm hailstone, the difference in kinetic energy imparted on the sample is larger.

A similar plot can be generated for the impact velocity against the cumulative sum of the energy imparted on the sample (Figure 4.18). Taking the same case as before of a five 20 mm hailstone impacts at 110 m/s and ten 15 mm hailstone impacts at the same velocity, we notice that the difference in accumulated energy is higher by about 30 J, showing the effect

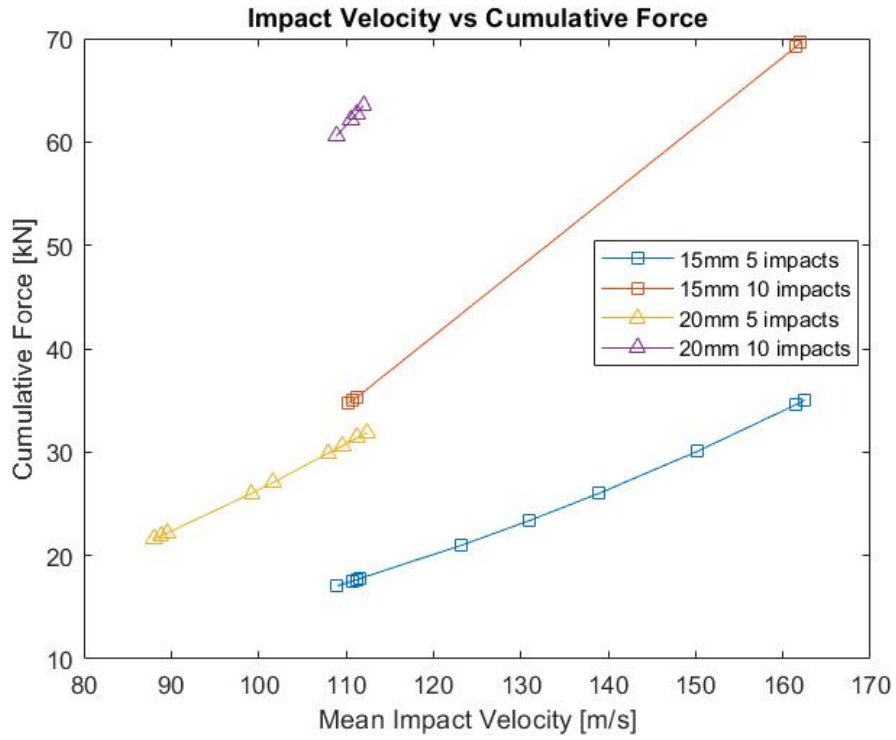

Figure 4.17: Impact velocity vs cumulative force, providing total force imparted on the sample

of increase of mass of hailstones on the energy. This happens even though the number of impacts is comparatively lower.

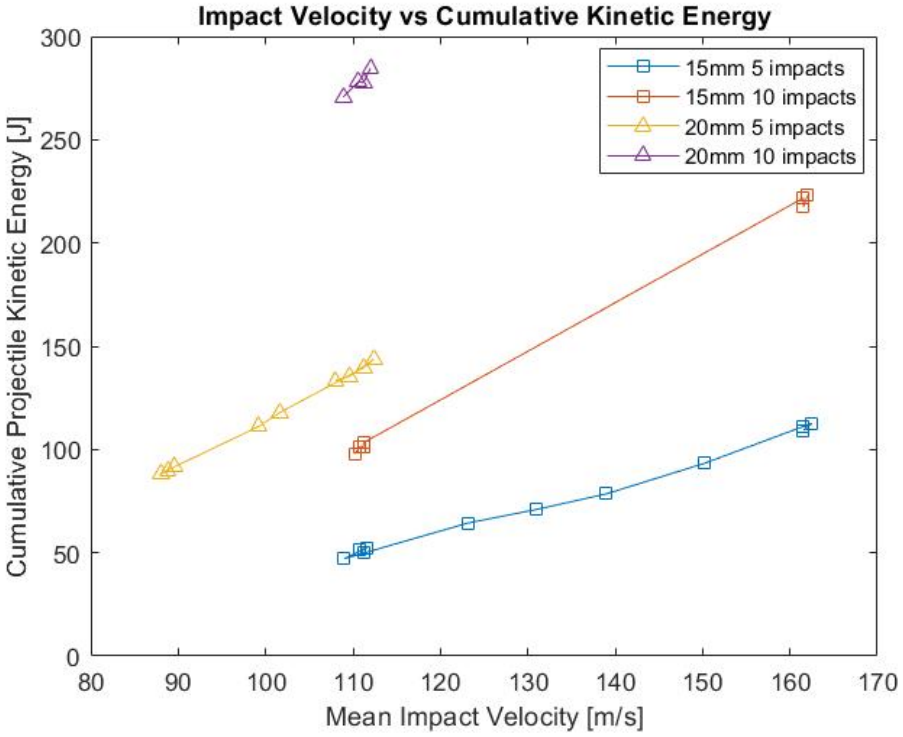

Figure 4.18: Impact velocity vs cumulative kinetic energy, providing total energy imparted on the sample

5
Discussions

5.1. Optical Microscopy

The front and rear of the samples were analyzed through optical microscopy. No visible damage in the coating was reported for any of the samples, suggesting that the coating had good impact resistance for the tested impact parameters. The height map shown in Figure 4.4b shows no change in the surface profile of the coating when impacted by a 15 mm hailstone at the highest impact velocity of 163 m/s (with a mean impact velocity of 162 m/s). Some variability in this observation was noticed for samples impacted at lower velocity (Appendix D). However, for the high impact velocity samples, the surface profile remained the same. It is speculated that this might be caused by the hailstone breaking before impact and thus, hitting spots around the sample.

The height map for a sample impacted by a 20 mm SHI (Figure 4.6b and Figure 4.7b) shows a difference in the surface profile of the coating after the hailstone impacts. This shows clear deformation in the coating and suggests that repeated impact of a 20 mm hailstone imparts sufficient force and energy on the coating to cause such deformation. This is also noted for a 20 mm hailstone impacting at a mean impact velocity of 90 m/s. Conclusion on this deformation being caused by a higher kinetic energy couldn't be drawn, because the case of a 15 mm hailstone at 162 m/s has a higher impact kinetic energy than that of a 20 mm hailstone impacting at 92 m/s. Although it is to be noted here that this doesn't cause any visible coating damage (in the form of cracks and crevices). This is possibly due to the flexible nature of the polyurethane coating. Polyurethane is a highly viscoelastic polymer (subsection 2.1.2) and has high damping properties. This damping could improve the resistance of the coating to impacts and lead to less load transfer through to the GFRP substrate.

Observations of the rear of samples impacted by 15 mm SHI showed faint lines appearing at oblique -45° angles when the samples were impacted at 160 m/s (Figure 4.8). These are interpreted as signs of matrix cracks. At velocities lower than this, no such lines were noted. These oblique lines (for impacts at 160 m/s) were observed to be located slightly away from the impact zone. Similar but more distinct matrix cracks were noted for samples impacted at an impact velocity of 110 m/s with a 20 mm SHI. The highest impact velocity measured for a fully intact 20 mm SHI test was 116 m/s. Whitening of the matrix around the crack was also noted, further affirming the observation that these lines are signs of matrix cracks and indicate that the matrix is under stress. These lines are seen to be more frequent and become more visible with subsequent impacts (observations of cracks after 7 impacts are more discernible than

observations after 4 impacts). This is shown in Figure D.44 and Figure D.45. This suggests that the cracks are growing in size. The number of such cracks observed also seems to increase by a small amount. In contrast, the number of such observed cracks for samples impacted by 15 mm SHI at high mean velocities (160 m/s) remained the same (when observed after 10 impacts).

5.2. Ultrasonic C-Scans

Ultrasonic testing was performed to check for voids or possible delaminations after impacts. The scans performed after the prescribed number of impacts are also shown in Appendix E. All the impacted samples showed no signs of voids or delaminations. As discussed in the previous section, matrix cracks in the -45° direction were seen in some samples, when viewed from the rear. From what was seen in the literature review in subsection 2.3.2, delaminations were identified as the initial observed mode of failure for composites being impacted by hailstones and that delaminations increase with increased contact force. However, Eryörük [63] noticed that in the case of gelcoat GFRP samples impacted by 20 mm SHI, matrix cracking preceded delaminations at lower velocities. This provides context that the contact forces generated on hailstone impact in the current research project are not yet sufficient to cause delaminations. However, it is possible that increasing the impact kinetic energy by increasing the velocity and size of hailstones (and with that, the contact forces) have the potential to develop delaminations. Type II damage and onwards could also be possible at higher projectile kinetic energies (Figure 2.22).

5.3. Cross-Sectional Microscopy

Cross-sections of the impacted samples were observed under high magnification in order to be able to determine the mode of failure. Cross-sectional observations confirmed the presence of transverse matrix cracks. The location of these cracks was found to be in the lowermost -45° layer. The position of these cracks were noted to be away from the central impact zone, similar to the observations in section 4.1. One possible explanation for this was given by O'Brien and Elber [64] that this is caused due to high transverse shear stresses on impact. A higher magnification picture (Figure 4.11) of the cracks show that the transverse matrix cracks occur in the lowermost -45° layer and the resin rich zone between this fibre layer and the woven fabric layer. It is hypothesized that these cracks originate from the rear of the composite (in the case of the left picture, near the void), in a resin rich zone (between the fibre layer and the woven fabric layer) and propagate through the lowermost -45° fibre bundle. The matrix cracks travel through to the lowermost fibre bundle and reach the interface of the -45° and 45° layer.

Comparing the cross-section in Figure 4.13 with Figure 4.11, we can see that the cracks are higher in number in sample B5. In contrast, the cross-section of sample C5 (impacted at a maximum velocity of 151 m/s) shows a single transverse matrix crack in the right corner (Figure 4.12). This goes to show that the impact energy and contact forces imparted by the hailstones, play a large role in the extent of damage seen. The matrix cracks follow the same pattern, in terms of location and direction of crack growth.

Overall, all the samples shown in section 4.3 and Appendix F are consistent in terms of the location of the matrix crack and the layer it is found in. The cracks are present only in the last layer and in none of the other -45° layers. The only case where a difference was noticed was in sample B4 (Figure F.3), where the transverse matrix cracks appear in the resin rich region between the lowermost -45° layer and the 45° layer. Compared to other cross-sections, this

sample had a larger resin rich region between these two fibre layers. It is possible that the cracks extend into this layer because of being drawn towards this resin zone.

When considering bending of the composite panel caused by hail impact, the fibre layers below the neutral axis are in tension. The maximum tension occurs in the last layer (in this case, the -45° layer). This explains why matrix cracks are seen only in the last layer and not the layer closest to the impact. The longitudinal cracks seen in the woven fabric layer present a challenge. A cause of these cracks couldn't be established with the observations of the cross-sections. As was seen in Figure 4.12, some times these transverse matrix cracks are present even though no longitudinal cracks were observed in the cross-sections. It is possible that the depth of these cracks is limited and the cross-sections obtained are unable to show these cracks. The presence of these longitudinal cracks appear random i.e. in some cases with lesser number of impacts at lesser kinetic energy, a large number of longitudinal cracks appear while in some cases with similar parameters, little or no such cracks are seen. The longitudinal cracks in the woven fabric layer are noted to occur near the origin of the transverse matrix cracks. It is expected that this degree of matrix cracks do not reduce the structural performance of the composite. The composite should be able to take most of the loads that it is designed for, inspite of the presence of these matrix cracks. The performance might be affected if these cracks travel towards the coating and create fractures on the coating. This when combined with rain could lead to severe leading edge erosion.

5.4. Kinetic Energy and Peak Contact Force

Macdonald et al.[50] had seen that for each hailstone diameter and sample thickness, there is a threshold velocity below which surface damage is negligible. In our case, the thickness of the coating and substrate is approximately constant, meaning that only the hailstone diameter is a variable here. Going back to the observations of damage discussed in the previous section, it was noted that for a 15 mm SHI, multiple matrix cracks were seen when the SHI was impacted at the PU coated samples at a mean impact velocity of 162 m/s (where the highest noted impact velocity was 163 m/s). A singular matrix crack was observed for the case of 15 impacts (10 impacts at 110 m/s and 5 impacts at 150 m/s) while no noticeable damage was observed in the form of matrix cracks for impacts at or below 140 m/s. Similarly, for a 20 mm SHI, multiple matrix cracks were clearly visible when the hailstones impacted the samples at 110 m/s. Matrix cracks were also seen for impacts of a 20 mm SHI at 100 m/s, whereas no visible matrix cracks were seen in the samples impacted at 90 m/s.

Inspecting the plot in Figure 4.15, it is possible that the FTE for a 15 mm SHI will be slightly higher than the FTE for a 20 mm SHI within this range. However, Kim et al.[59] had found that the FTE for a smaller hailstone is lower than for a larger hailstone because of the impact force being localized to a smaller area compared to a larger area of contact for a larger SHI. Kim et al.[10] also had developed an analytical prediction for the FTE through numerical analysis (Equation 2.8), where β is an empirical constant for a given hailstone and βD depicts the diameter of the ice over which the average shear stress acts. For a larger hailstone, this diameter will be larger and thus, a larger FTE (The prediction shows that FTE is proportional to the square of βD). Therefore, it is likely that the FTE for the 15 mm SHI is lower than the FTE for a 20 mm SHI. Nevertheless, this needs to be verified by measuring the area of contact for different SHI diameters and measuring the force of contact. Impact velocities between the range specified can also be tested to know the exact velocity at which damage is seen.

The manner of experimentally determining the FTE by Kim et al.[59] was to impact the sample at a velocity slightly lower than the expected velocity at which delamination occurred and then, test at a higher velocity until delamination was noted. In our case, the expected velocity for delaminations was unknown and the research had to start from ground zero, to ascertain at what velocity delaminations (or in this case, matrix cracks) occur. Kim et al.[10] also had found through numerical analysis that the FTE is related to the interlaminar shear strain energy at the contact region between the panel and the hailstone. This was used to normalize the FTE and plot it against the ratio of panel thickness and SHI diameter (Figure 2.26). This approach could be particularly useful when testing panels of different thicknesses and subsequently, design a panel to be resistant to hail impact.

The plot between peak force and kinetic energy (Figure 4.16) utilizes the analytical expression for the peak contact force, as shown in Equation 2.1. The experimental values determined are used as the requisite variables in the expressions. Here, the yield stress is determined from Equation 2.2. As highlighted before, this equation takes into account impacts on solid, rigid surfaces [50] and overestimates the actual peak forces. For composites, which have different layers stacked on each other, the actual peak contact forces are expected to be lower. Thus, the forces calculated are exaggerated over what actually occurs. However for this research, a decision was made to use this expression.

The plot between peak contact force and the projectile kinetic energy showed a linear trend. This makes sense when we look at the mathematical expressions for peak force (Equation 2.1) and kinetic energy (Equation 4.1). Both equations are dependent on the impact velocity and the mass of the hailstone. The analytical expression for the peak contact force shows that the force is directly proportional to the impact velocity and directly proportional to the square of the hailstone radius. When we consider the peak forces generated for the same impact velocity, this squared dependence leads to a larger contact force for the 20 mm SHI, compared to the 15 mm SHI. Looking at Figure 4.16, a projectile kinetic energy of about 21.5 J for a 20 mm SHI corresponds to a similar peak force as that generated by the impact of a 15 mm SHI, where it has a kinetic energy of about 15.7 J. This peak force is generated for a 20 mm SHI impacting at 100 m/s and a 15 mm SHI impacting at 150 m/s, showing the effect of SHI radius on the peak force as per the analytical expression.

6

Conclusion

This research project has dealt with conducting hail impact experiments on polyurethane coated glass fibre composites. The effect of hail impact on these PU coated samples were studied in a gas cannon facility at the Delft Aerospace Structures and Materials Laboratory (DASML). The hailstone size and impact velocity to be used for tests were determined based on a thorough literature review. Calibrations were performed to determine the pressures corresponding to specific impact velocities of different hailstone sizes. This allowed repeatability of tests. Damage analysis through non-contact profilometry was conducted to evaluate the surface of the composite and then the cross-sections of the samples were analyzed to get an in-depth picture of the damage and it's location. The answers to the sub-questions that were initially set out in section 2.4 are discussed before answering the main research question.

1. **Which parameters play a key role in understanding the dynamics of hailstone impact?**
   The literature study has suggested that the kinetic energy of an impacting hailstone and the contact forces generated by the hailstone on impact play a major role in the dynamics of a hailstone impact. The literature study revealed that increasing the impact force increases the extent of delamination seen. Both, the failure threshold energy and the contact force are dependent on the same variables i.e. radius of hailstone and impact velocity. Thus, an inter-dependency was seen in literature, where delaminations were triggered on exceeding the failure threshold.

   The other key parameter is the behaviour of ice. Ice has been found to be a complex material, displaying numerous crystal structures. Under compression, the behaviour of ice has been found to be dependent on the strain rate. Since we are dealing with high velocity impacts, the strain rates are such that the material behaves like a semi-brittle material. Research has shown that the behaviour of ice changes when it is reinforced with cotton. This leads to increased compressive strength. This results in the cotton-filled hailstone not shattering completely on impact and thus, being able to concentrate the contact force on a smaller area.

2. **What role does kinetic energy play in damage initiation and progression?**
   It has been seen over the experiments that there exists a failure threshold energy (FTE) for each hailstone size and sample thickness, below which no surface/sub-surface damage is visible. For all the tests conducted, damage initiation occurred on exceeding

the threshold velocity required to cross the FTE for a given hailstone. Without exceeding this threshold, no damage was observed, even after multiple impacts. It has been seen that for a 15 mm hailstone, the FTE lies between 15.7 J and 18.7 J. The velocities at which these energies were obtained was 150 m/s and 160 m/s, respectively. On the other hand, the FTE for a 20 mm hailstone was noted to lie between 18 J and 22.9 J. The impact velocities corresponding to these energy values are 90 m/s and 100 m/s, respectively. This shows the difference in the threshold velocity for each hailstone. It was seen that the the range of this threshold for the two hailstones overlap between 18 J and 18.7 J i.e. it is possible for the exact FTE for a 15 mm hailstone to be higher than the FTE for a 20 mm hailstone. However, it is hypothesized based on observations in literature that the smaller hailstone will have a lower FTE than the larger hailstone and will be more lethal, due to the concentrated area of contact. This however needs to be verified by measuring area of contact, force on impact and the exact velocity at which damage is seen.

3. **What is the principal damage mode in the coating and the composite?**
   It has been observed over the duration of the experiments that the coatings remain largely intact throughout the hail impacts. No visible sign of damage or delamination between coating and substrate was noticed during damage analysis. Deformations in the coating from the height map were seen for 20 mm hailstone impacts. The height maps for 15 mm hailstone impacts even at the highest impact velocity largely remained the same as before any hailstone impact.

   Matrix cracks have been seen in the lowermost -45° layer which is at the rear of the substrate. The cracks appear in the resin rich zone and extend into the this -45° fibre bundle. These cracks appear as faint oblique lines on exceeding the failure threshold energy for the hailstone. The matrix cracks are also found to be located away from the central point of impact of the hailstone. This is explained in literature as being caused due to the high transverse shear stresses on impact.

4. **What is the damage evolution in the coated samples over the course of multiple hailstone impacts?**
   Observations from the optical microscope showed that multiple impacts increased the number of observable matrix cracks in the substrate to a small extent. The damage type observed however was limited to being transverse matrix cracks. These cracks didn't evolve into delaminations or fibre failure. In the case of 15 mm hailstone impacts, they remained faint oblique lines that didn't increase by a substantial number. For 20 mm hailstone impacts, the matrix cracks increased in number (more than the increase in number for 15 mm impacts) and became more visible with multiple impacts. Cross-sectional microscopy revealed that the matrix cracks appeared in the lowermost -45° layer and the resin rich region between this layer and the woven fabric layer. It is hypothesized that the cracks originate in the rear of the composite and traversing between the fibres in resin rich regions towards the lowermost -45° layer. This can also be comprehended when taking into account the bending of the panel by hail impact. The fibre layers at the back are in tension and the maximum tension occurs in the last layer.

Finally, answering the main research question,

"What is the effect of varying hailstone sizes on the damage mode in leading edge polyurethane coatings subjected to hail impact?"

Over the experiments conducted, the damage mode in the polyurethane coated GFRP samples was observed to be matrix cracking for both hailstone sizes, even at the highest impact velocities. These transverse matrix cracks appear in the lowermost -45° layer when the cross-sections are observed. Longitudinal cracks in the woven fabric layer was also seen but no conclusion about the origin of these cracks could be drawn from the evidence obtained in the research. The hypothesis for the formation of the transverse matrix cracks is that these cracks are originate from the rear through the resin rich regions and travel through to the lowermost -45° fibre bundle. Bending of the panels is speculated to be the cause of the cracks appearing in this specific layer (due to tension in this layer). Based on the research by Kim et al.[59], increasing velocity or energy for a given hailstone leads to transition from type I damage (Delamination) to type II damage (backside fibre failure) and so on. It is possible that the energy imparted on the PU coated GFRP samples by both the hailstones is not sufficient to cause delaminations or fibre failure. This might be possible under continuous impacts for longer test times (for example 50 impacts) or by increasing the impact velocity. Another possible explanation for the specific damage evolution seen is that PU coatings are highly flexible and have the potential to dampen the contact forces generated on impact.

Varying the hailstone size causes a difference in the mass of the hailstones to a large degree. It has been seen that for the case of a jump from a 15 mm hailstone to a 20 mm hailstone, the increase in mass was almost three times. This leads to a large increase in the kinetic energy of the hailstones when considering the same impact velocity. This is clear in Figure 4.18, where the difference in accumulated kinetic energy for the case of five 20 mm hailstone impacts and ten 15 mm hailstone impacts at 110 m/s is almost 30 J. This increase in kinetic energy imparts more energy onto the sample on impact and the matrix cracks observed are more noticeable compared to the faint oblique lines for 15 mm impacts. Additionally, hailstone size does affect the number and visibility of the matrix cracks when seen under the optical microscope. For impacts of 20 mm hailstones, the matrix cracks produced were largely visible by a naked eye.

7

Recommendations

The current research project aimed to determine the effect of varying hailstone size on the damage mode in leading edge polyurethane coated composites. One of the research goals was to observe the damage evolution in the coated samples over multiple impacts. It was seen over the course of the thesis that the damage mode observed for the agreed impact parameters produced matrix cracks in the samples when impacted with 15 mm and 20 mm hailstones. As seen over literature, there are further modes of damage that occur in the case of high velocity impacts, which are likely to be more detrimental to the life of the composite. These damage modes could possibly be investigated by increasing the lethality of the impacts. This could be achieved by increasing the impact velocity or increasing the size of the hailstone used. Increasing velocity would potentially make the velocity measurements difficult, as the accuracy with which these measurements could be performed decrease. Adding dye while manufacturing the hailstones could likely aid in velocity measurement. A larger diameter hailstone would be a cost-effective solution. However, due to the limitation of the gas cannon and the compressed air pressure available, this couldn't be exceeded beyond what was performed in the thesis. Modifications to the setup, like fabricating a barrel with a larger diameter (within the constraints of the gas cannon frame) could make such tests viable. Experimental measurement of the impact force could also aid in further understanding the key factors affecting damage initiation and growth in the composite. Force measurement techniques like a force transducer or a load cell could be looked at.

The results obtained from this thesis can also be further enhanced by conducting studies that directly or indirectly incorporate hail impact tests. One interesting thing to look at could be the effect of UV exposure to the hail impact resistance of the coating. This is useful in the real-life context, as wind turbine blades are exposed to intense sunlight and there has been known research on the degradation of the properties of thermoplastic coatings with long term exposure to UV light. Studying the effect of blade curvature and glancing impacts could also be interesting and provide some knowledge base in experimental testing of such panels. In case of samples which have delaminations but no coating damage, hail impact testing could be followed by rain erosion testing to see if the rain erosion performance of the coating gets affected by the presence of matrix cracks and delaminations in the substrate. This could be potentially useful to the wind turbine manufacturers as hail is a site-specific issue and does not occur throughout the year.

Further modifications to the setup in future could be used to conduct hail impact experiments at higher impact frequencies to allow lower relaxation time in the viscoelastic coatings. The

possibility of a temperature controlled chamber will allow testing of smaller hail projectiles which cannot be tested with the current setup. The temperature control could also be achieved with the help of a breech which keeps the projectiles cold between loading and firing.

References

[1] UNFCCC, “The Paris Agreement | UNFCCC.” [Online]. Available: https://unfccc.int/process-and-meetings/the-paris-agreement/the-paris-agreement

[2] WindEurope, “Wind energy in Europe: Outlook to 2023,” Oct. 2019, section: Reports. [Online]. Available: https://windeurope.org/about-wind/reports/wind-energy-in-europe-outlook-to-2023/

[3] NationalGeographic, “Wind Power,” Oct. 2009, section: Environment. [Online]. Available: https://www.nationalgeographic.com/environment/article/wind-power

[4] R. Wiser, J. Rand, J. Seel, P. Beiter, E. Baker, E. Lantz, and P. Gilman, “Expert elicitation survey predicts 37% to 49% declines in wind energy costs by 2050,” *Nature Energy*, vol. 6, no. 5, pp. 555–565, May 2021. [Online]. Available: https://www.nature.com/articles/s41560-021-00810-z

[5] US Department of Energy, “Map: Projected Growth of the Wind Industry From Now Until 2050.” [Online]. Available: https://www.energy.gov/maps/map-projected-growth-wind-industry-now-until-2050

[6] GWEC, “Global Wind Report 2021,” Mar. 2021. [Online]. Available: https://gwec.net/global-wind-report-2021/

[7] M. H. Keegan, D. H. Nash, and M. M. Stack, “On erosion issues associated with the leading edge of wind turbine blades,” *Journal of Physics D: Applied Physics*, vol. 46, no. 38, p. 383001, Sep. 2013. [Online]. Available: https://iopscience.iop.org/article/10.1088/0022-3727/46/38/383001

[8] Office of Energy Efficiency & Renewable Energy, “Wind Turbines: the Bigger, the Better.” [Online]. Available: https://www.energy.gov/eere/articles/wind-turbines-bigger-better

[9] M. Froese, “3M to launch Wind Protection Tape 2.0 at WindEnergy Hamburg,” *Wind power engineering*, vol. 9, 2016.

[10] H. Kim and K. T. Kedward, “Modeling Hail Ice Impacts and Predicting Impact Damage Initiation in Composite Structures,” *AIAA Journal*, vol. 38, no. 7, pp. 1278–1288, Jul. 2000, publisher: American Institute of Aeronautics and Astronautics. [Online]. Available: https://arc.aiaa.org/doi/10.2514/2.1099

[11] D. Windtechnik, “Eradicating blade damage,” Nov. 2014. [Online]. Available: https://www.sunwindenergy.com/wind-energy/eradicating-blade-damage

[12] L. Rempel, “Rotor blade leading edge erosion-real life experiences,” *Wind Systems Magazine*, p. 3, 2012. [Online]. Available: https://www.windsystemsmag.com/wp-content/uploads/pdfs/Articles/2012_October/1012_BladeFeature.pdf

[13] L. Mishnaevsky, “Repair of wind turbine blades: Review of methods and related computational mechanics problems,” *Renewable Energy*, vol. 140, pp. 828–839, Sep. 2019. [Online]. Available: https://linkinghub.elsevier.com/retrieve/pii/S0960148119304252

[14] E. Sagol, M. Reggio, and A. Ilinca, “Issues concerning roughness on wind turbine blades,” *Renewable and Sustainable Energy Reviews*, vol. 23, pp. 514–525, Jul. 2013. [Online]. Available: https://www.sciencedirect.com/science/article/pii/S1364032113001366

[15] J. I. Bech, C. B. Hasager, and C. Bak, “Extending the life of wind turbine blade leading edges by reducing the tip speed during extreme precipitation events,” *Wind Energy Science*, vol. 3, no. 2, pp. 729–748, Oct. 2018, publisher: Copernicus GmbH. [Online]. Available: https://wes.copernicus.org/articles/3/729/2018/

[16] L. Mishnaevsky, K. Branner, H. N. Petersen, J. Beauson, M. McGugan, and B. F. Sørensen, “Materials for Wind Turbine Blades: An Overview,” *Materials*, vol. 10, no. 11, p. 1285, Nov. 2017, number: 11 Publisher: Multidisciplinary Digital Publishing Institute. [Online]. Available: https://www.mdpi.com/1996-1944/10/11/1285

[17] A. Europe, “Wind Energy | Airtech Europe.” [Online]. Available: https://www.airtech.lu/wind-energy

[18] H. Haberkern, “Tailor-made reinforcements,” *Reinforced Plastics*, vol. 50, no. 4, pp. 28–33, Apr. 2006. [Online]. Available: https://www.sciencedirect.com/science/article/pii/S0034361706709742

[19] A. N. Mengal, S. Karuppanan, and A. A. Wahab, “Basalt Carbon Hybrid Composite for Wind Turbine Rotor Blades: A Short Review,” *Advanced Materials Research*, vol. 970, pp. 67–73, 2014, conference Name: Science and Engineering of Materials ISBN: 9783038350927 Publisher: Trans Tech Publications Ltd. [Online]. Available: https://www.scientific.net/AMR.970.67

[20] A. S. Verma, Z. Jiang, M. Caboni, H. Verhoef, H. van der Mijle Meijer, S. G. Castro, and J. J. Teuwen, “A probabilistic rainfall model to estimate the leading-edge lifetime of wind turbine blade coating system,” *Renewable Energy*, vol. 178, pp. 1435–1455, Nov. 2021. [Online]. Available: https://linkinghub.elsevier.com/retrieve/pii/S0960148121009885

[21] E. Cortés, F. Sánchez, A. O’Carroll, B. Madramany, M. Hardiman, and T. M. Young, “On the Material Characterisation of Wind Turbine Blade Coatings: The Effect of Interphase Coating–Laminate Adhesion on Rain Erosion Performance,” *Materials*, vol. 10, no. 10, Oct. 2017. [Online]. Available: https://www.mdpi.com/1996-1944/10/10/1146

[22] A. S. Verma, S. G. P. Castro, Z. Jiang, and J. J. E. Teuwen, “Numerical investigation of rain droplet impact on offshore wind turbine blades under different rainfall conditions: A parametric study,” *Composite Structures*, vol. 241, p. 112096, Jun. 2020. [Online]. Available: https://www.sciencedirect.com/science/article/pii/S0263822319329794

[23] E. Cortés, F. Sánchez, A. O’Carroll, B. Madramany, M. Hardiman, and T. M. Young, “On the Material Characterisation of Wind Turbine Blade Coatings: The Effect of Interphase Coating–Laminate Adhesion on Rain Erosion Performance,” *Materials*, vol. 10, no. 10, p. 1146, Oct. 2017, number: 10 Publisher: Multidisciplinary Digital Publishing Institute. [Online]. Available: https://www.mdpi.com/1996-1944/10/10/1146

[24] J. Seyyed Monfared Zanjani, I. Baran, and R. Akkerman, “Combatting rain erosion of offshore wind turbine blades by co-bonded thermoplastic-thermoset hybrid composites,” *IOP Conference Series: Materials Science and Engineering*, vol. 942, p. 012024, Oct. 2020. [Online]. Available: https://iopscience.iop.org/article/10.1088/1757-899X/942/1/012024

[25] 3M, “3M Wind Blade Protection Coating W4600 - Technical data sheet and application guide.” [Online]. Available: https://multimedia.3m.com/mws/media/978868O/3m-wind-blade-coating-w4600-app-guide-and-technical.data.pdf

[26] LM Wind Power, “The ProBlade Ultra- a superior leading edge protection solution! | LM Wind Power.” [Online]. Available: https://www.lmwindpower.com/en/services/stories/the-problade-ultra

[27] I. Yilgör, E. Yilgör, and G. L. Wilkes, “Critical parameters in designing segmented polyurethanes and their effect on morphology and properties: A comprehensive review,” *Polymer*, vol. 58, pp. A1–A36, Feb. 2015. [Online]. Available: https://www.sciencedirect.com/science/article/pii/S0032386114011136

[28] N. Sigamani, “Characterization of Polyurethane at Multiple Scales for Erosion Mechanisms Under Sand Particle Impact,” Master’s thesis, Texas A&M University, Jul. 2010, accepted: 2010-07-15T00:17:23Z. [Online]. Available: https://tdl-ir.tdl.org/handle/1969.1/ETD-TAMU-2010-05-8008

[29] L. Mishnaevsky and J. Sütterlin, “Micromechanical model of surface erosion of polyurethane coatings on wind turbine blades,” *Polymer Degradation and Stability*, vol. 166, pp. 283–289, Aug. 2019. [Online]. Available: https://linkinghub.elsevier.com/retrieve/pii/S0141391019302125

[30] J. Kolarik, “Simultaneous prediction of the modulus and yield strength of binary polymer blends,” *Polymer Engineering and Science*, vol. 36, no. 20, pp. 2518–2524, 1996.

[31] L. E. Govaert, E. L. J. C. J. D’Hooghe, and A. A. J. M. Peijs, “A micromechanical approach to the viscoelasticity of unidirectional hybrid composites,” *Composites*, vol. 22, no. 2, pp. 113–119, Mar. 1991. [Online]. Available: https://www.sciencedirect.com/science/article/pii/0010436191906698

[32] L. Mishnaevsky Jr, “Toolbox for optimizing anti□erosion protective coatings of wind turbine blades: Overview of mechanisms and technical solutions,” *Wind Energy*, vol. 22, Nov. 2019.

[33] M. LeGault, “Wind blades: Progress and challenges,” Oct. 2013. [Online]. Available: https://www.compositesworld.com/articles/wind-blades-progress-and-challenges

[34] 3M, “3M Wind Energy Solutions,” archive Location: US Layout: Luxury. [Online]. Available: https://www.3m.com/3M/en_US/power-generation-us/solutions/wind-energy/

[35] W. D. Weigel, “Advanced Rotor Blade Erosion Protection System,” Kaman Aerospace Corporation, Bloomfield, Tech. Rep., 1996.

[36] M. D. Haag, “Advances in leading edge protection of wind turbine blades,” Vienna, Austria, Feb. 2013.

[37] LM Wind Power, “On the leading edge: Innovative solutions to reduce rain erosion | LM Wind Power.” [Online]. Available: https://www.lmwindpower.com/en/stories-and-press/stories/innovation/on-the-leading-edge

[38] M. M. Shokrieh and A. Bayat, “Effects of Ultraviolet Radiation on Mechanical Properties of Glass/Polyester Composites,” *Journal of Composite Materials*, vol. 41, no. 20, pp. 2443–2455, Oct. 2007, publisher: SAGE Publications Ltd STM. [Online]. Available: https://doi.org/10.1177/0021998307075441

[39] Gurit, “Guide to Composites,” 2013. [Online]. Available: https://www.gurit.com/-/media/Gurit/Datasheets/guide-to-composites.pdf

[40] P. Field, W. Hand, G. Cappelluti, A. McMillan, A. Foreman, D. Stubbs, and M. Willows, “Hail threat standardisation,” *Research project EASA*, vol. 5, 2008.

[41] M. H. Keegan, D. Nash, and M. Stack, “Wind Turbine Blade Leading Edge Erosion : An Investigation of Rain Droplet and Hailstone Impact Induced Damage Mechanisms,” phd, University of Strathclyde, Glasgow, 2014. [Online]. Available: https://strathprints.strath.ac.uk/58904/

[42] ERZ, “The centre of a large hailstone with alternate layers of opaque and transparent ice.” May 2008. [Online]. Available: https://commons.wikimedia.org/wiki/File:Hagelkorn_mit_Anlagerungsschichten.jpg

[43] H. Macdonald, D. Infield, D. H. Nash, and M. M. Stack, “Mapping hail meteorological observations for prediction of erosion in wind turbines,” *Wind Energy*, vol. 19, no. 4, pp. 777–784, 2016, _eprint: https://onlinelibrary.wiley.com/doi/pdf/10.1002/we.1854. [Online]. Available: https://onlinelibrary.wiley.com/doi/abs/10.1002/we.1854

[44] T. Pucik, “Hailstorms of 2021 | European Severe Storms Laboratory.” [Online]. Available: https://www.essl.org/cms/hailstorms-of-2021/

[45] E. M. Schulson, “The Brittle Failure of Ice under Compression,” *The Journal of Physical Chemistry B*, vol. 101, no. 32, pp. 6254–6258, Aug. 1997. [Online]. Available: https://pubs.acs.org/doi/10.1021/jp9632192

[46] K. S. Carney, D. J. Benson, P. DuBois, and R. Lee, “A phenomenological high strain rate model with failure for ice,” *International Journal of Solids and Structures*, vol. 43, no. 25, pp. 7820–7839, Dec. 2006. [Online]. Available: https://www.sciencedirect.com/science/article/pii/S0020768306001119

[47] I. V. Roisman and C. Tropea, “Impact of a crushing ice particle onto a dry solid wall,” *Proceedings of the Royal Society A: Mathematical, Physical and Engineering Sciences*, vol. 471, no. 2183, p. 20150525, Nov. 2015. [Online]. Available: https://royalsocietypublishing.org/doi/10.1098/rspa.2015.0525

[48] C. V. Raman., “On Some Applications of Hertz’s Theory of Impact,” *Physical Review*, vol. 15, no. 4, pp. 277–284, Apr. 1920, publisher: American Physical Society. [Online]. Available: https://link.aps.org/doi/10.1103/PhysRev.15.277

[49] J. D. Tippmann, H. Kim, and J. D. Rhymer, “Experimentally validated strain rate dependent material model for spherical ice impact simulation,” *International Journal of Impact Engineering*, vol. 57, pp. 43–54, Jul. 2013. [Online]. Available: https://www.sciencedirect.com/science/article/pii/S0734743X13000201

[50] H. Macdonald, D. Nash, and M. M. Stack, “Repeated impact of simulated hail ice on glass fibre composite materials,” *Wear*, vol. 432-433, p. 102926, Aug. 2019. [Online]. Available: https://linkinghub.elsevier.com/retrieve/pii/S0043164818310172

[51] A. Dennis, “Weather Modification by Cloud Seeding,” *International Geophysics Series*, vol. 24, Jan. 1980. [Online]. Available: https://digitalcommons.usu.edu/water_rep/670

[52] A. J. Heymsfield, I. M. Giammanco, and R. Wright, “Terminal velocities and kinetic energies of natural hailstones,” *Geophysical Research Letters*, vol. 41, no. 23, pp. 8666–8672, 2014, _eprint: https://onlinelibrary.wiley.com/doi/pdf/10.1002/2014GL062324. [Online]. Available: https://onlinelibrary.wiley.com/doi/abs/10.1002/2014GL062324

[53] H. Kim, J. D. Nightingale, and H. Park, “Impact damage resistance of composite panels impacted by cotton-filled and unfilled ice,” 2007.

[54] J. Sun, N. Lam, L. Zhang, D. Ruan, and E. Gad, “Contact forces generated by hailstone impact,” *International Journal of Impact Engineering*, vol. 84, pp. 145–158, Oct. 2015. [Online]. Available: https://www.sciencedirect.com/science/article/pii/S0734743X1500113X

[55] H. Kim and K. T. Kedward, “Modeling Hail Ice Impacts and Predicting Impact Damage Initiation in Composite Structures,” *AIAA Journal*, vol. 38, no. 7, pp. 1278–1288, Jul. 2000. [Online]. Available: https://arc.aiaa.org/doi/10.2514/2.1099

[56] G. a. O. Davies and R. Olsson, “Impact on composite structures,” *The Aeronautical Journal*, vol. 108, no. 1089, pp. 541–563, Nov. 2004, publisher: Cambridge University Press. [Online]. Available: https://www.cambridge.org/core/journals/aeronautical-journal/article/abs/impact-on-composite-structures/6EEE5B2A54C1C0025EBAF47DD97BF27A

[57] M. Mahinfalah and R. A. Skordahl, “The effects of hail damage on the fatigue strength of a graphite/epoxy composite laminate,” *Composite Structures*, vol. 42, no. 2, pp. 101–106, Jun. 1998. [Online]. Available: https://www.sciencedirect.com/science/article/pii/S0263822398000567

[58] W. Jackson and C. Poe, “The Use of Impact Force as a Scale Parameter for the Impact Response of Composite Laminates,” *Journal of Composites Technology and Research*, vol. 15, no. 4, p. 282, 1993. [Online]. Available: http://www.astm.org/doiLink.cgi?CTR10380J

[59] H. Kim, D. A. Welch, and K. T. Kedward, “Experimental investigation of high velocity ice impacts on woven carbon/epoxy composite panels,” *Composites Part A: Applied Science and Manufacturing*, vol. 34, no. 1, pp. 25–41, Jan. 2003. [Online]. Available: https://www.sciencedirect.com/science/article/pii/S1359835X02002580

[60] E. M. Schulson, “The brittle compressive fracture of ice,” *Acta Metallurgica et Materialia*, vol. 38, no. 10, pp. 1963–1976, Oct. 1990. [Online]. Available: https://www.sciencedirect.com/science/article/pii/0956715190903084

[61] F07 Committee, “Standard Test Method for Hail Impact Resistance of Aerospace Transparent Enclosures,” ASTM International, Tech. Rep. [Online]. Available: http://www.astm.org/cgi-bin/resolver.cgi?F320-21

[62] M. Alonso Diaz, “Leading Edge Erosion. Effect of droplet impact frequencies and dry intervals on incubation times of polyurethane coatings,” Master’s thesis, TU Delft, 2021. [Online]. Available: https://repository.tudelft.nl/islandora/object/uuid%3Ae085cfb7-1fe1-47e9-b0f4-5d3bf4487d6a

[63] H. Eryörük, “Effects of gelcoat thickness on damage resistance of leading edge gelcoated glass fibre composite subjected to hailstone impact,” Master’s thesis, TU Delft, 2021. [Online]. Available: https://repository.tudelft.nl/islandora/object/uuid%3Abec72336-20ff-4409-8fd3-4b61072b0bd6

[64] T. O'Brien and W. Elber, "Delamination and fatigue of composite materials: a review," *AGARD, Debonding/Delamination of Composites 11 p(SEE N 93-21507 07-24)*, 1992.

A

Design Chart for Peak Force Estimation

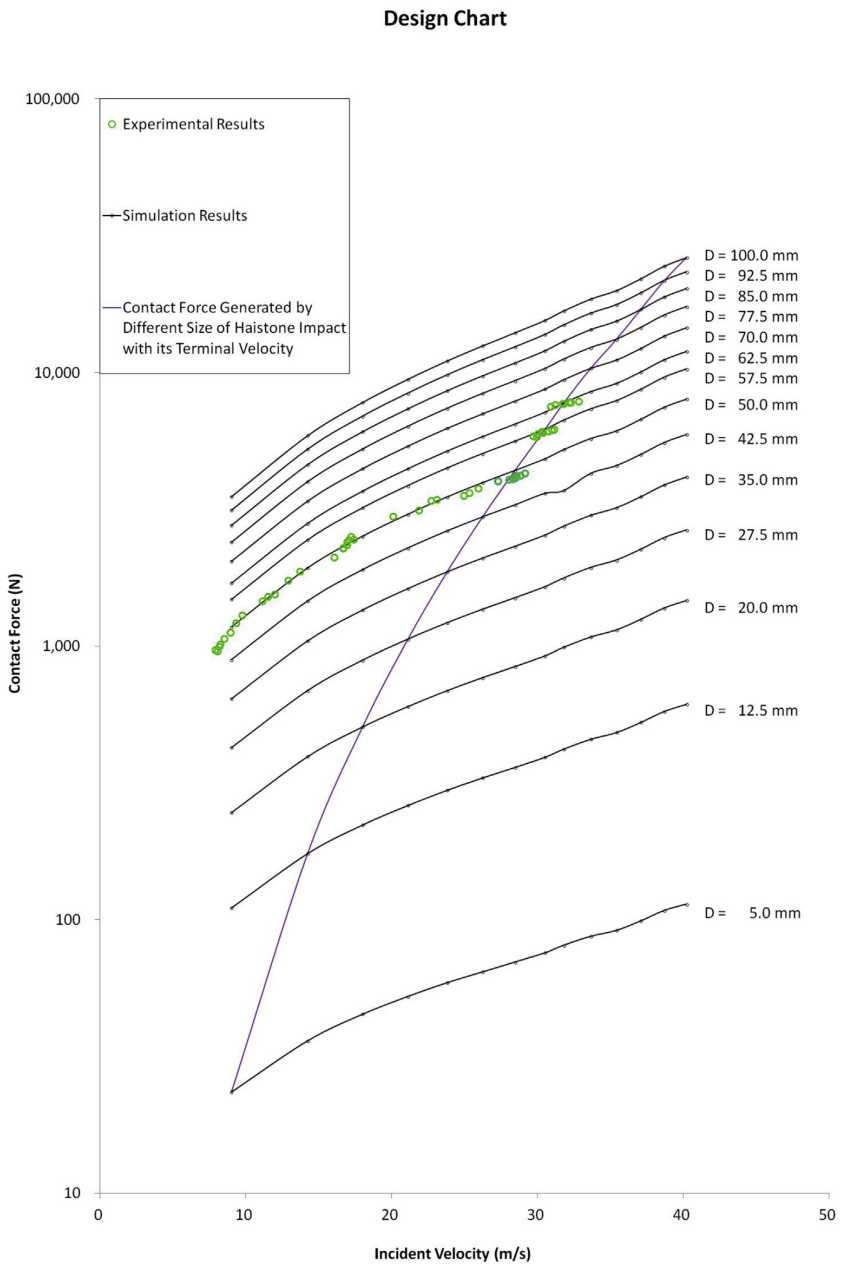

Figure A.1: Design chart to estimate peak forces for SHI ranging from 5 mm to 100 mm diameter [54]

B

Pressure-velocity calibration

15 mm		
Test Case	**Pressure [bar]**	**Velocity [m/s]**
1	1	0
2	2.05	28
3	2.06	29
4	3.01	62
5	3.04	64
6	3.08	64
7	3.95	93
8	4.05	96
9	4.1	96
10	4.19	99
11	4.63	108
12	4.66	108
13	4.69	108
14	4.74	112
15	4.83	115
16	4.87	115
17	4.98	115
18	5.07	115
19	5.1	115
20	5.93	121
21	6.08	125
22	6.17	126
23	6.97	132
24	7.13	135
25	7.99	144
26	8.13	144
27	8.52	152
28	8.94	159
29	9.04	159
30	9.24	159
31	9.32	163
32	9.52	163
33	9.68	163

Table B.1: Pressure-velocity calibration for 15 mm hailstone

20 mm		
Test Case	**Pressure [bar]**	**Velocity [m/s]**
1	1	0
2	2.17	23
3	2.44	30
4	3.07	51
5	3.22	54
6	3.23	54
7	4.05	69
8	4.17	72
9	4.38	75
10	4.66	78
11	5.16	84
12	5.35	87
13	5.51	90
14	6.06	94
15	6.19	97
16	6.23	97
17	6.51	101
18	7.11	108
19	7.13	108
20	7.18	110
21	7.26	112
22	7.56	116
23	7.96	120
24	8.1	124
25	8.28	128
26	8.53	132
27	9.04	136
28	9.14	136
29	9.32	138
30	9.48	140

Table B.2: Pressure-velocity calibration for 20 mm hailstone

C

Hailstone Mass Measurement

Mass with ice [g]	Mass without ice [g]	Mass of Ice [g]	Sample name (Impact number)
11.91	10.19	1.72	C2 (1st)
11.47	9.87	1.6	C2 (2nd)
11.67	9.94	1.73	C2 (3rd)
11.62	9.98	1.64	C2 (4th)
11.5	9.9	1.6	C2 (5th)
11.87	10.17	1.7	C3 (1st)
11.77	10.13	1.64	C3 (2nd)
11.92	10.23	1.69	C3 (3rd)
11.87	10.16	1.71	C3 (4th)
11.76	10.06	1.7	C3 (5th)
11.78	10.11	1.67	C4 (1st)
11.85	10.22	1.63	C4 (2nd)
11.88	10.17	1.71	C4 (3rd)
12.02	10.42	1.6	C4 (4th)
11.86	10.18	1.68	C4 (5th)
11.81	10.33	1.48	C5 (1st)
11.76	10.15	1.61	C5 (2nd)
11.48	9.94	1.54	C5 (3rd)
11.82	10.19	1.63	C5 (4th)
12.12	10.46	1.66	C5 (5th)

Table C.1: Mass measurement for 15 mm hailstone

Mass with ice [g]	Mass without ice [g]	Mass of Ice [g]	Sample name (Impact number)
17.78	13.18	4.6	B3 (1st)
17.89	13.27	4.62	B3 (2nd)
17.93	13.33	4.6	B3 (3rd)
17.86	13.29	4.57	B3 (4th)
17.65	13.24	4.41	B3 (5th)
17.87	13.21	4.66	B4 (1st)
17.97	13.35	4.62	B4 (2nd)
17.85	13.31	4.54	B4 (3rd)
17.82	13.25	4.57	B4 (4th)
17.96	13.36	4.6	B4 (5th)
17.79	13.31	4.48	B5 (4th)
17.81	13.25	4.56	B5 (2nd)
17.96	13.31	4.65	B5 (3rd)
17.97	13.36	4.61	B4 (6th)
17.96	13.32	4.64	B5 (5th)
17.96	13.32	4.64	C1 (1st)
17.69	13.15	4.54	C1 (2nd)
17.79	13.19	4.6	C1 (3rd)
18.01	13.35	4.66	C1 (4th)
17.92	13.35	4.57	C1 (5th)

Table C.2: Mass measurement for 20 mm hailstone

D

Optical Microscopy

Front side of samples impacted with 15 mm SHI

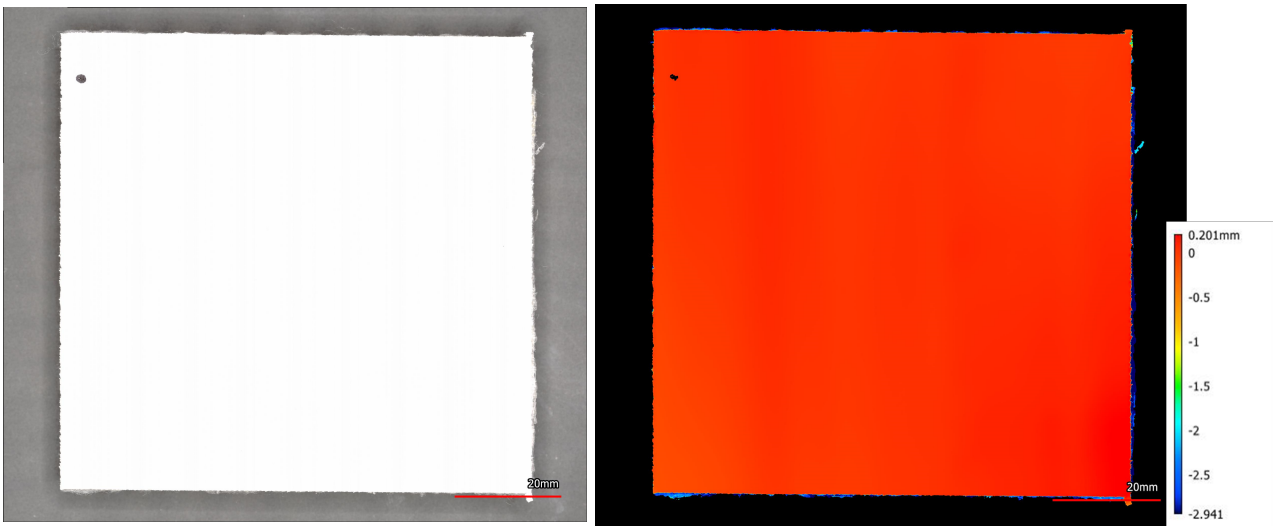

(a) Optical microscope scan of sample

(b) Height map of sample

Figure D.1: Optical microscopy pictures of Sample C2 before impact

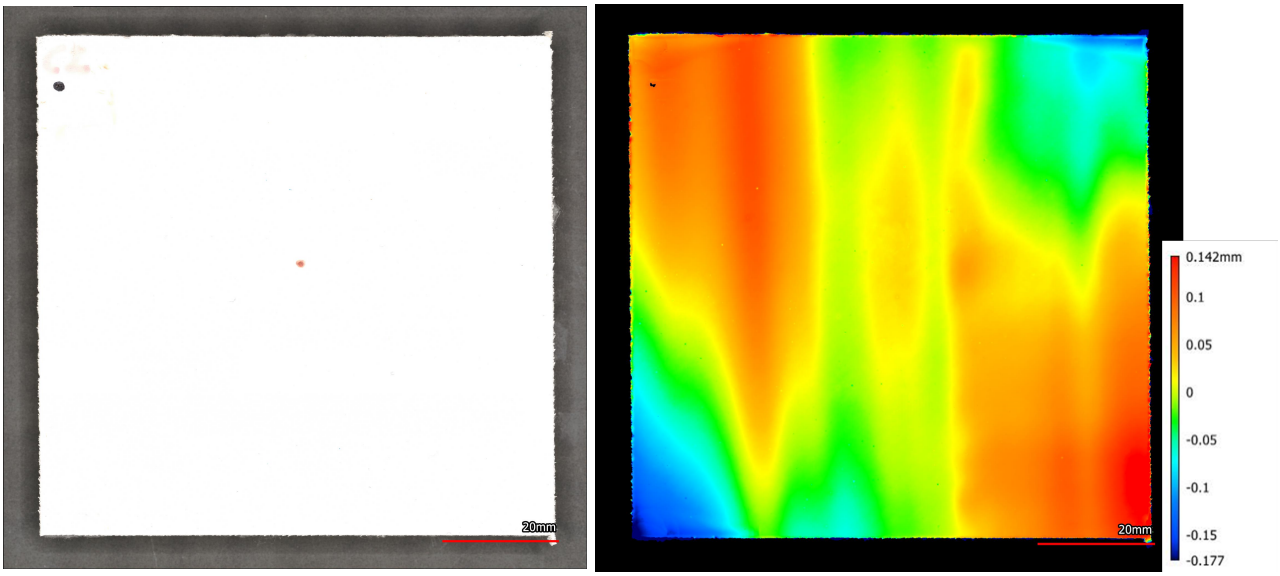

(a) Optical microscope scan of sample **(b)** Height map of sample

Figure D.2: Optical microscopy pictures of Sample C2 after 10 impacts of 15 mm SHI

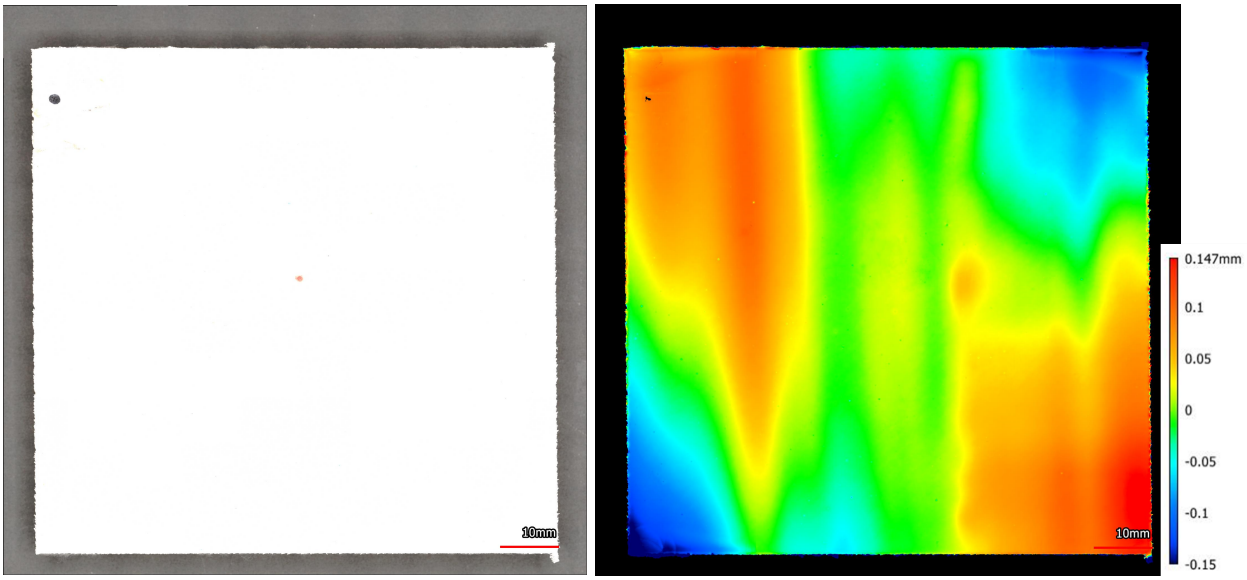

(a) Optical microscope scan of sample **(b)** Height map of sample

Figure D.3: Optical microscopy pictures of Sample C2 after 15 impacts of 15 mm SHI

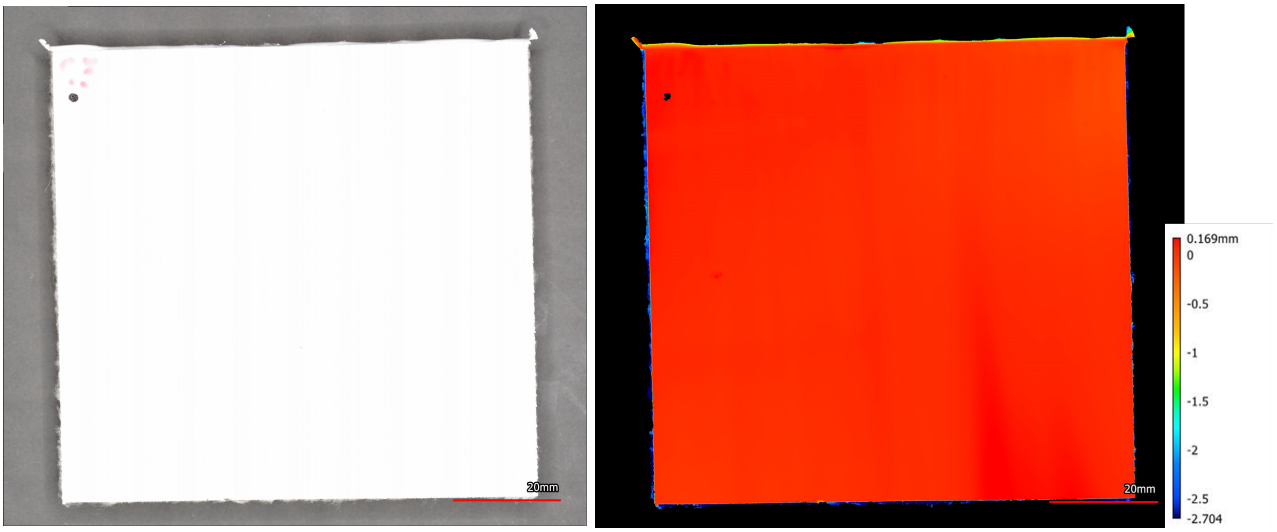

(a) Optical microscope scan of sample

(b) Height map of sample

Figure D.4: Optical microscopy pictures of Sample C3 before impact

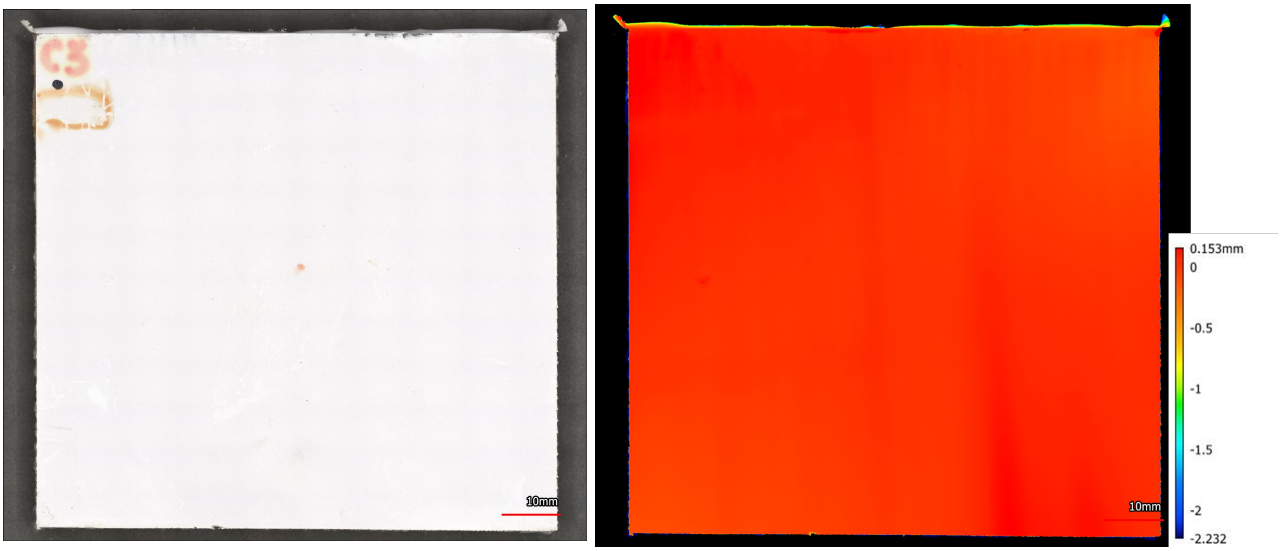

(a) Optical microscope scan of sample

(b) Height map of sample

Figure D.5: Optical microscopy pictures of Sample C3 after 10 impacts of 15 mm SHI

(a) Optical microscope scan of sample **(b)** Height map of sample

Figure D.6: Optical microscopy pictures of Sample C3 after 15 impacts of 15 mm SHI

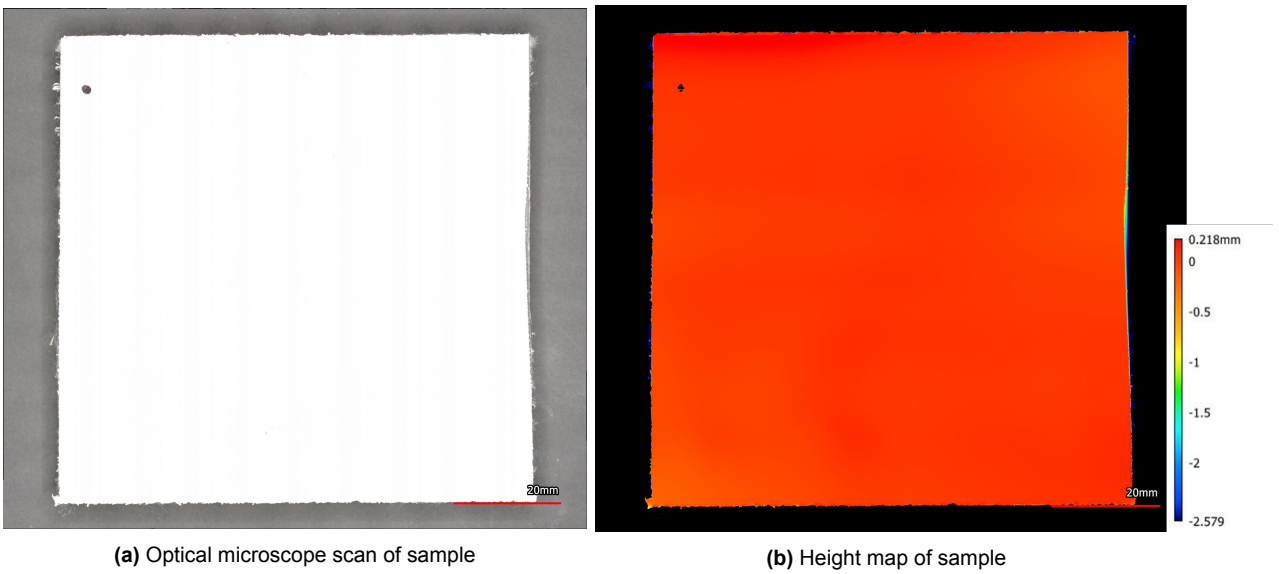

(a) Optical microscope scan of sample **(b)** Height map of sample

Figure D.7: Optical microscopy pictures of Sample C4 before impact

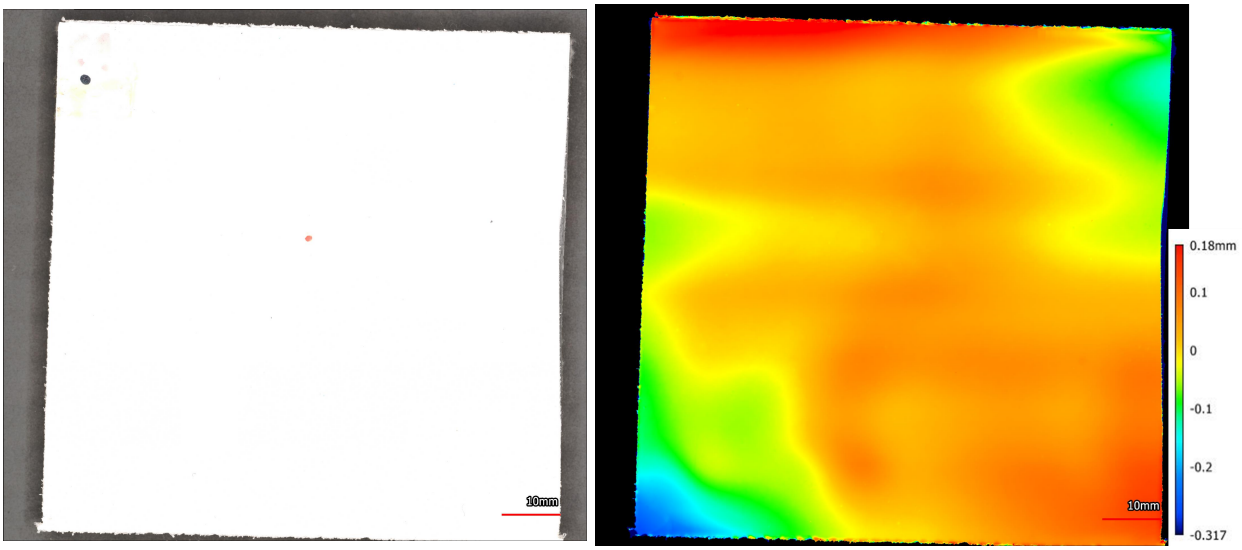

(a) Optical microscope scan of sample

(b) Height map of sample

Figure D.8: Optical microscopy pictures of Sample C4 after 10 impacts of 15 mm SHI

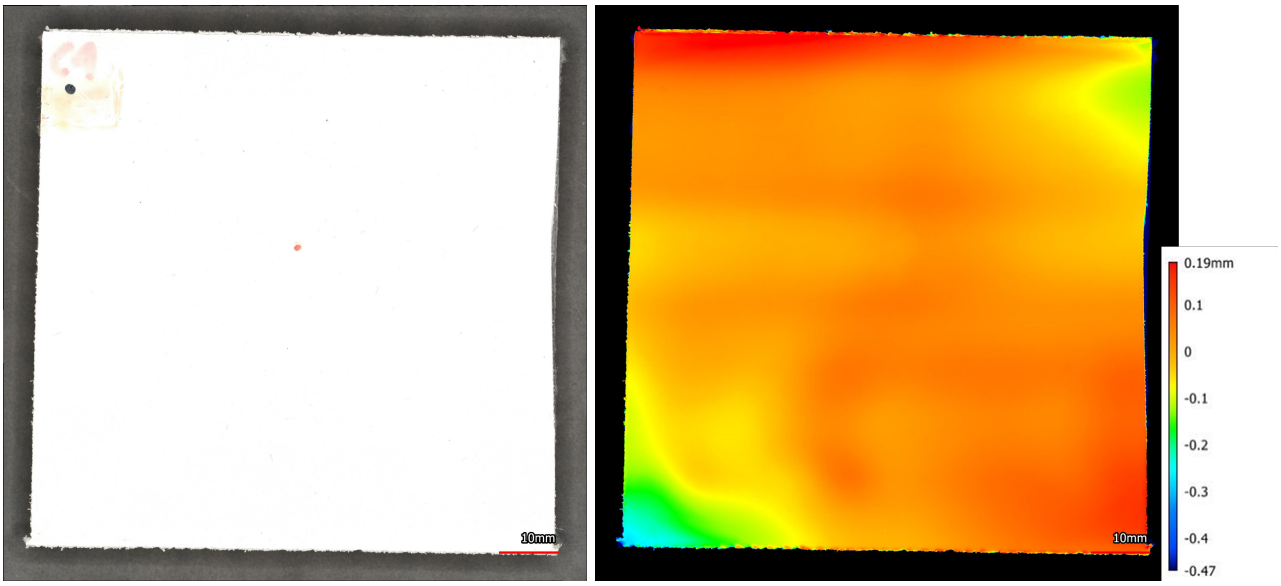

(a) Optical microscope scan of sample

(b) Height map of sample

Figure D.9: Optical microscopy pictures of Sample C4 after 15 impacts of 15 mm SHI

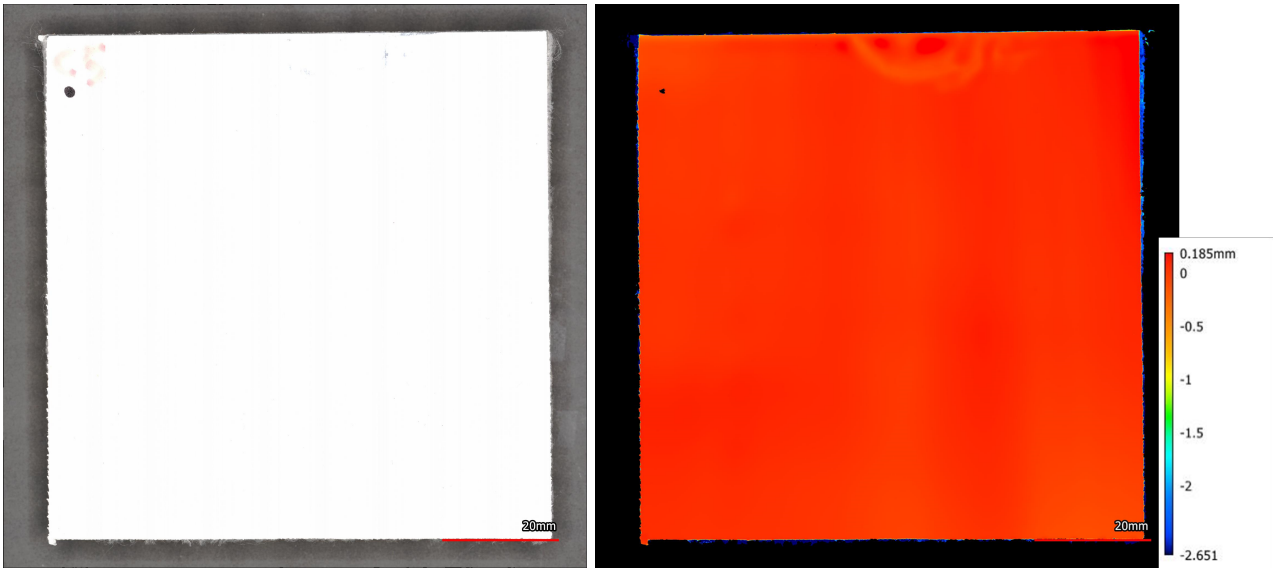

(a) Optical microscope scan of sample **(b)** Height map of sample

Figure D.10: Optical microscopy pictures of Sample C5 before impact

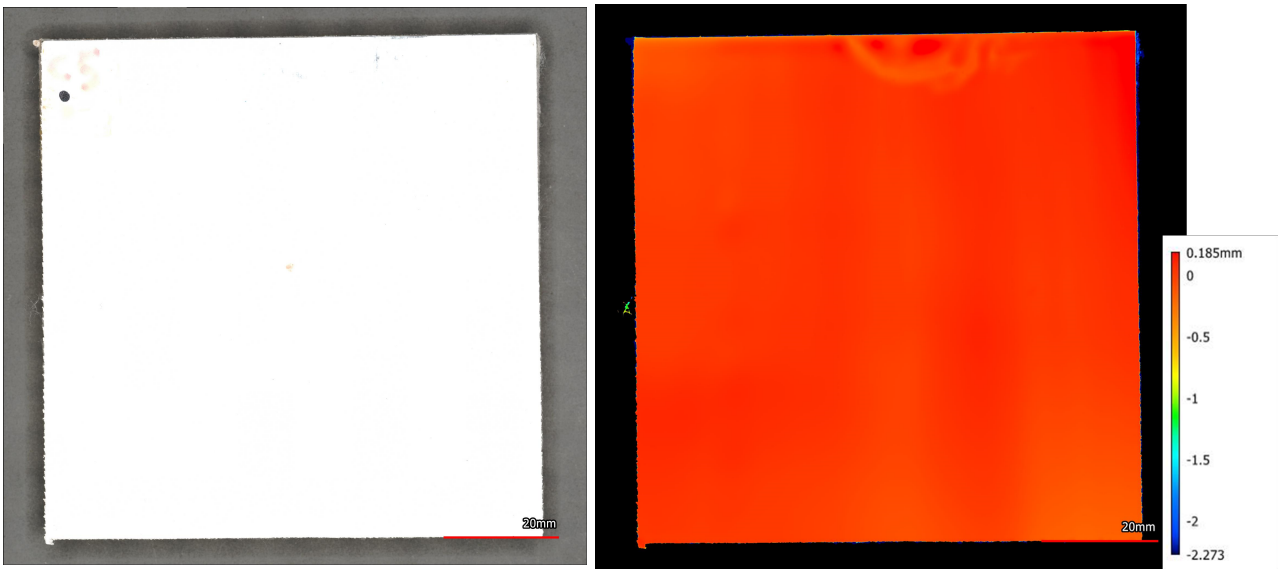

(a) Optical microscope scan of sample **(b)** Height map of sample

Figure D.11: Optical microscopy pictures of Sample C5 after 10 impacts of 15 mm SHI

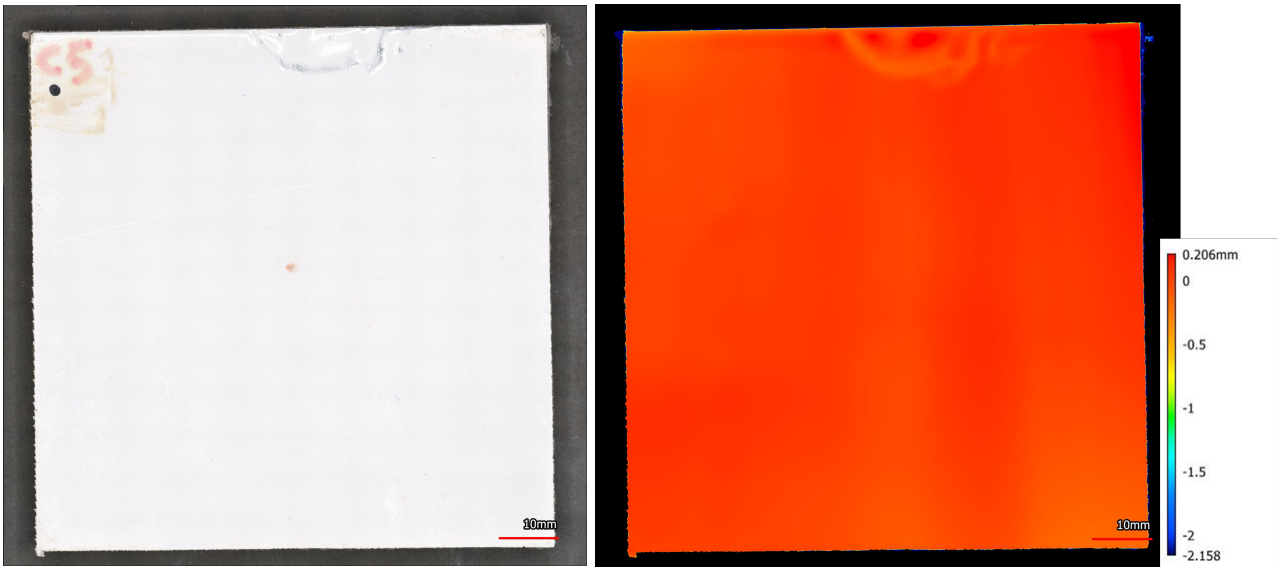

(a) Optical microscope scan of sample **(b)** Height map of sample

Figure D.12: Optical microscopy pictures of Sample C5 after 15 impacts of 15 mm SHI

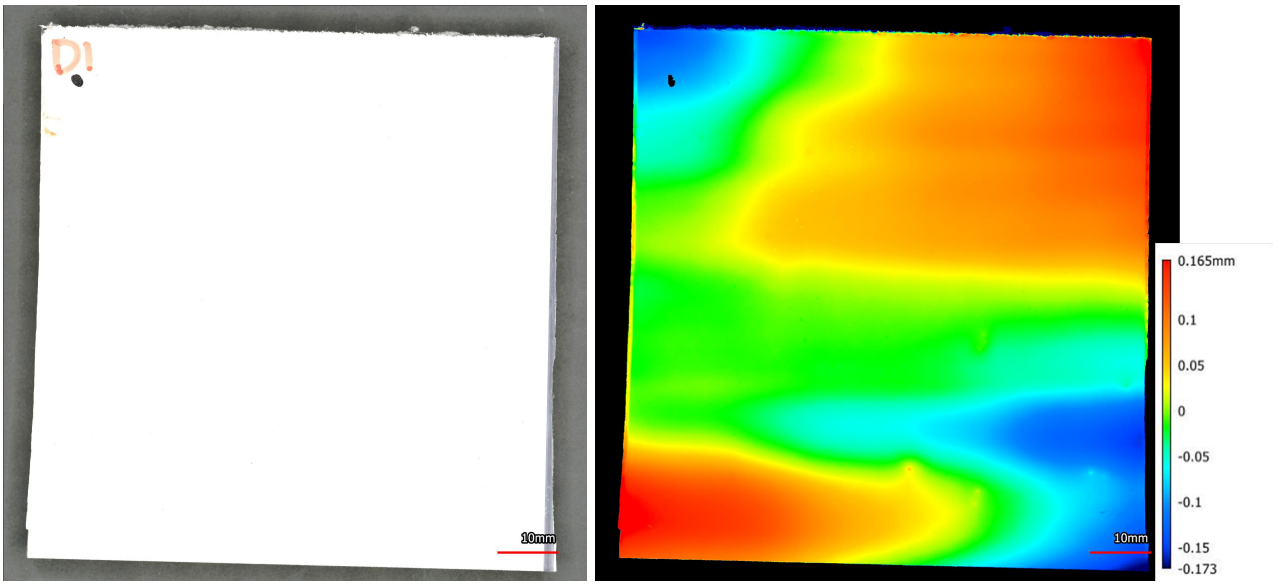

(a) Optical microscope scan of sample **(b)** Height map of sample

Figure D.13: Optical microscopy pictures of Sample D1 before impact

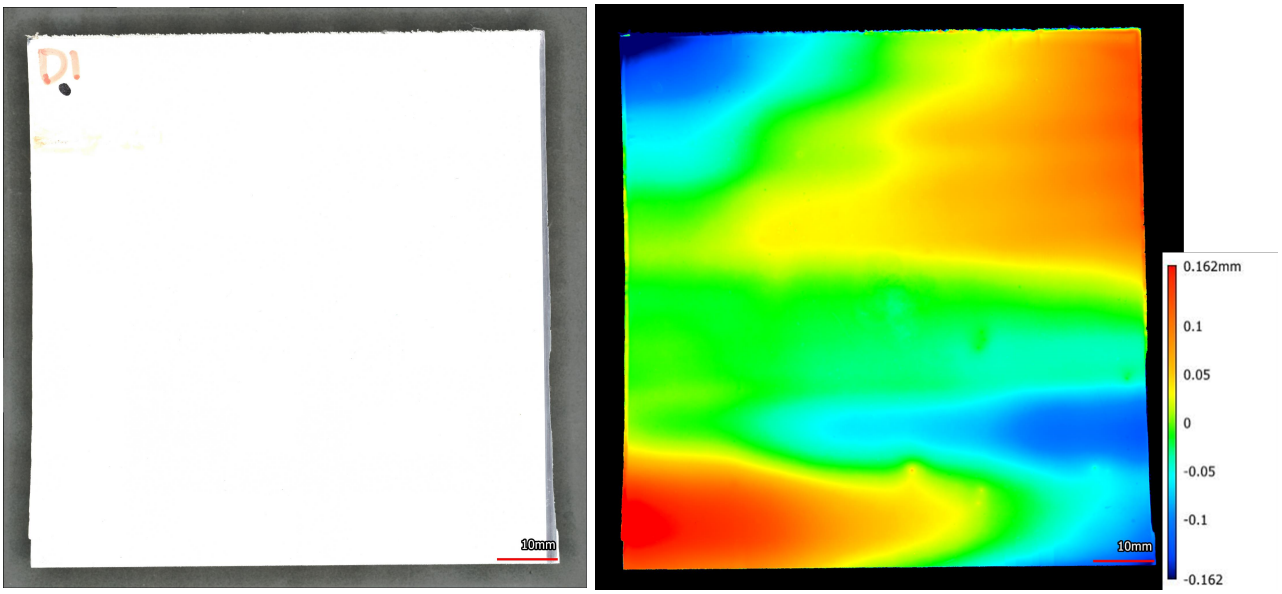

(a) Optical microscope scan of sample **(b)** Height map of sample

Figure D.14: Optical microscopy pictures of Sample D1 after 10 impacts of 15 mm SHI

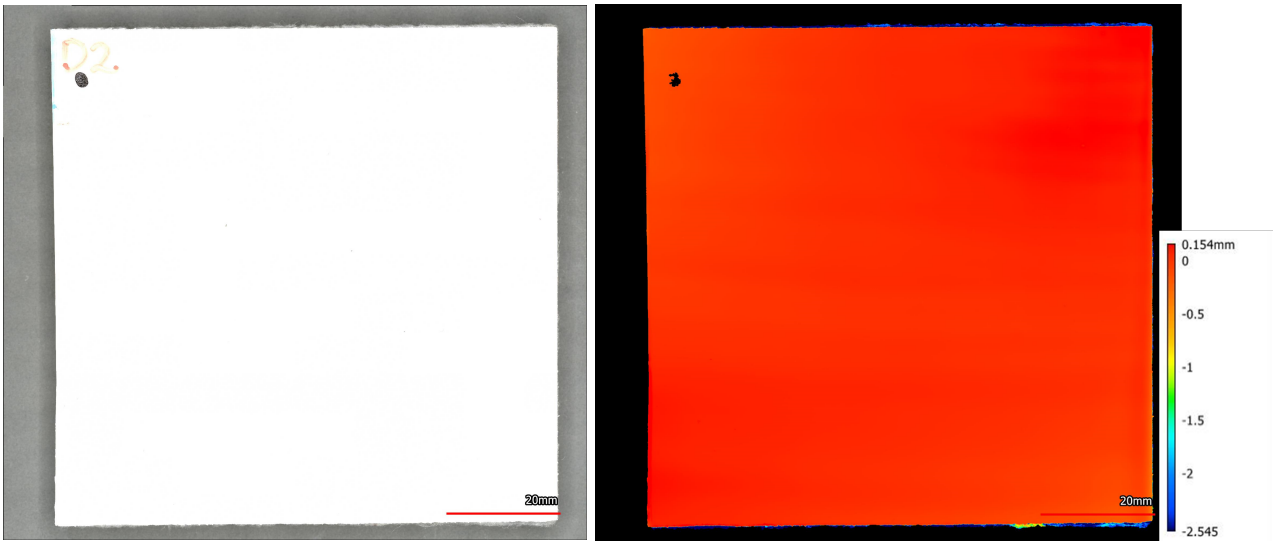

(a) Optical microscope scan of sample **(b)** Height map of sample

Figure D.15: Optical microscopy pictures of Sample D2 before impact

(a) Optical microscope scan of sample

(b) Height map of sample

Figure D.16: Optical microscopy pictures of Sample D2 after 10 impacts of 15 mm SHI

Front side of samples impacted with 20 mm SHI

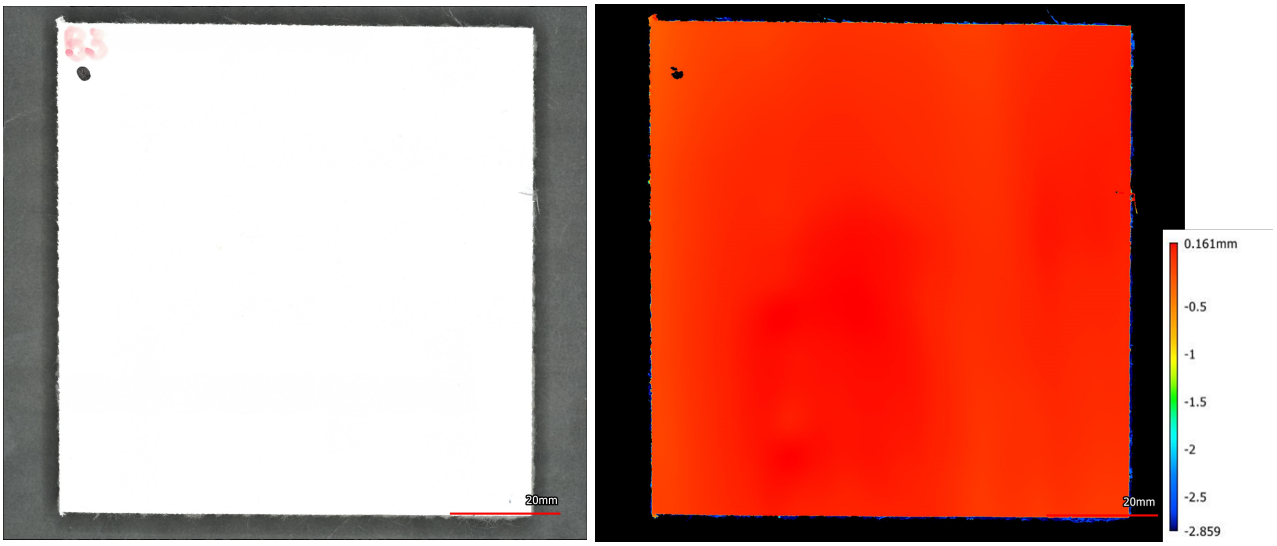

(a) Optical microscope scan of sample

(b) Height map of sample

Figure D.17: Optical microscopy pictures of Sample B3 before impact

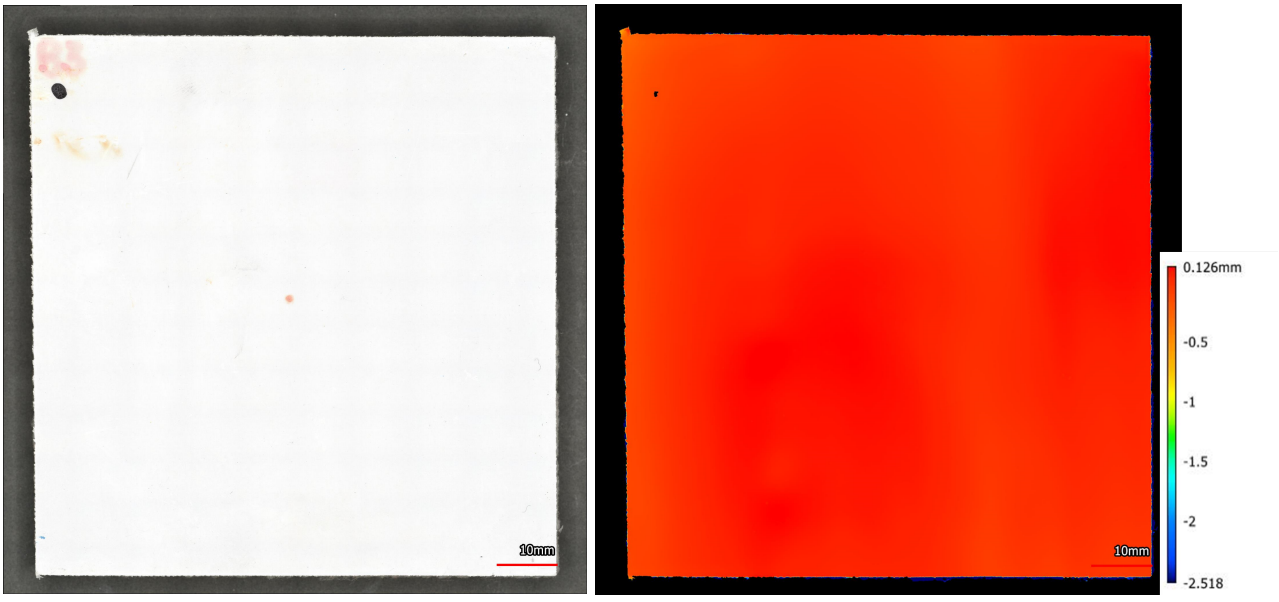

(a) Optical microscope scan of sample

(b) Height map of sample

Figure D.18: Optical microscopy pictures of Sample B3 after 10 impacts of 20 mm SHI

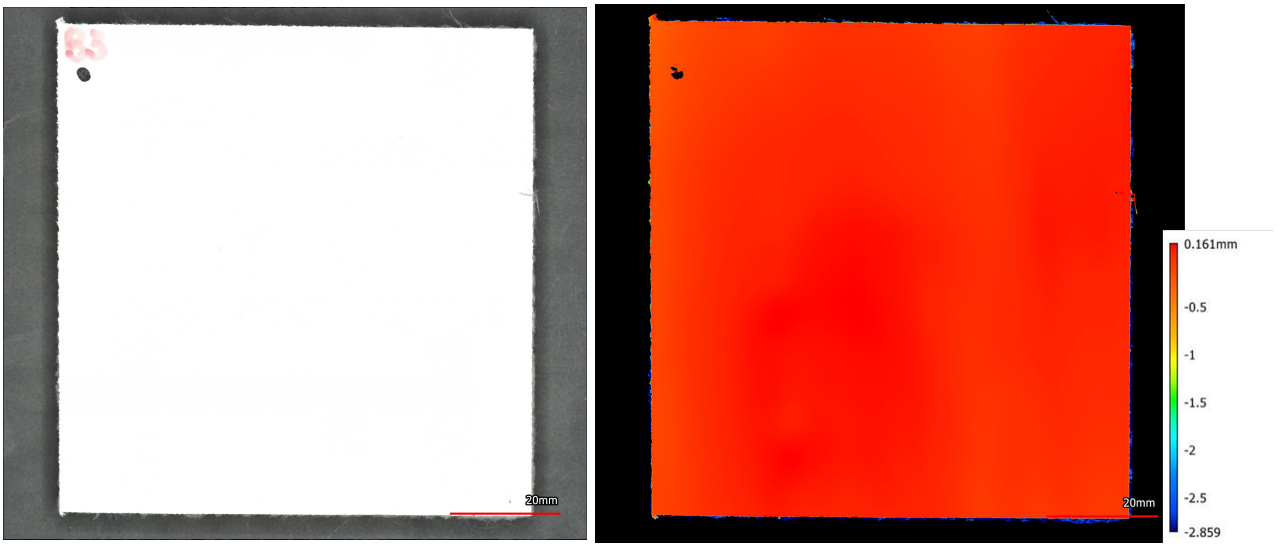

(a) Optical microscope scan of sample **(b)** Height map of sample

Figure D.19: Optical microscopy pictures of Sample B4 before impact

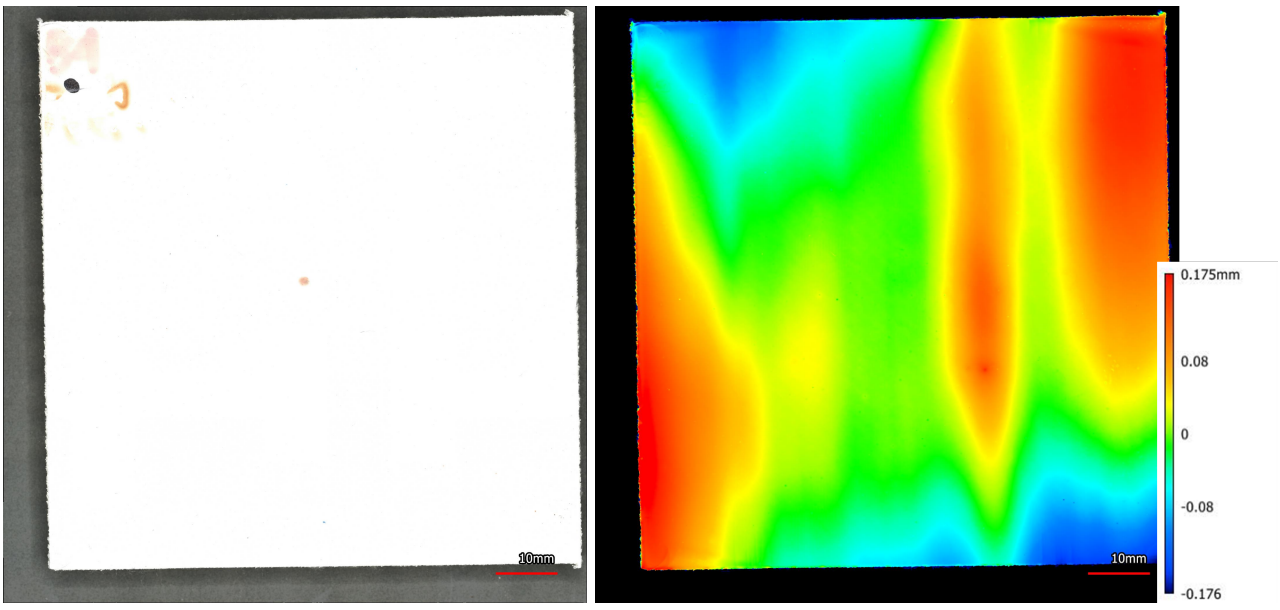

(a) Optical microscope scan of sample **(b)** Height map of sample

Figure D.20: Optical microscopy pictures of Sample B4 after 10 impacts of 20 mm SHI

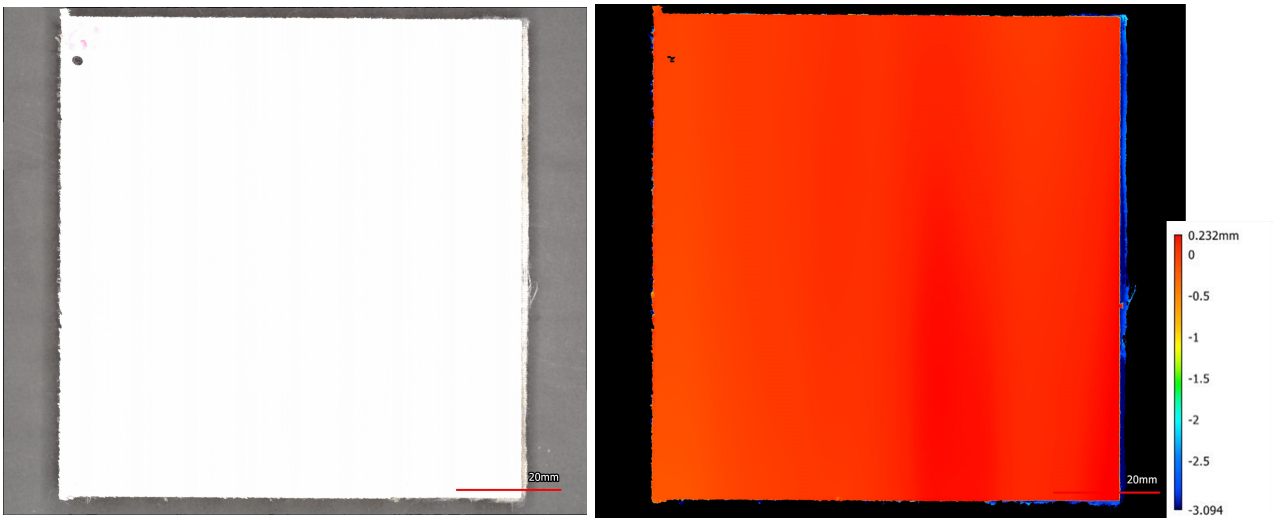

(a) Optical microscope scan of sample

(b) Height map of sample

Figure D.21: Optical microscopy pictures of Sample C1 before impact

(a) Optical microscope scan of sample

(b) Height map of sample

Figure D.22: Optical microscopy pictures of Sample C1 after 10 impacts of 20 mm SHI

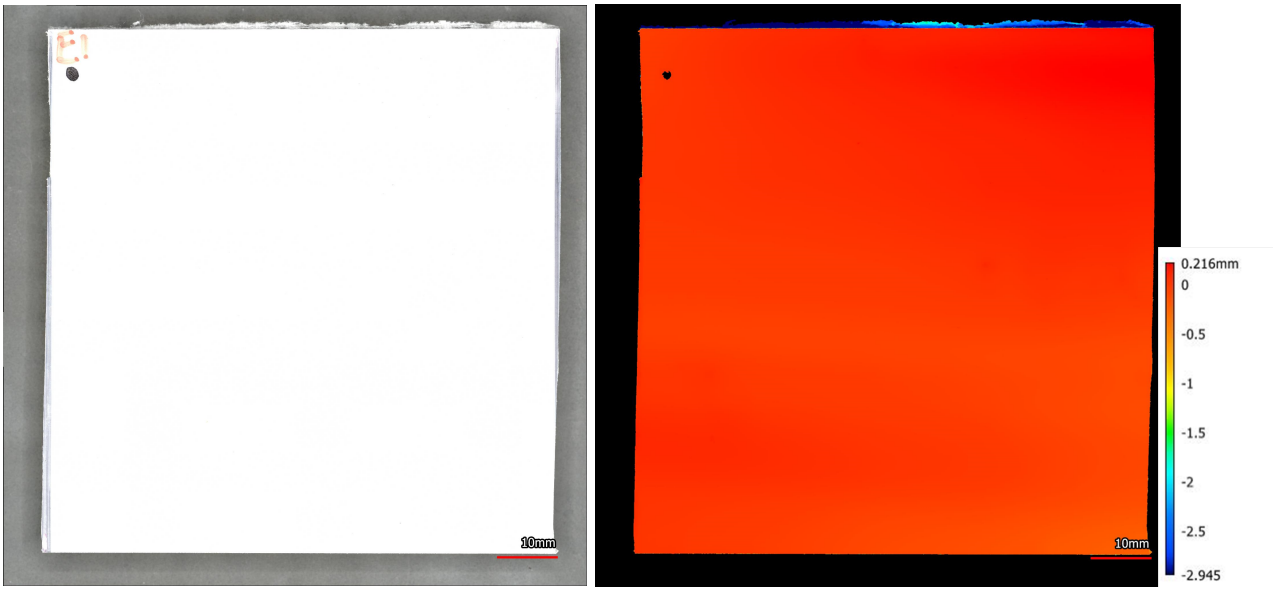

(a) Optical microscope scan of sample **(b)** Height map of sample

Figure D.23: Optical microscopy pictures of Sample E1 before impact

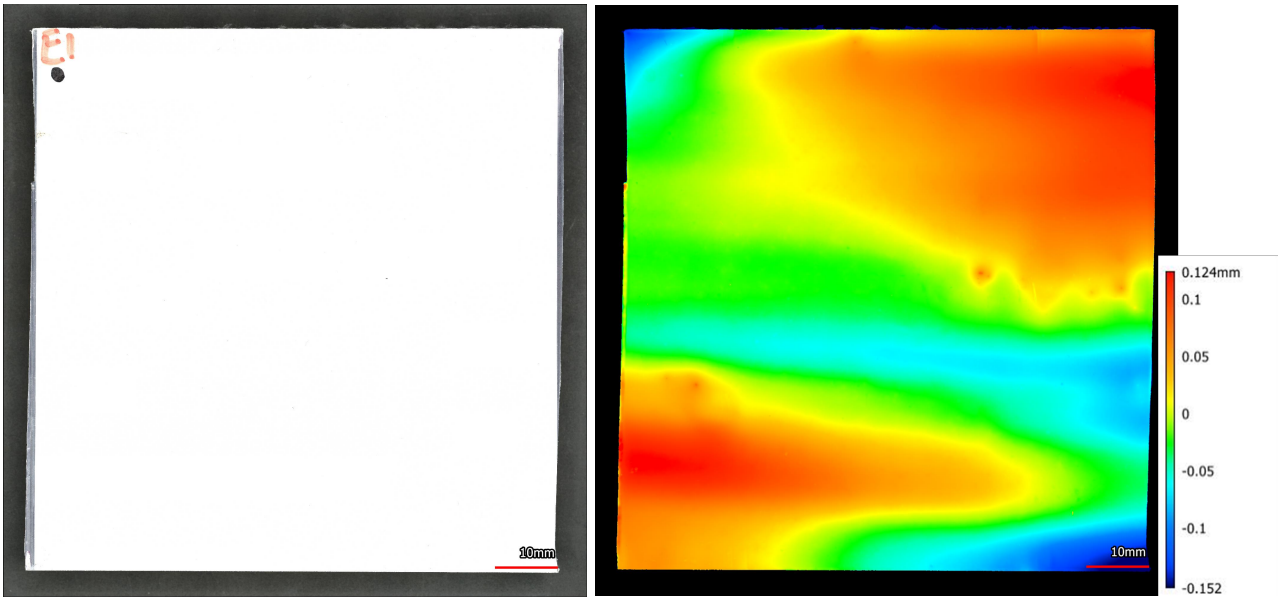

(a) Optical microscope scan of sample **(b)** Height map of sample

Figure D.24: Optical microscopy pictures of Sample E1 after 5 impacts of 20 mm SHI

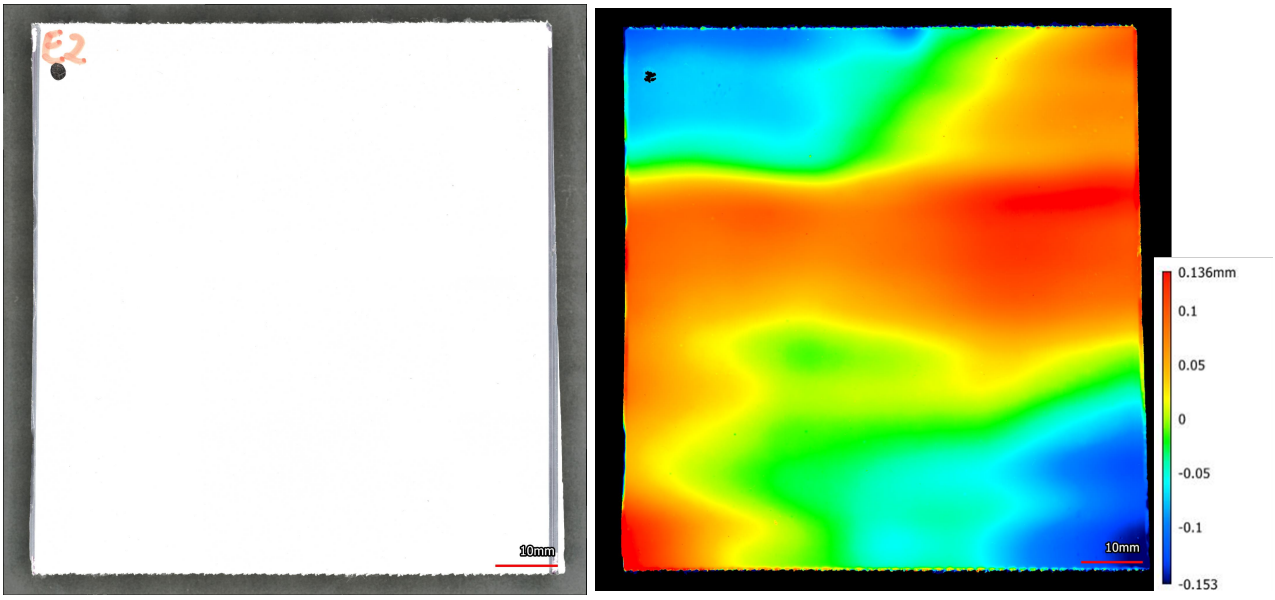

(a) Optical microscope scan of sample **(b)** Height map of sample

Figure D.25: Optical microscopy pictures of Sample E2 before impact

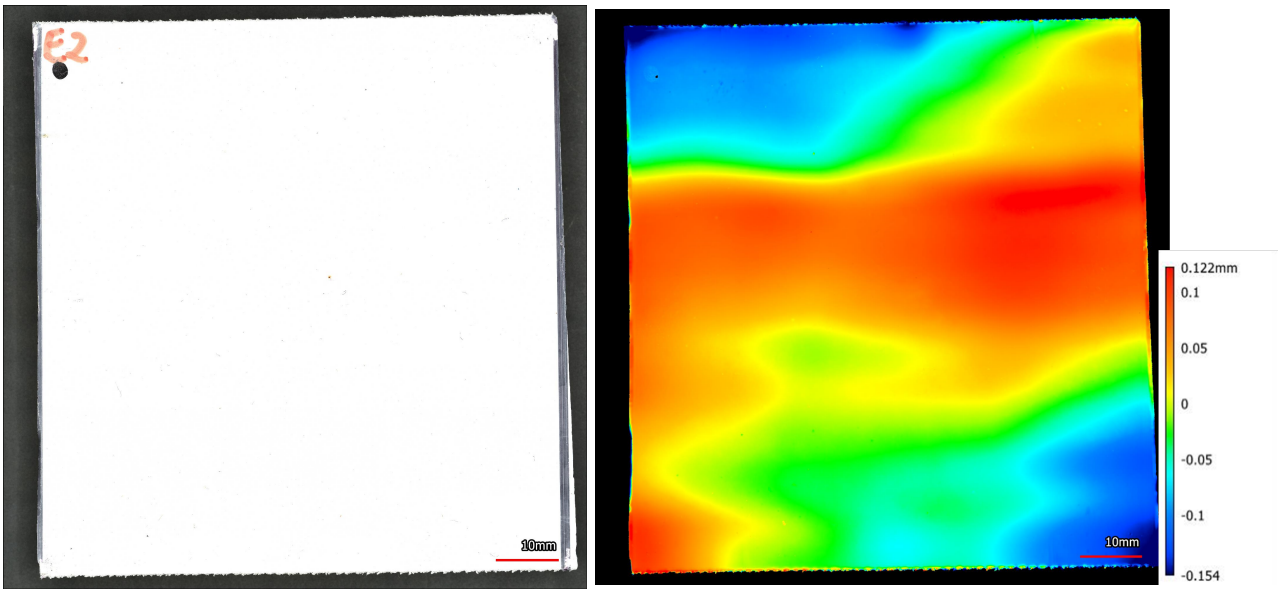

(a) Optical microscope scan of sample **(b)** Height map of sample

Figure D.26: Optical microscopy pictures of Sample E2 after 5 impacts of 20 mm SHI

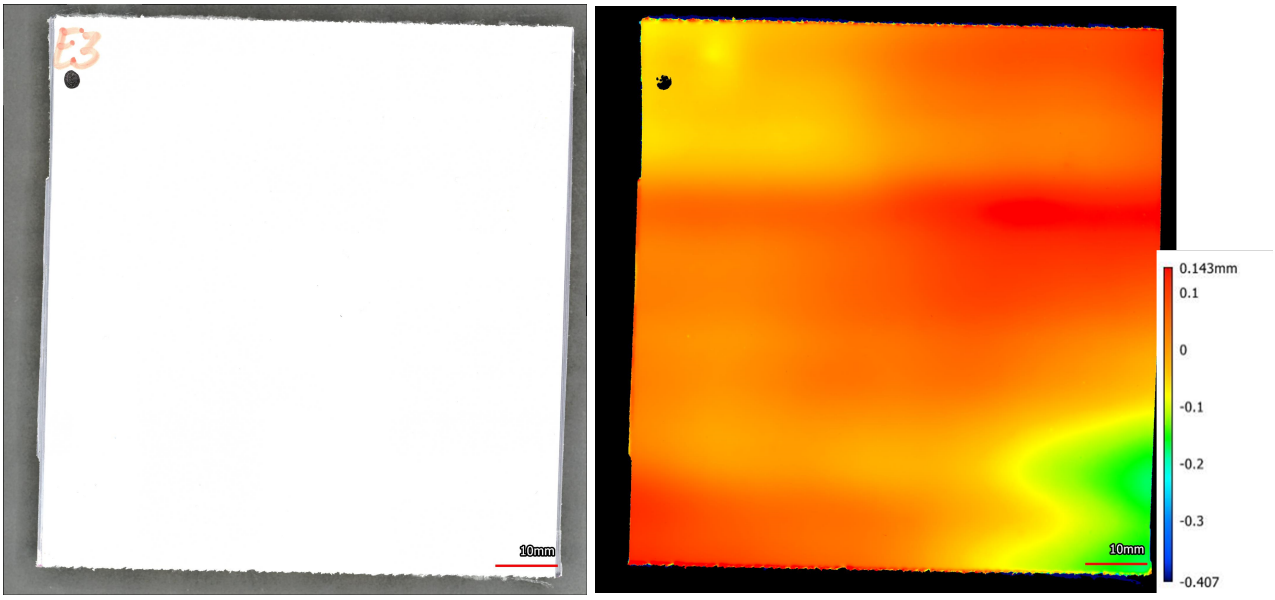

(a) Optical microscope scan of sample **(b)** Height map of sample

Figure D.27: Optical microscopy pictures of Sample E3 before impact

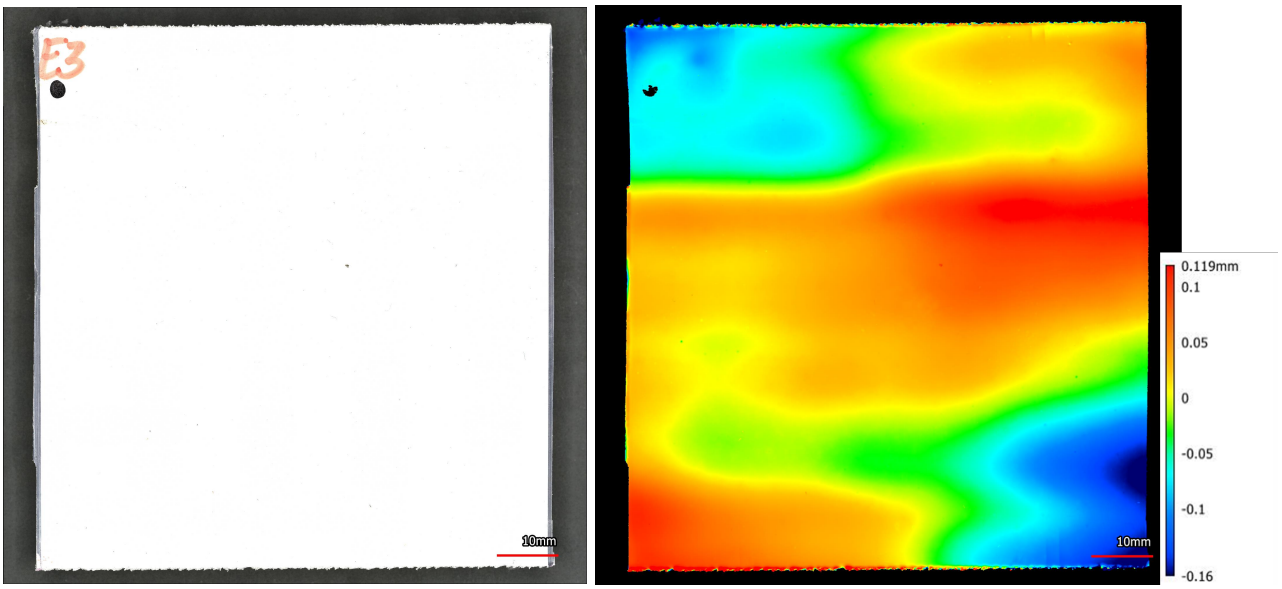

(a) Optical microscope scan of sample **(b)** Height map of sample

Figure D.28: Optical microscopy pictures of Sample E3 after 5 impacts of 20 mm SHI

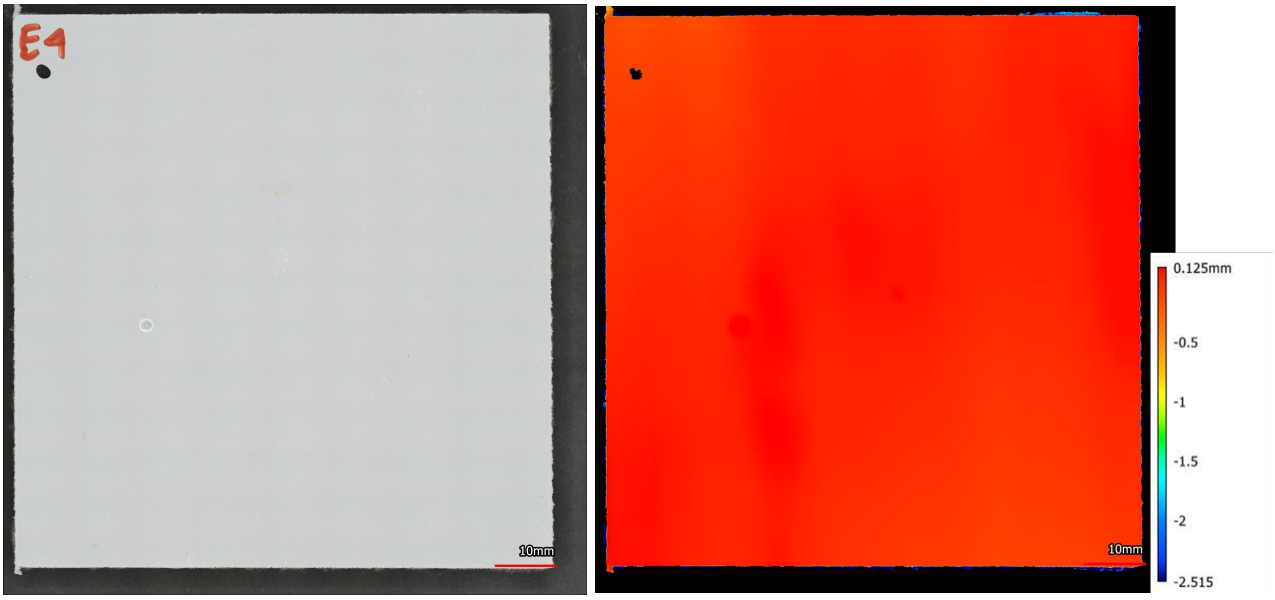

(a) Optical microscope scan of sample **(b)** Height map of sample

Figure D.29: Optical microscopy pictures of Sample E4 before impact

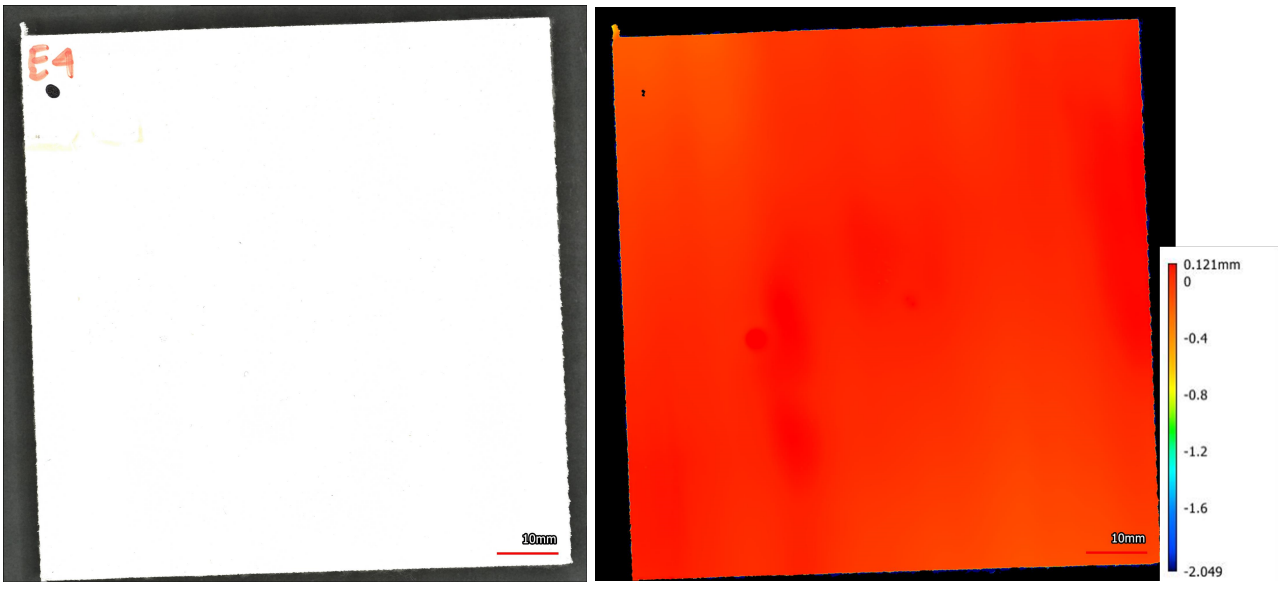

(a) Optical microscope scan of sample **(b)** Height map of sample

Figure D.30: Optical microscopy pictures of Sample E4 after 5 impacts of 20 mm SHI

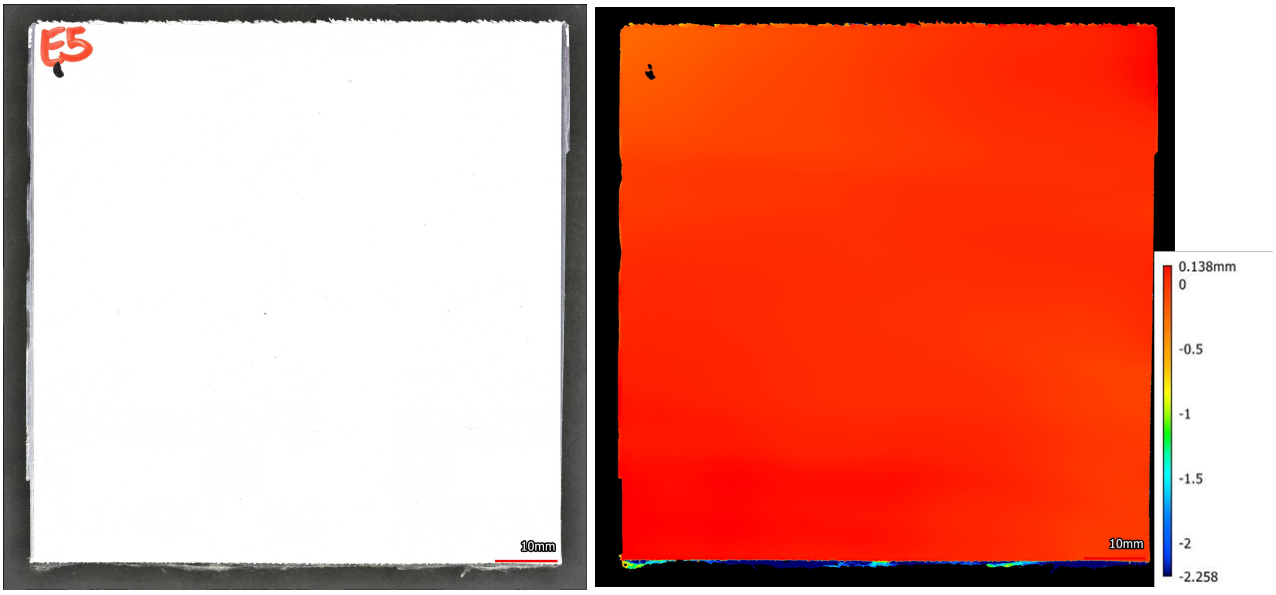

(a) Optical microscope scan of sample **(b)** Height map of sample

Figure D.31: Optical microscopy pictures of Sample E5 before impact

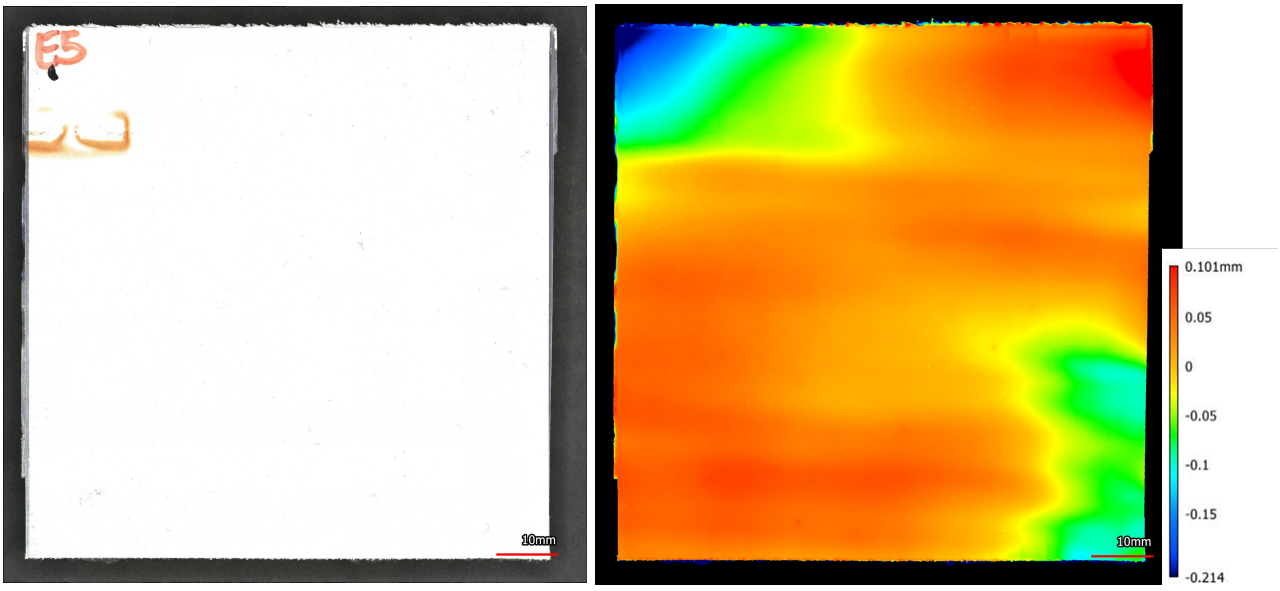

(a) Optical microscope scan of sample **(b)** Height map of sample

Figure D.32: Optical microscopy pictures of Sample E5 after 5 impacts of 20 mm SHI

Rear of samples impacted with 15 mm SHI

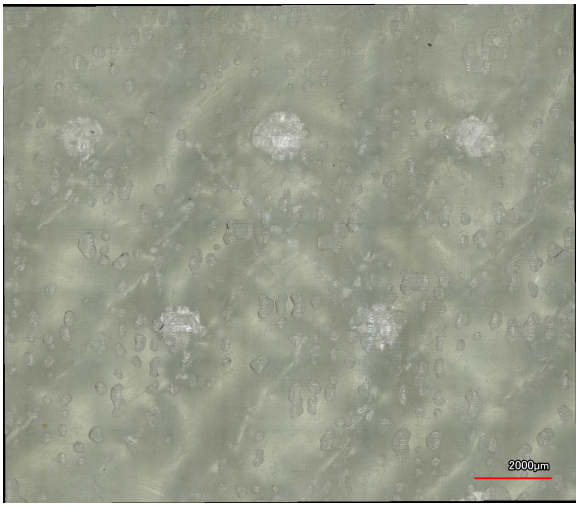

Figure D.33: Optical microscopy picture of rear of Sample D1 after 1 impact of 15 mm SHI, showing matrix cracks in -45◦ direction

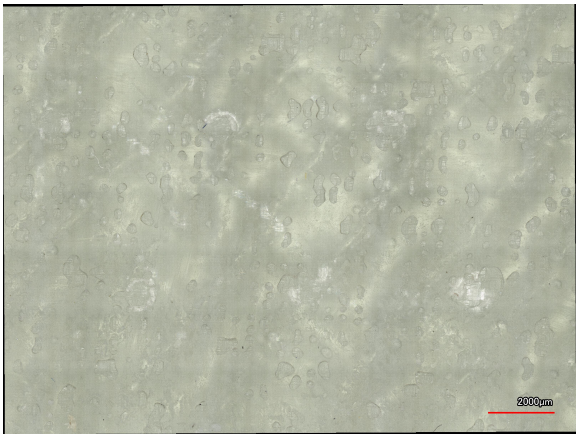

Figure D.34: Optical microscopy picture of rear of Sample D1 after 10 impacts of 15 mm SHI, showing matrix cracks in -45◦ direction

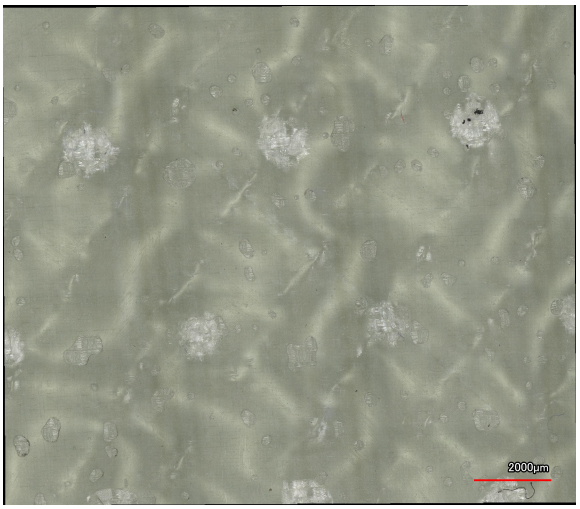

Figure D.35: Optical microscopy picture of rear of Sample D2 after 1 impact of 15 mm SHI, showing matrix cracks in -45◦ direction

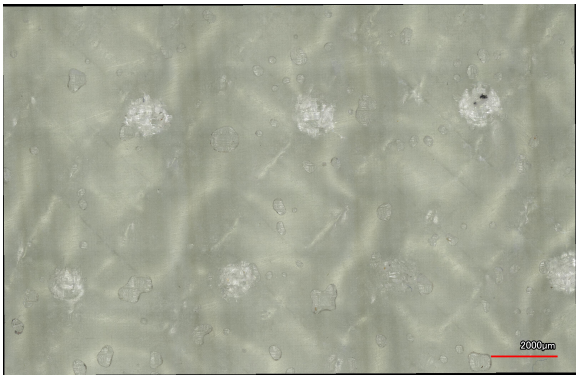

Figure D.36: Optical microscopy picture of rear of Sample D2 after 5 impacts of 15 mm SHI, showing matrix cracks in -45◦ direction

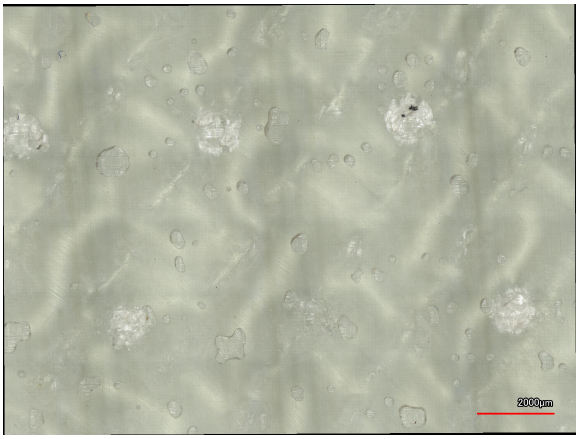

Figure D.37: Optical microscopy picture of rear of Sample D2 after 7 impacts of 15 mm SHI. The matrix cracks can only be seen with coaxial light. This is possibly due to compaction pressure applied while mounting the sample on clay to observe the coating layer

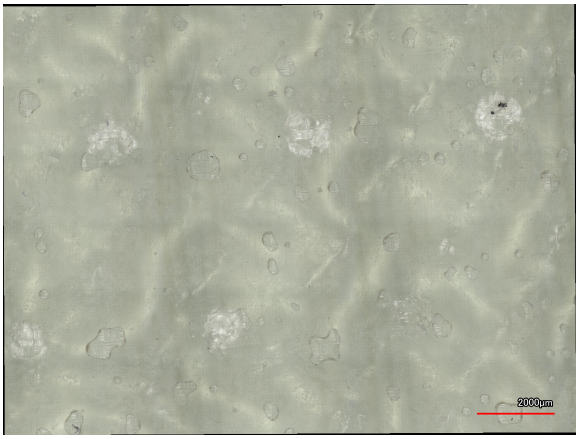

Figure D.38: Optical microscopy picture of rear of Sample D2 after 10 impacts of 15 mm SHI. The matrix cracks can only be seen with coaxial light. This is possibly due to compaction pressure applied while mounting the sample on clay to observe the coating layer

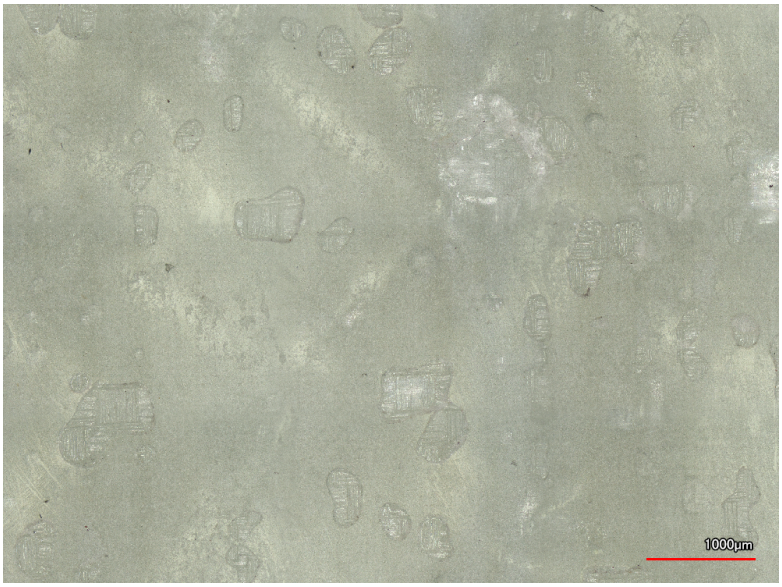

Figure D.39: Closeup picture of matrix crack seen in sample D3 (Figure 4.5)

Rear of samples impacted with 20 mm SHI

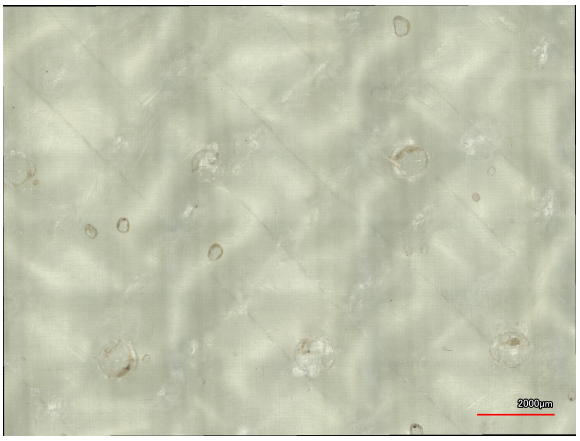

Figure D.40: Optical microscopy picture of rear of Sample B3 after 5 impacts of 20 mm SHI, showing matrix cracks in -45◦ direction

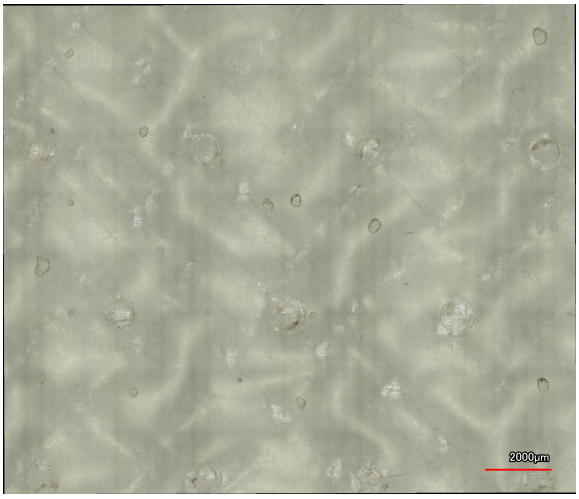

Figure D.41: Optical microscopy picture of rear of Sample B3 after 10 impacts of 20 mm SHI, showing matrix cracks in -45◦ direction

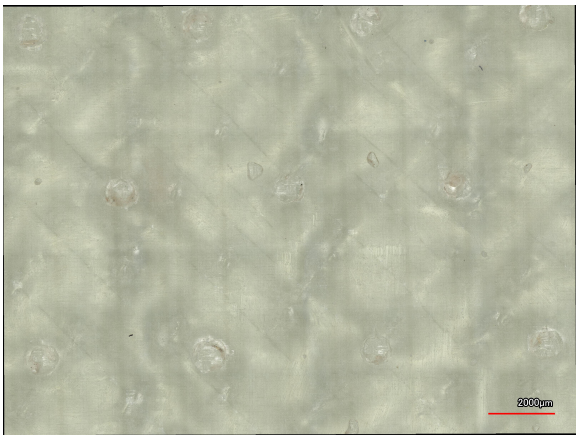

Figure D.42: Optical microscopy picture of rear of Sample B4 after 4 impacts of 20 mm SHI, showing matrix cracks in -45◦ direction

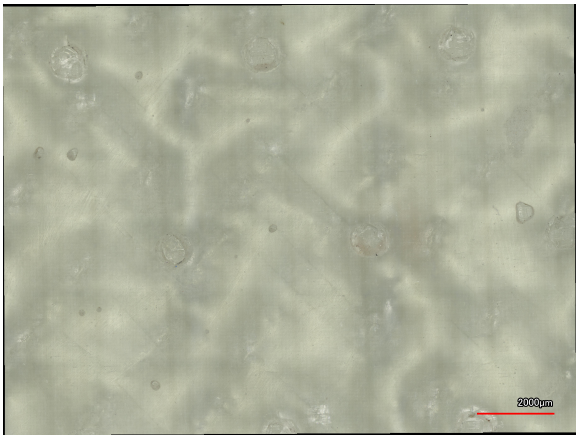

Figure D.43: Optical microscopy picture of rear of Sample B4 after 10 impacts of 20 mm SHI, showing matrix cracks in -45◦ direction

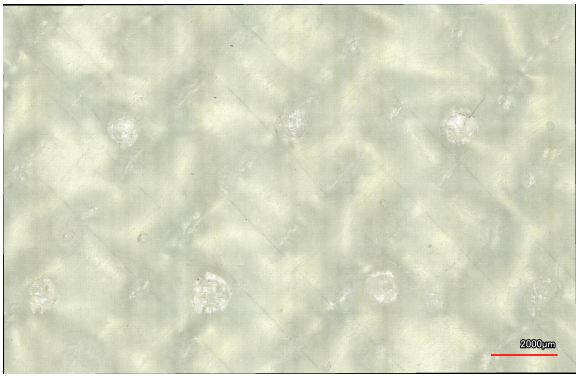

Figure D.44: Optical microscopy picture of rear of Sample B5 after 4 impacts of 20 mm SHI, showing matrix cracks in -45◦ direction

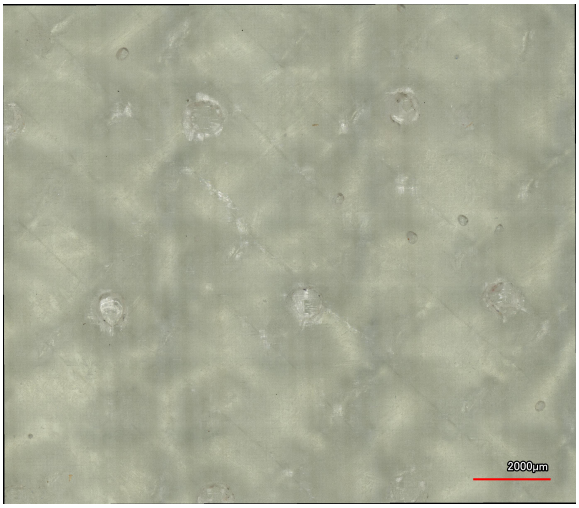

Figure D.45: Optical microscopy picture of rear of Sample B5 after 7 impacts of 20 mm SHI, showing matrix cracks in -45◦ direction

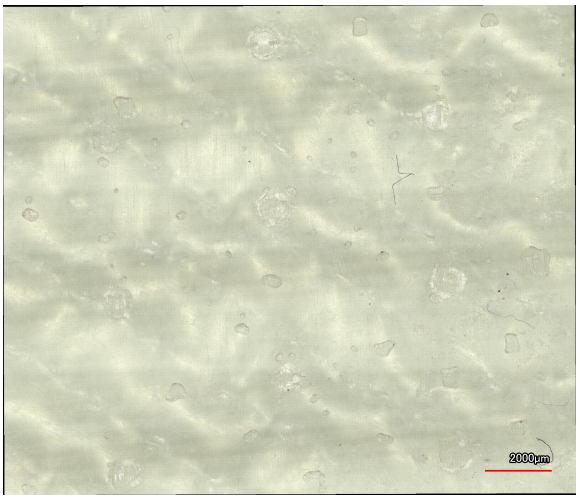

Figure D.46: Optical microscopy picture of rear of Sample C1 after 3 impacts of 20 mm SHI. No matrix cracks are visible due to the breaking of the hailstones for the first 3 impacts for this sample

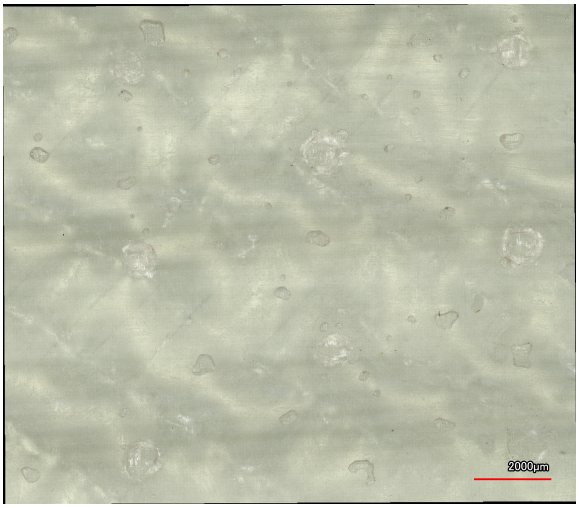

Figure D.47: Optical microscopy picture of rear of Sample C1 after 10 impacts of 20 mm SHI, showing matrix cracks in 45◦ direction. This change in orientation is possibly due to a different orientation while clamping of the sample inside the impact chamber

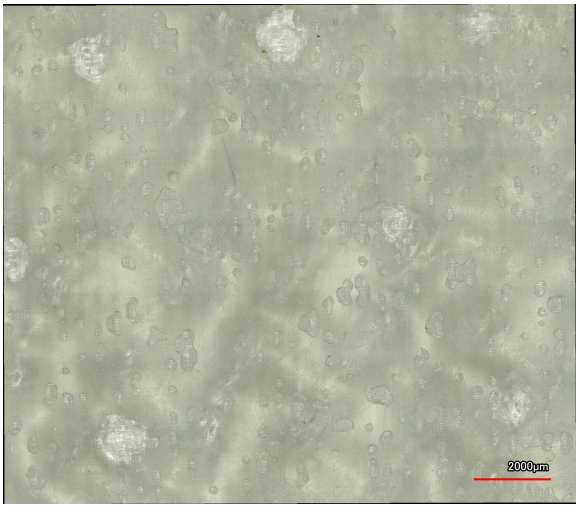

Figure D.48: Optical microscopy picture of rear of Sample E1 after 1 impact of 20 mm SHI. No matrix cracks are visible in this sample

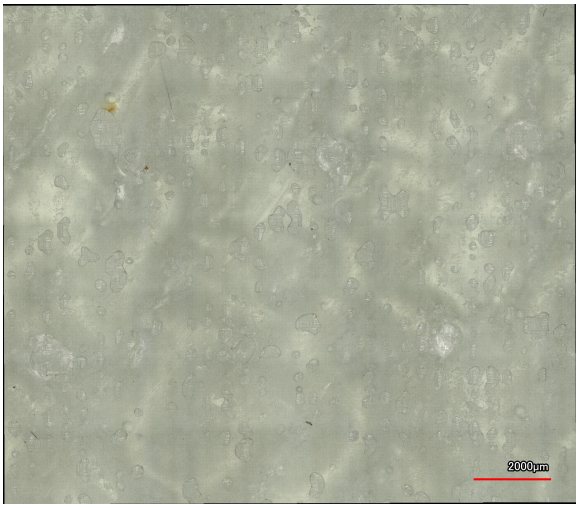

Figure D.49: Optical microscopy picture of rear of Sample E1 after 5 impacts of 20 mm SHI. No matrix cracks are visible in this sample

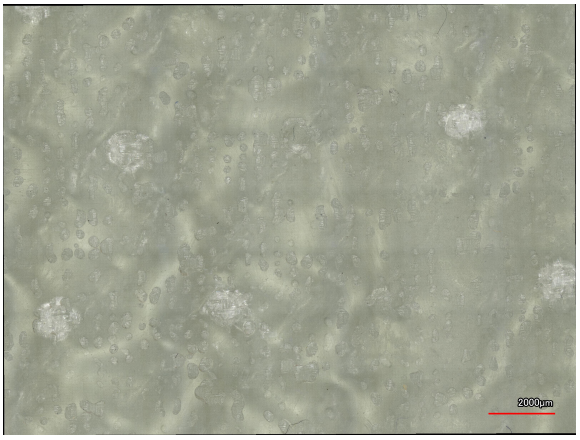

Figure D.50: Optical microscopy picture of rear of Sample E2 after 1 impact of 20 mm SHI. No matrix cracks are visible in this sample

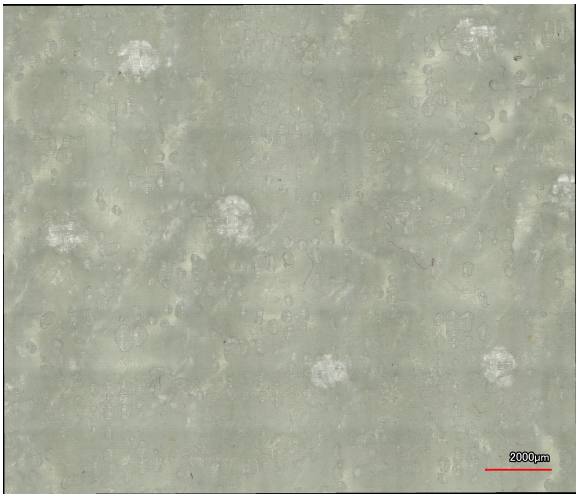

Figure D.51: Optical microscopy picture of rear of Sample E2 after 5 impacts of 20 mm SHI. No matrix cracks are visible in this sample

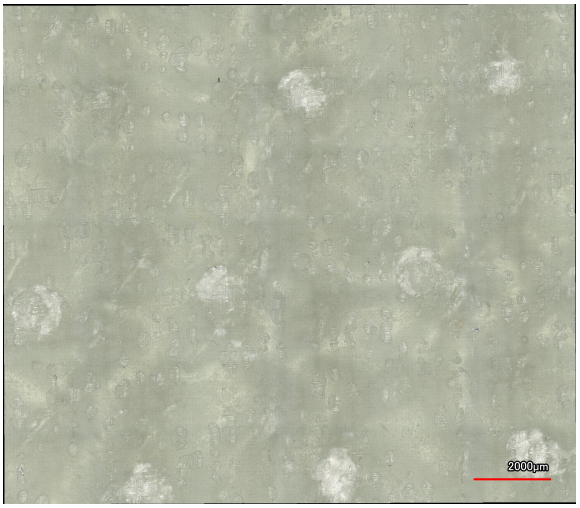

Figure D.52: Optical microscopy picture of rear of Sample E3 after 1 impact of 20 mm SHI. No matrix cracks are visible in this picture. However, cracks were seen when viewed under coaxial light

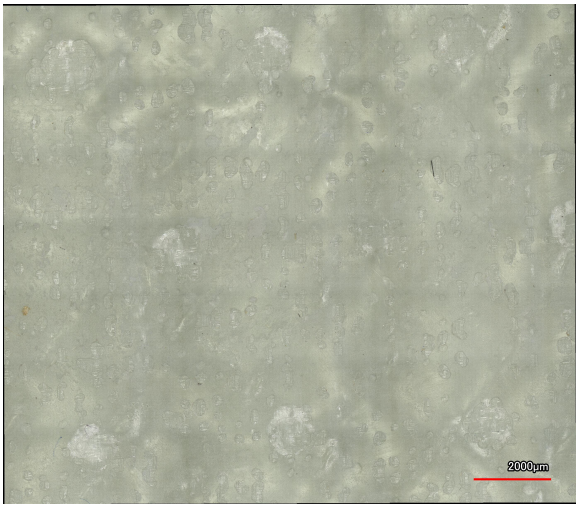

Figure D.53: Optical microscopy picture of rear of Sample E3 after 5 impacts of 20 mm SHI. No matrix cracks are visible in this picture. However, cracks were seen when viewed under coaxial light

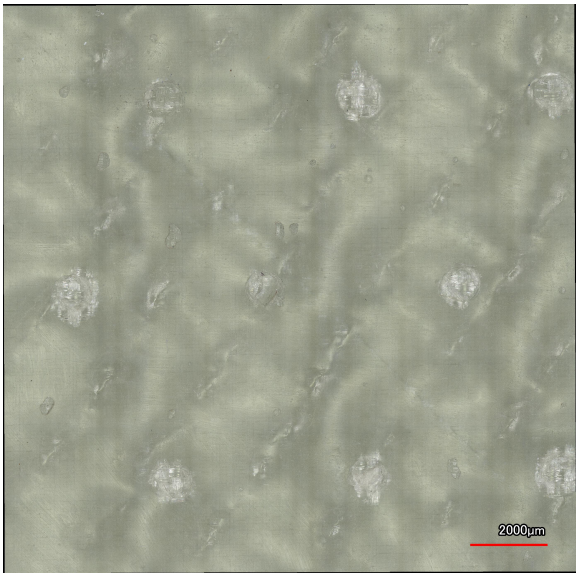

Figure D.54: Optical microscopy picture of rear of Sample E4 after 1 impact of 20 mm SHI, showing matrix cracks in -45◦ direction

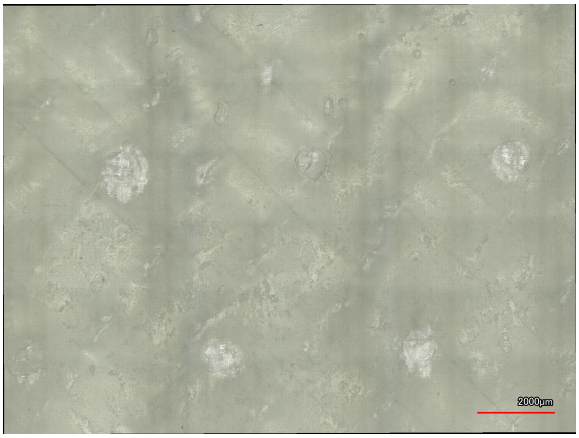

Figure D.55: Optical microscopy picture of rear of Sample E4 after 5 impacts of 20 mm SHI, showing matrix cracks in -45◦ direction

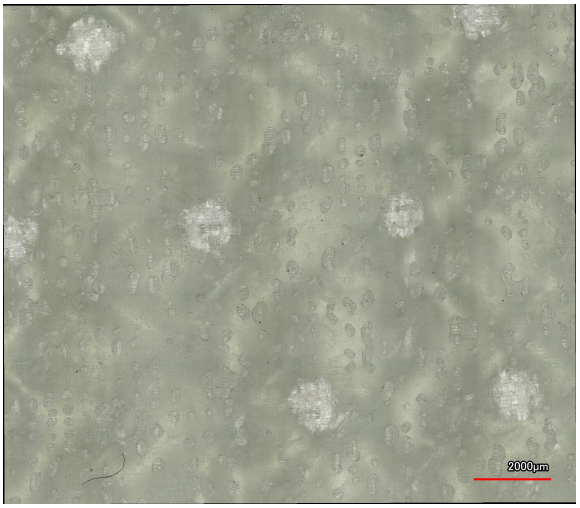

Figure D.56: Optical microscopy picture of rear of Sample E5 after 1 impact of 20 mm SHI. No matrix cracks are visible in this sample

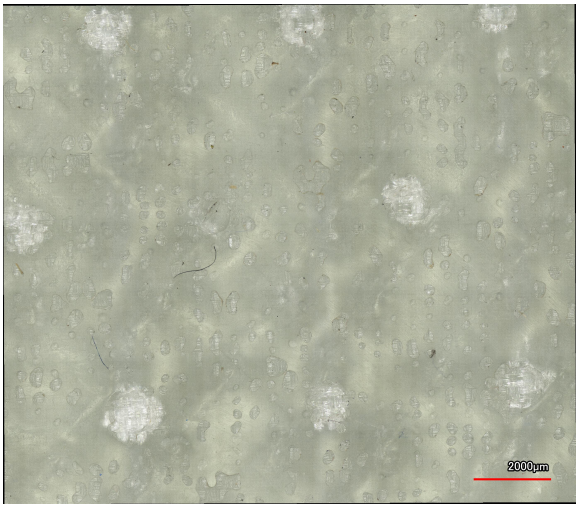

Figure D.57: Optical microscopy picture of rear of Sample E5 after 5 impacts of 20 mm SHI. No matrix cracks are visible in this sample

E

Ultrasonic C-scans

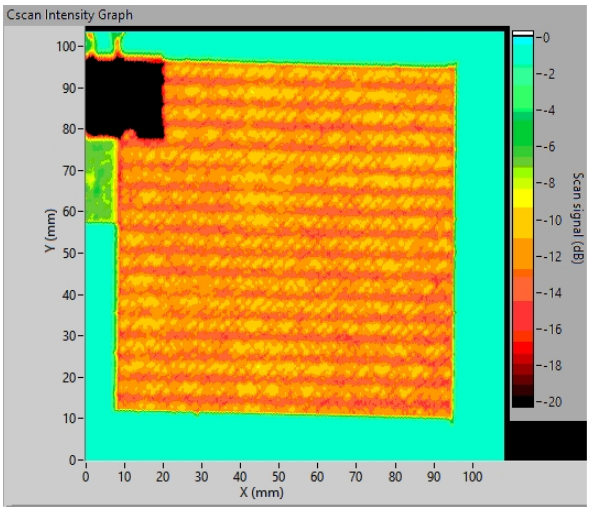

Figure E.1: C-scan of sample C2 after 15 impacts of 15 mm SHI

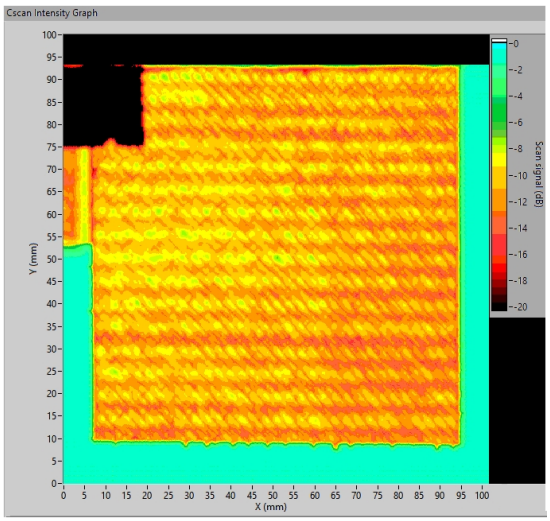

Figure E.2: C-scan of sample C3 after 15 impacts of 20 mm SHI

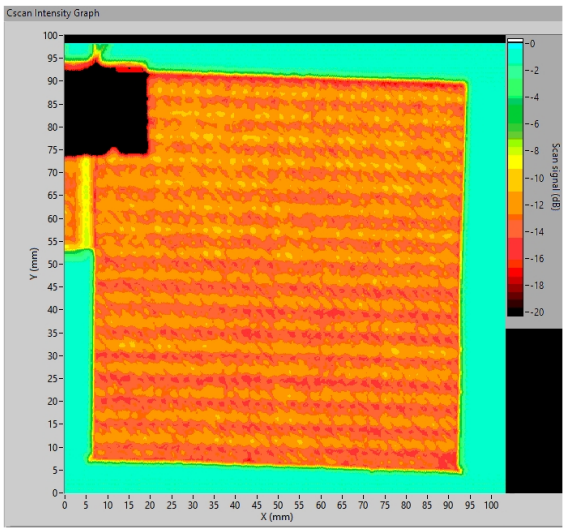

Figure E.3: C-scan of sample C4 after 15 impacts of 15 mm SHI

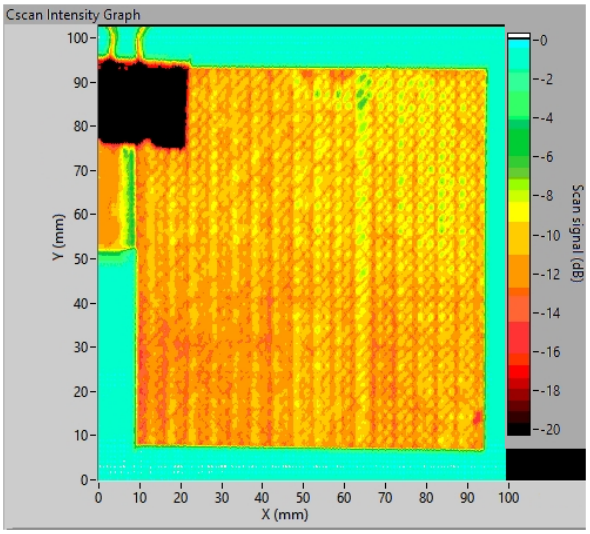

Figure E.4: C-scan of sample C5 after 15 impacts of 20 mm SHI

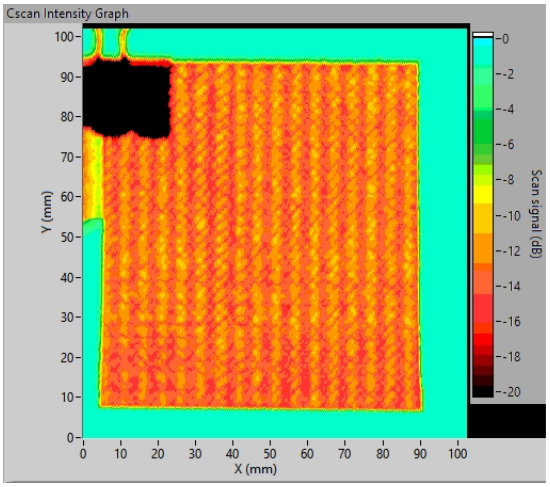

Figure E.5: C-scan of sample D1 after 10 impacts of 15 mm SHI

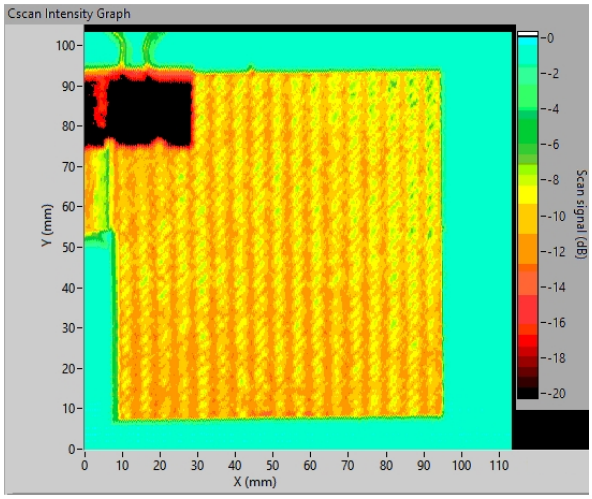

Figure E.6: C-scan of sample D2 after 10 impacts of 20 mm SHI

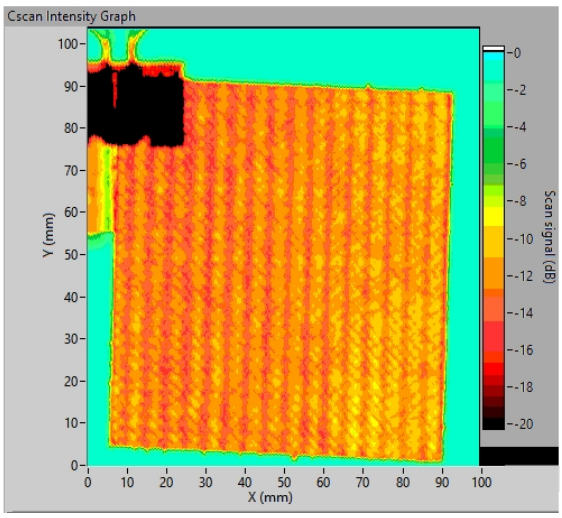

Figure E.7: C-scan of sample B3 after 10 impacts of 20 mm SHI

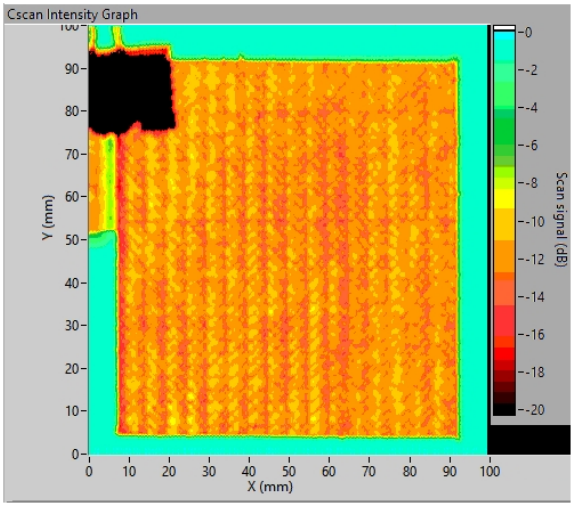

Figure E.8: C-scan of sample B4 after 10 impacts of 20 mm SHI

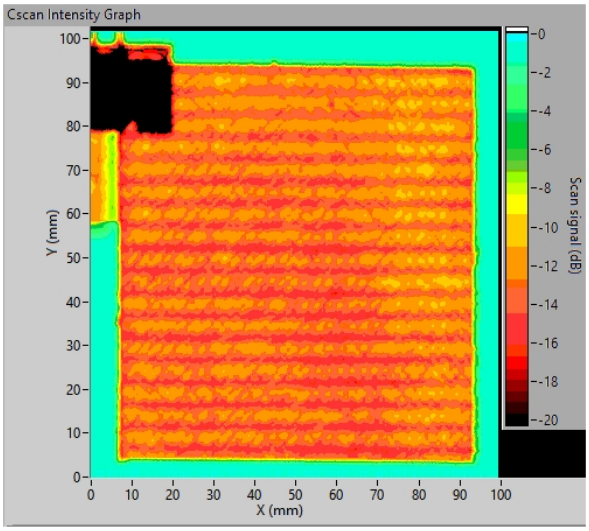

Figure E.9: C-scan of sample C1 after 10 impacts of 20 mm SHI

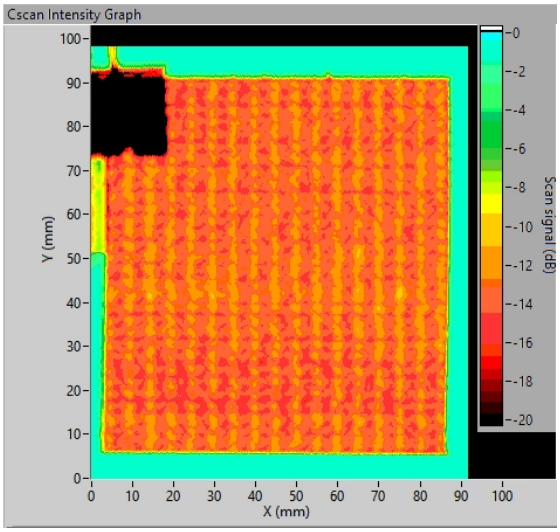

Figure E.10: C-scan of sample E1 after 5 impacts of 20 mm SHI

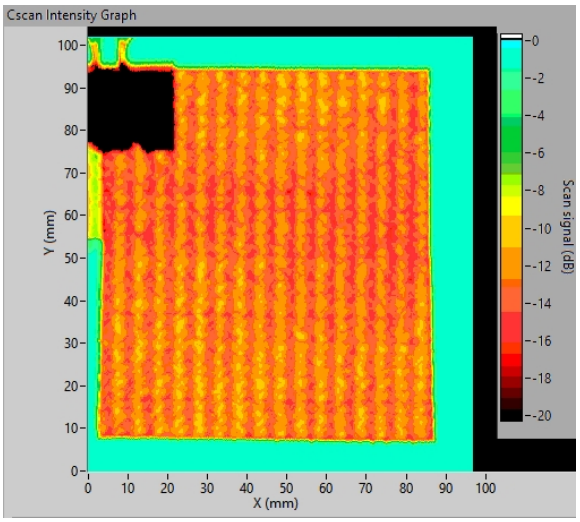

Figure E.11: C-scan of sample E2 after 5 impacts of 20 mm SHI

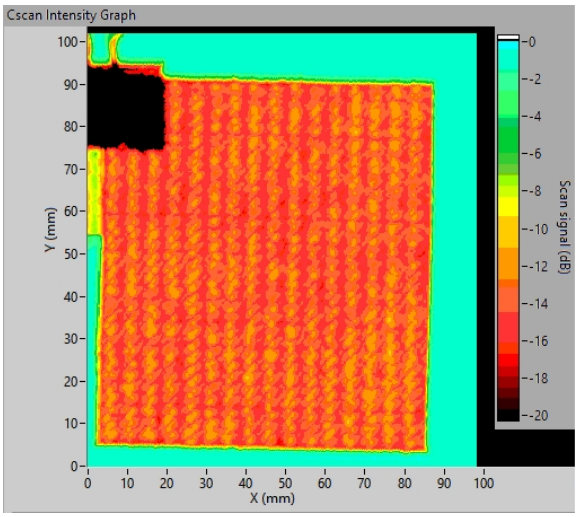

Figure E.12: C-scan of sample E3 after 5 impacts of 20 mm SHI

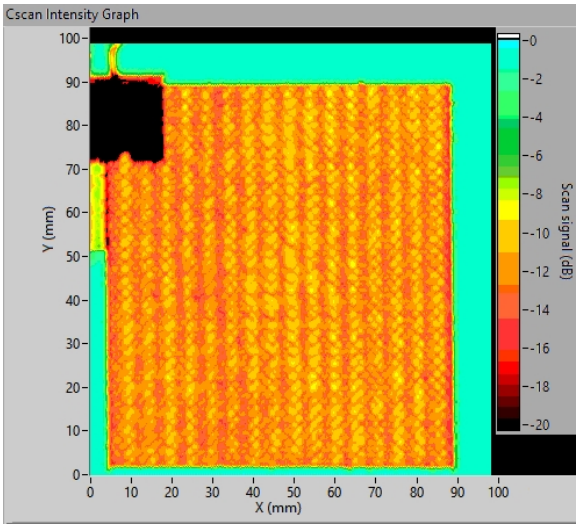

Figure E.13: C-scan of sample E4 after 5 impacts of 20 mm SHI

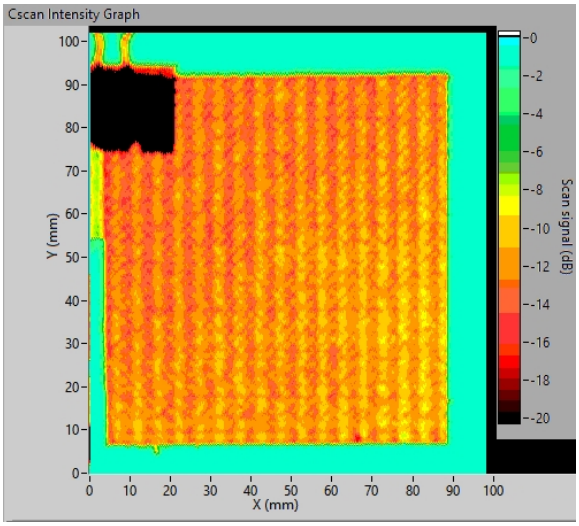

Figure E.14: C-scan of sample E5 after 5 impacts of 20 mm SHI

F

Cross-Sectional Microscopy

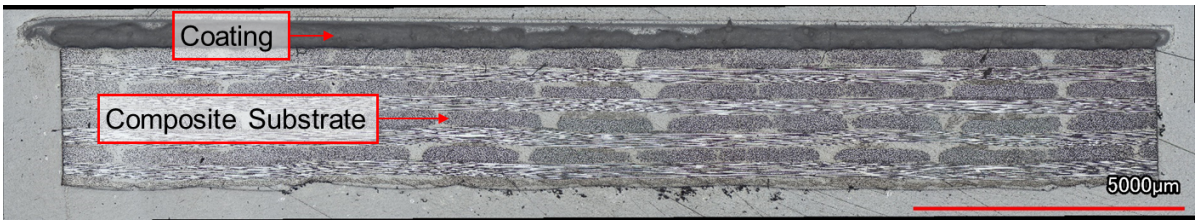

Figure F.1: Optical microscopy picture of the cross-section of Sample C2 after 15 impacts of 15 mm SHI. No matrix cracks were observed in this cross-section

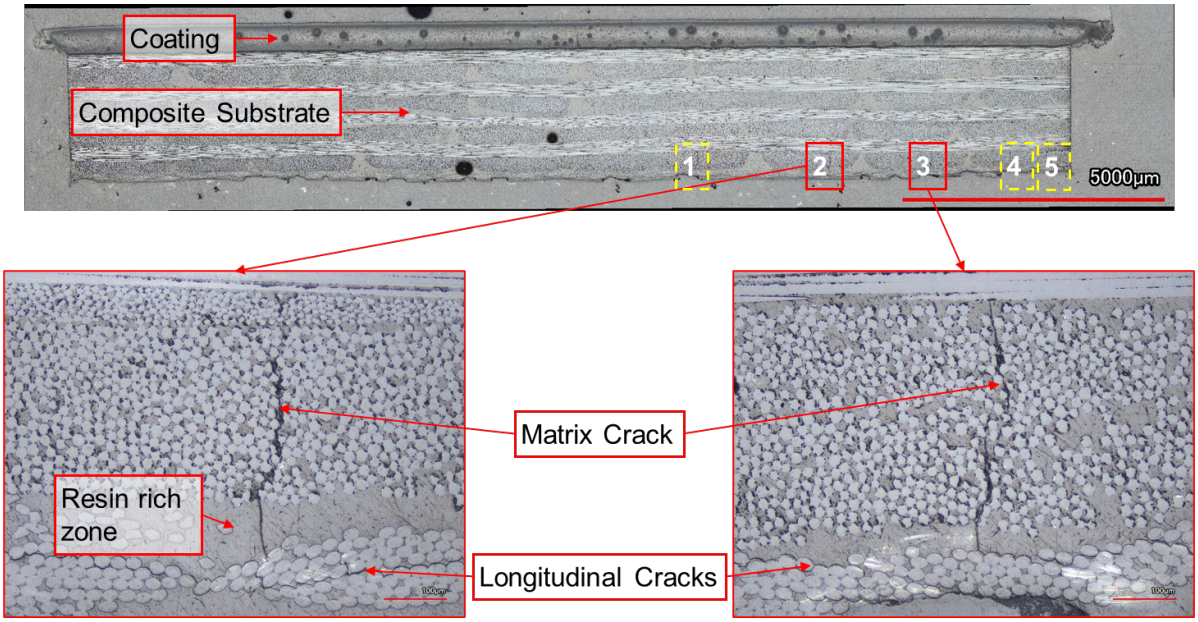

Figure F.2: Optical microscopy picture of the cross-section of Sample D1 after 10 impacts of 15 mm SHI. 5 matrix cracks were observed in this cross-section

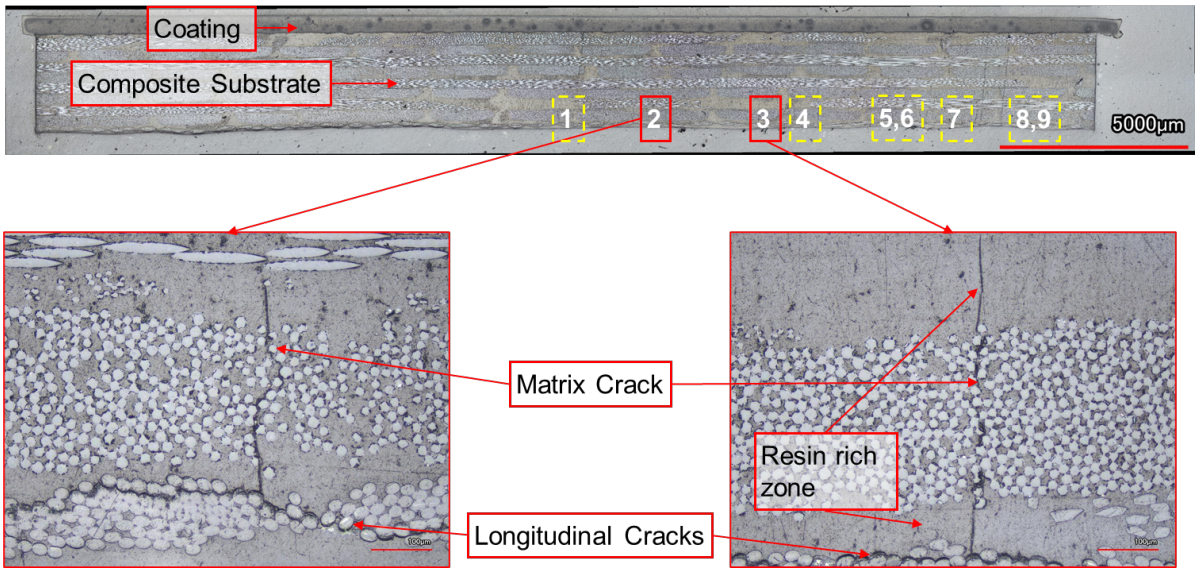

Figure F.3: Optical microscopy picture of the cross-section of Sample B4 after 10 impacts of 20 mm SHI. 9 matrix cracks were observed in this cross-section

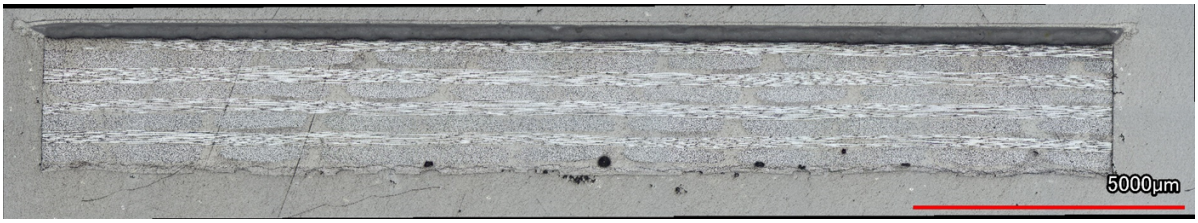

Figure F.4: Optical microscopy picture of the cross-section of Sample E5 after 5 impacts of 20 mm SHI. No matrix cracks were observed in this cross-section

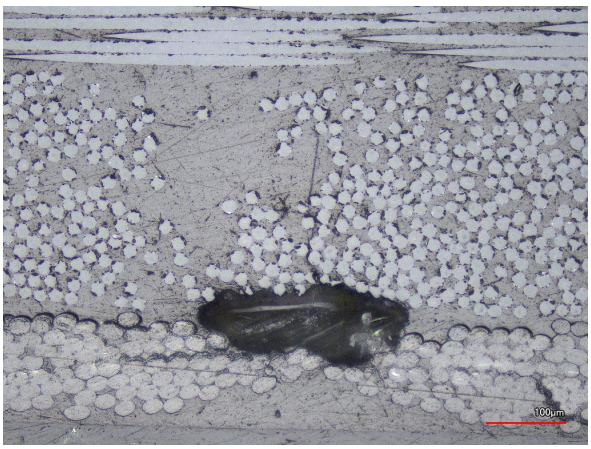

Figure F.5: Closeup of crack 3 in Sample D3, shown in Figure 4.11

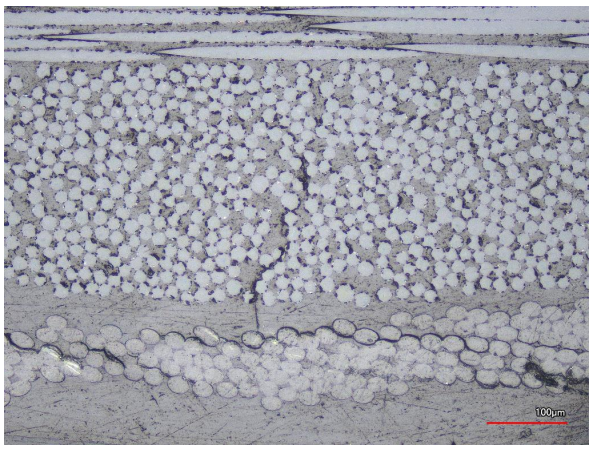

Figure F.6: Closeup of crack 4 in Sample D3, shown in Figure 4.11

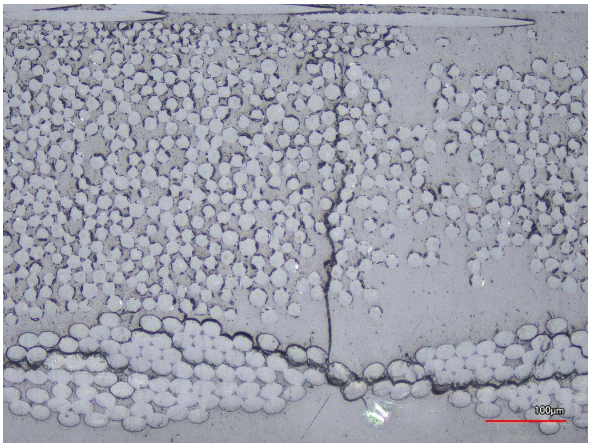

Figure F.7: Closeup of crack 3 in Sample B5, shown in Figure 4.13

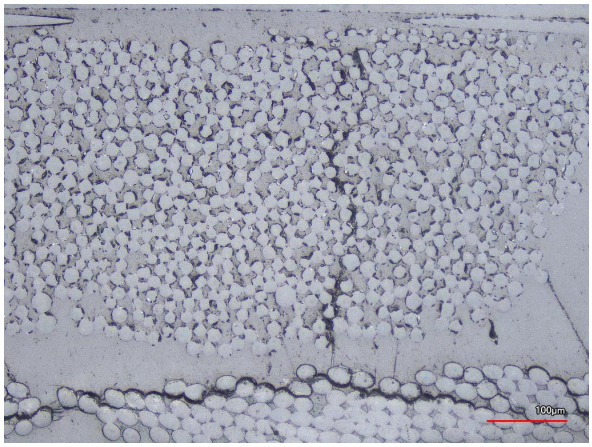

Figure F.8: Closeup of crack 4 in Sample B5, shown in Figure 4.13

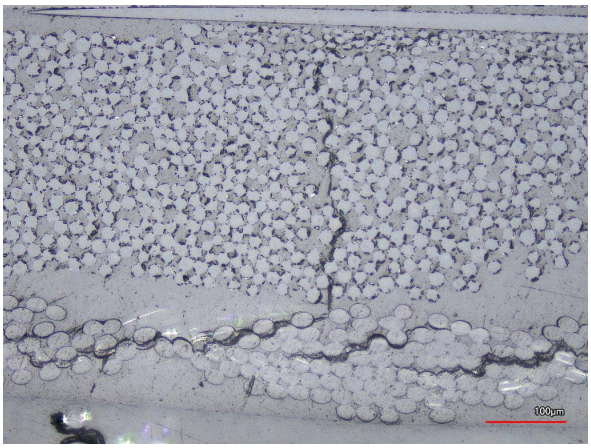

Figure F.9: Closeup of crack 3 in Sample E4, shown in Figure 4.14

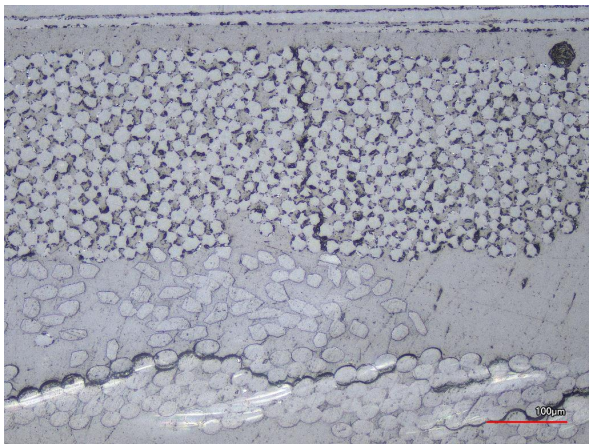

Figure F.10: Closeup of crack 4 in Sample E4, shown in Figure 4.14

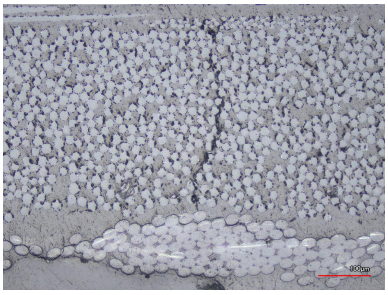

Figure F.11: Closeup of crack 1 in Sample D1, shown in Figure F.2

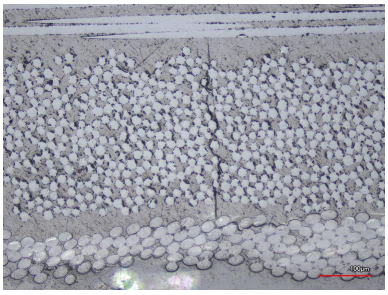

Figure F.12: Closeup of crack 4 in Sample D1, shown in Figure F.2

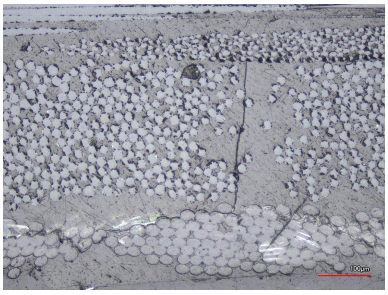

Figure F.13: Closeup of crack 5 in Sample D1, shown in Figure F.2

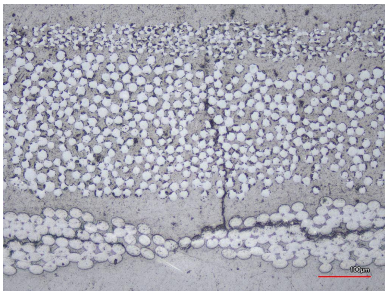

Figure F.14: Closeup of crack 1 in Sample B4, shown in Figure F.3

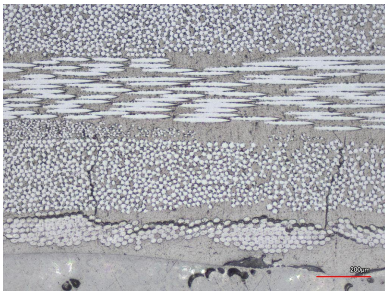

Figure F.15: Closeup of crack 5 and 6 in Sample B4, shown in Figure F.3

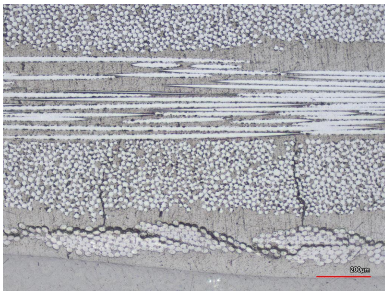

Figure F.16: Closeup of crack 8 and 9 in Sample B4, shown in Figure F.3

G

Test Summary

Test Case	Impact no.	Pressure [bar]	Velocity [m/s]	Mass [g]	KE [J]	Notes	Accept	Peak Force [kN]
C2	1	4.71	116	1.72	11.6	*SHI close to a perfect sphere*	Yes	3.785
	2	4.75	112	1.6	10.0	SHI a perfect sphere and scale placed near sample	Yes	3.568
	3	4.67	108	1.73	10.1	*SHI spherical but having particles flying alongside*	Yes	3.359
	4	4.74	112	1.64	10.3	SHI a perfect sphere and scale placed near sample	Yes	3.568
	5	4.69	108	1.6	9.3	SHI a perfect sphere and scale placed near sample	Yes	3.359
	6	4.75	112	1.62	10.2	SHI a perfect sphere and scale placed near sample	Yes	3.568
	7	4.74	108	1.57	9.2	*SHI close to a perfect sphere*	Yes	3.359
	8	4.72	112	1.55	9.7	SHI a perfect sphere and scale placed near sample	Yes	3.568
	9	4.72	116	1.67	11.2	*SHI close to a perfect sphere*	Yes	3.785
	10	4.64	108	1.66	9.7	*SHI close to a perfect sphere*	Yes	3.359
	11	5.75	120	1.66	12.0	SHI a perfect sphere and scale placed near sample	Yes	4.010
	12	5.73	124	1.73	13.3	*SHI close to a perfect sphere*	Yes	4.244
	13	5.83	124	1.67	12.8	SHI a perfect sphere and scale placed near sample	Yes	4.244
	14	5.86	124	1.7	13.1	SHI a perfect sphere and scale placed near sample	Yes	4.244
	15	5.79	124	1.73	13.3	*SHI close to a perfect sphere*	Yes	4.244
	1	4.69	110	1.7	10.3	SHI a perfect sphere and scale placed near sample	Yes	3.462
	2	4.69	112	1.64	10.3	*SHI having lots of particles and droplets flying alongside*	Yes	3.568
	3	4.71	112	1.69	10.6	*SHI a perfect sphere but some particles flying alongside*	Yes	3.568
	4	4.65	108	1.71	10.0	SHI a perfect sphere and scale placed near sample	Yes	3.359
	5	4.7	112	1.7	10.7	*SHI close to a perfect sphere*	Yes	3.568
	6	4.65	110	1.54	9.3	SHI a perfect sphere and scale placed near sample	Yes	3.462
	7	4.7	112	1.64	10.3	*No footage available*	Yes	3.568
	8	4.74	112	1.6	10.0	*SHI close to a perfect sphere*	Yes	3.568
	9	4.74	110	1.65	10.0	SHI a perfect sphere and scale placed near sample	Yes	3.462
	10	4.73	110	1.66	10.0	SHI a perfect sphere and scale placed near sample	Yes	3.462
	11	6.58	135	1.62	14.8	*SHI close to a perfect sphere but some particles flying alongside*	Yes	4.935
	12	6.68	130	1.68	14.2	SHI a perfect sphere and scale placed near sample	Yes	4.612
	13	6.64	128	1.66	13.6	SHI a perfect sphere and scale placed near sample	Yes	4.487
	14	6.83	132	1.65	14.4	SHI a perfect sphere and scale placed near sample	Yes	4.739

Table G.1 continued from previous page

Test Case	Impact no.	Pressure [bar]	Velocity [m/s]	Mass [g]	KE [J]	Notes	Accept	Peak Force [kN]
	15	6.77	130	1.66	14.0	SHI a perfect sphere and scale placed near sample	Yes	4.612
C4	1	4.75	116	1.67	11.2	*SHI not spherical and having pieces flying alongside*	Yes	3.785
	2	4.71	110	1.63	9.9	SHI a perfect sphere and scale placed near sample	Yes	3.462
	3	4.75	110	1.71	10.3	SHI a perfect sphere and scale placed near sample	Yes	3.462
	4	4.68	108	1.6	9.3	SHI a perfect sphere and scale placed near sample	Yes	3.359
	5	4.73	110	1.68	10.2	SHI a perfect sphere and scale placed near sample	Yes	3.462
	6	4.75	108	1.63	9.5	*SHI close to a perfect sphere*	Yes	3.359
	7	4.67	112	1.68	10.5	*SHI close to a perfect sphere*	Yes	3.568
	8	4.66	116	1.75	11.8	*SHI a bit small but spherical*	Yes	3.785
	9	4.77	112	1.67	10.5	SHI a perfect sphere and scale placed near sample	Yes	3.568
	10	4.7	110	1.66	10.0	SHI a perfect sphere and scale placed near sample	Yes	3.462
	11	7.06	140	1.62	15.9	SHI a perfect sphere and scale placed near sample	Yes	5.273
	12	7.1	142	1.6	16.1	SHI a perfect sphere and scale placed near sample	Yes	5.413
	13	7.05	138	1.62	15.4	*SHI close to a perfect sphere but a bit flat*	Yes	5.136
	14	7.06	140	1.63	16.0	SHI a perfect sphere and scale placed near sample	Yes	5.273
	15	7.03	135	1.66	15.1	*SHI close to a perfect sphere*	Yes	4.935
	1	4.8	105	1.48	8.2	*SHI not spherical and having pieces flying alongside*	Yes	3.208
	2	4.76	112	1.61	10.1	*SHI broken and having lots of particles impacting*	No	3.568
	3	4.73	108	1.54	9.0	SHI a perfect sphere and scale placed near sample	Yes	3.359
	4	4.73	112	1.63	10.2	SHI a perfect sphere and scale placed near sample	Yes	3.568
	5	4.67	108	1.66	9.7	*SHI a bit small but spherical*	Yes	3.359
	6	4.7	110	1.67	10.1	SHI a perfect sphere and scale placed near sample	Yes	3.462
	7	4.78	116	1.51	10.2	SHI a perfect sphere and scale placed near sample	Yes	3.785
	8	4.7	108	1.72	10.0	SHI a perfect sphere and scale placed near sample	Yes	3.359
	9	4.69	108	1.65	9.6	SHI a perfect sphere and scale placed near sample	Yes	3.359
	10	4.79	115	1.63	10.8	*SHI close to a perfect sphere*	Yes	3.730
	11	7.82	151	1.67	19.1	SHI a perfect sphere and scale placed near sample	Yes	6.091
	12	7.82	151	1.68	19.2	SHI a perfect sphere and scale placed near sample	Yes	6.091
	13	7.71	146	1.66	17.8	SHI a perfect sphere and scale placed near sample	Yes	5.725

Table G.1 continued from previous page

Test Case	Impact no.	Pressure [bar]	Velocity [m/s]	Mass [g]	KE [J]	Notes	Accept	Peak Force [kN]
	14	7.8	151	1.64	18.7	*SHI close to a perfect sphere*	Yes	6.091
	15	7.82	151	1.62	18.5	SHI a perfect sphere and scale placed near sample	Yes	6.091
D1	1	9.44	163	1.66	22.2	SHI a perfect sphere and scale placed near sample	Yes	7.085
	2	9.04	159	1.74	21.9	SHI a perfect sphere and scale placed near sample	Yes	6.681
	3	9.66	163	1.72	23.0	SHI a perfect sphere and scale placed near sample	Yes	7.085
	4	8.94	159	1.68	21.1	SHI a perfect sphere and scale placed near sample	Yes	6.681
	5	9.37	163	1.72	23.0	SHI a perfect sphere and scale placed near sample	Yes	7.085
	6	9.1	159	1.71	21.5	SHI a perfect sphere and scale placed near sample	Yes	6.681
	7	9.74	163	1.69	22.6	SHI a perfect sphere and scale placed near sample	Yes	7.085
	8	9.19	159	1.71	21.5	SHI a perfect sphere and scale placed near sample	Yes	6.681
	9	9.29	163	1.69	22.6	SHI a perfect sphere and scale placed near sample	Yes	7.085
	10	9.26	163	1.68	22.4	SHI a perfect sphere and scale placed near sample	Yes	7.085
D2	1	9.52	163	1.74	23.2	SHI a perfect sphere and scale placed near sample	Yes	7.085
	2	9.4	163	1.7	22.7	SHI a perfect sphere and scale placed near sample	Yes	7.085
	3	9.32	163	1.66	22.2	SHI a perfect sphere and scale placed near sample	Yes	7.085
	4	9.62	163	1.75	23.4	*SHI close to a perfect sphere*	Yes	7.085
	5	9.1	159	1.68	21.1	SHI a perfect sphere and scale placed near sample	Yes	6.681
	6	9.37	163	1.65	22.0	SHI a perfect sphere and scale placed near sample	Yes	7.085
	7	9.24	159	1.74	21.9	*SHI close to a perfect sphere*	Yes	6.681
	8	9.49	163	1.75	23.4	SHI a perfect sphere and scale placed near sample	Yes	7.085
	9	9.39	163	1.64	21.9	SHI a perfect sphere and scale placed near sample	Yes	7.085
	10	9.17	159	1.68	21.1	*SHI close to a perfect sphere*	Yes	6.681
	1	9.68	163	1.66	22.2	*No footage available*	Yes	7.085
	2	9.4	163	1.68	22.4	SHI a perfect sphere and scale placed near sample	Yes	7.085
	3	9.47	163	1.63	21.8	SHI a perfect sphere and scale placed near sample	Yes	7.085
	4	9.28	159	1.7	21.4	SHI a perfect sphere and scale placed near sample	Yes	6.681
	5	9.24	159	1.71	21.5	SHI a perfect sphere and scale placed near sample	Yes	6.681
	6	9.67	163	1.69	22.6	SHI a perfect sphere and scale placed near sample	Yes	7.085
	7	9.44	163	1.58	21.1	*SHI a bit small but close to a perfect sphere*	Yes	7.085

Table G.1 continued from previous page

Test Case	Impact no.	Pressure [bar]	Velocity [m/s]	Mass [g]	KE [J]	Notes	Accept	Peak Force [kN]
	8	9.37	163	1.61	21.5	SHI a perfect sphere and scale placed near sample	Yes	7.085
	9	9.19	159	1.74	21.9	SHI a perfect sphere and scale placed near sample	Yes	6.681
	10	9.28	159	1.68	21.1	SHI a perfect sphere and scale placed near sample	Yes	6.681

Table G.1: 15 mm Test Overview

Test Case	Impact no.	Pressure [bar]	Velocity [m/s]	Mass [g]	KE [J]	Notes	Accept	Peak Force [kN]
B3	1	7.21	116	4.55	30.6	*SHI close to a perfect sphere*	Yes	6.728
	2	7.14	112	4.57	28.7	SHI a perfect sphere and scale placed near sample	Yes	6.343
	3	7.09	108	4.55	26.6	*SHI spherical but having particles flying alonside*	Yes	5.971
	4	7.09	108	4.52	26.4	*SHI having lots of particles and droplets flying alongside*	No	5.971
	5	7.05	112	4.36	27.4	SHI a perfect sphere and scale placed near sample	Yes	6.343
	6	6.97	112	4.33	27.2	*No footage available*	Yes	6.343
	7	6.93	112	4.60	28.9	*SHI close to a perfect sphere*	Yes	6.343
	8	7.06	112	4.28	26.9	SHI a perfect sphere and scale placed near sample	Yes	6.343
	9	7	108	4.57	26.7	*SHI not spherical and having pieces flying alongside*	Yes	5.971
	10	6.98	112	4.53	28.4	SHI a perfect sphere and scale placed near sample	Yes	6.343
B4	1	7.13	110	4.61	27.9	SHI a perfect sphere and scale placed near sample	Yes	6.155
	2	7.07	112	4.57	28.7	*SHI having lots of particles and droplets flying alongside*	Yes	6.343
	3	7.07	112	4.49	28.2	*SHI a perfect sphere but some particles flying alongside*	Yes	6.343
	4	7.04	116	4.52	30.4	SHI a perfect sphere and scale placed near sample	Yes	6.728
	5	7.04	112	4.55	28.6	*SHI not spherical and having pieces flying alongside*	Yes	6.343
	6	7.06	112	4.56	28.6	*SHI spherical but having particles flying alongside*	Yes	6.343
	7	6.99	108	4.53	26.4	*SHI spherical but having particles flying alongside*	Yes	5.971
	8	6.99	108	4.57	26.7	SHI a perfect sphere and scale placed near sample	Yes	5.971
	9	6.96	108	4.50	26.3	SHI a perfect sphere and scale placed near sample	Yes	5.971
	10	7.01	108	4.51	26.3	SHI a perfect sphere and scale placed near sample	Yes	5.971
	1	7.09	120	4.59	33.1	*SHI not spherical and having pieces flying alongside*	Yes	7.129
	2	7.06	108	4.51	26.3	SHI a perfect sphere and scale placed near sample	Yes	5.971
	3	7.12	116	4.60	31.0	SHI a perfect sphere and scale placed near sample	Yes	6.728
	4	7.09	120	4.43	31.9	SHI a perfect sphere and scale placed near sample	Yes	7.129
	5	7.01	108	4.59	26.8	SHI a perfect sphere and scale placed near sample	Yes	5.971
	6	7.03	112	4.50	28.2	SHI a perfect sphere and scale placed near sample	Yes	6.343
	7	7.04	108	4.56	26.6	*SHI close to a perfect sphere*	Yes	5.971
	8	6.94	108	4.53	26.4	*SHI close to a perfect sphere*	Yes	5.971
	9	6.9	108	4.43	25.9	*SHI close to a perfect sphere*	Yes	5.971

B5

Table G.2 continued from previous page

Test Case	Impact no.	Pressure [bar]	Velocity [m/s]	Mass [g]	KE [J]	Notes	Accept	Peak Force [kN]
	10	7.06	112	4.51	28.3	SHI a perfect sphere and scale placed near sample	Yes	6.343
C1	1	7.01	105	4.59	25.3	*SHI not spherical and having pieces flying alongside*	Yes	5.702
	2	7.07	112	4.49	28.2	*SHI broken and having lots of particles impacting*	No	6.343
	3	7.03	112	4.55	28.6	*SHI not spherical and having pieces flying alongside*	Yes	6.343
	4	6.94	108	4.61	26.9	SHI a perfect sphere and scale placed near sample	Yes	5.971
	5	7.06	112	4.52	28.4	SHI a perfect sphere and scale placed near sample	Yes	6.343
	6	7.02	108	4.59	26.8	SHI a perfect sphere and scale placed near sample	Yes	5.971
	7	6.97	108	4.54	26.5	*SHI close to a perfect sphere*	Yes	5.971
	8	6.98	108	4.55	26.6	SHI a perfect sphere and scale placed near sample	Yes	5.971
	9	6.92	108	4.60	26.8	SHI a perfect sphere and scale placed near sample	Yes	5.971
	10	6.95	108	4.58	26.7	SHI a perfect sphere and scale placed near sample	Yes	5.971
E1	1	4.91	92	4.52	19.1	SHI a perfect sphere and scale placed near sample	Yes	4.622
	2	4.88	88	4.60	17.8	SHI a perfect sphere and scale placed near sample	Yes	4.317
	3	4.91	88	4.52	17.5	*SHI close to a perfect sphere*	Yes	4.317
	4	4.91	88	4.60	17.8	SHI a perfect sphere and scale placed near sample	Yes	4.317
	5	4.87	92	4.57	19.4	*SHI not spherical and having pieces flying alongside*	Yes	4.622
E2	1	4.86	88	4.57	17.7	*No footage available*	Yes	4.317
	2	4.98	92	4.54	19.2	SHI a perfect sphere and scale placed near sample	Yes	4.622
	3	4.84	88	4.51	17.5	SHI a perfect sphere and scale placed near sample	Yes	4.317
	4	4.82	88	4.56	17.7	*SHI broken into two halves*	No	4.317
	5	4.81	88	4.60	17.8	SHI a perfect sphere and scale placed near sample	Yes	4.317
E3	1	5.88	100	4.61	23.1	SHI a perfect sphere and scale placed near sample	Yes	5.271
	2	5.77	96	4.60	21.2	*SHI close to a perfect sphere*	Yes	4.940
	3	5.83	100	4.46	22.3	*SHI close to a perfect sphere*	Yes	5.271
	4	5.82	100	4.49	22.5	SHI a perfect sphere and scale placed near sample	Yes	5.271
	5	5.8	100	4.41	22.1	SHI a perfect sphere and scale placed near sample	Yes	5.271
	1	5.83	100	4.54	22.7	SHI a perfect sphere and scale placed near sample	Yes	5.271
	2	5.87	100	4.58	22.9	SHI a perfect sphere and scale placed near sample	Yes	5.271
	3	5.82	100	4.59	23.0	*SHI close to a perfect sphere*	Yes	5.271

Table G.2 continued from previous page

Test Case	Impact no.	Pressure [bar]	Velocity [m/s]	Mass [g]	KE [J]	Notes	Accept	Peak Force [kN]
E4	4	5.94	104	4.55	24.6	SHI a perfect sphere and scale placed near sample	Yes	5.614
	5	5.93	104	4.55	24.6	*SHI close to a perfect sphere*	Yes	5.614
E5	1	4.88	88	4.55	17.6	SHI a perfect sphere and scale placed near sample	Yes	4.317
	2	4.78	88	4.49	17.4	SHI a perfect sphere and scale placed near sample	Yes	4.317
	3	4.83	88	4.52	17.5	SHI a perfect sphere and scale placed near sample	Yes	4.317
	4	4.88	88	4.59	17.8	*No footage available*	Yes	4.317
	5	4.84	88	4.56	17.7	*SHI close to a perfect sphere*	Yes	4.317

Table G.2: 20 mm Test Overview